# Bioavailability studies of Iron Nanoparticles in Biological Samples using Mass Spectrometric Techniques

Dissertation

zur Erlangung des akademischen Grades

doctor rerum naturalium

(Dr. rer. nat.)

im Fach Chemie

eingereicht an der

Mathematisch-Naturwissenschaftlichen Fakultät

der Humboldt-Universität zu Berlin

von

M.Sc. Jenifer García-Fernández

Präsidentin der Humboldt-Universität zu Berlin

Prof. Dr.-Ing. Dr. Sabine Kunst

Dekan der Mathematisch- Naturwissenschaftlichen Fakultät

Prof. Dr. Elmar Kulke

Gutachter/innen:
1. Prof. Dr. Michael Linscheid
2. Prof. Dr. Maria Montes-Bayón
3. Prof. Dr. Ulrich Panne

Tag der mündlichen Prüfung: 5.09.2018

# ACKNOWLEDGMENTS

*After this 4 year-journey full of lights and shadows, but above all, full of learning and experiences, it is time to look back and think about the people that made this possible.*

*First of all, I would like to express my deep gratitude to my first supervisor, Prof. Maria Montes-Bayón for relying on me for this project and conducting it with a critical and sensible approach, always in pursuit of excellence and quality of research. I also want to thank Dr. Jörg Bettmer for his support as collaborator during this work and his invaluable assistance in terms of German issues. I am especially grateful to both for helping me to take the first steps in this adventure in Berlin.*

*I would like to thank my second supervisor Dr. Norbert Jakubowski, for being always available for the exchange of ideas and providing suggestions and advices greatly useful in the course of this work, especially in the last part of this journey, where his motivation was really appreciated.*

*Besides my advisors, I would like to thank Prof. Ulrich Panne for his insightful comments and encouragement in all the meetings we had.*

*I would like to mention Prof. Dr. Alfredo Sanz Medel from University of Oviedo, who led the Analytical Spectrometry group in which I started my research career. It has been an honour to be taught and inspired by a reference in the analytical chemistry field like him.*

*I am also grateful to Prof. Francisco Javier García Alonso, from the Inorganic Department at University of Oviedo, for giving me a place in his group and sharing his scientific knowledge, as well as to his students, Javier Carrasco and Javier Calleja for their help and the great time we spent together.*

*I am also indebted to Dr. Elena Añón Álvarez from the Hematology Group of the Hospital Central Universitario de Asturias for her contribution and support to this work.*

*My very special thanks go to Dr. Marcos García Ocaña, from University of Oviedo, for his immeasurable help with cell experiments. His constant readiness and expertise have made this work much easier.*

*I have had the chance to meet excellent professionals and better people at BAM. In particular, I would like to thank Dr. Carina Sötebier and Antje Cossmer for helping me in the lab; Anke Kabelitz for her assistance with X-ray diffraction and Raman experiments; Dr. Diego Esteban Fernández, for teaching me so much and so well; and Dr. Heike Traub for her time, patience, professionalism, but above all, her kindness and human quality.*

*Credits must be given to Dr. Andrea Haase, from BfR, for letting me use all facilities in her department, and Dora Wittke for giving me the training for cell culture and helping a chemist like me to operate with high autonomy out of my "comfort zone".*

*I would like to express my gratitude to Granada's group: Prof. Juan Llopis, Dr. Cristina Sánchez González, Dr. Lorenzo Rivas García and Dr. Carlos López Chaves, for showing me not only a wealth of scientific information, but also a wonderful place. Thank you all for your contributions and making me feel a part of your "family".*

*SALSA staff must be mentioned here, not only for their financial support along all this time, but also for their human support. I want to thank Katharina Schultens, Katharina Gliege, Christian Stutz, Virginia Merk, Kristin Kuschnerik, Esther Santel, Jenna Koenen, Pablo Lores Lareo and Kerstin Steinberg because they helped me to feel a little less foreigner in Berlin since the beginning.*

*Additionally, I would like to thank my fellow colleagues in Oviedo: the ones from "Proteómica" and the ones who became the little big core of "EMAB". Xavi, Silvia, Nerea, Dani, Rober, Alejandro and Mario, thanks to all of you for giving me so many good memories.*

*Moreover, I am certainly grateful to my colleagues from SALSA: Vesna, Kristina, Christine, Oleksandr, Reddy, Mona, Gergő and my sweet Hoa, for making this experience in Berlin, simply unforgettable.*

*And although not directly related to my work, there must be a special mention to my friends Ainhoa, Esteffi and Lucía. All of them have shared their experiences to encourage and support me when I needed, and I am very grateful for that. My friends Silvia & Marc, Virginia, Eva, Vanesa and Mari have always had a moment to ask me how I was or to visit me wherever I was, so I felt their support in spite of the distance.*

*And last but not least, I would like to finish these acknowledgements in Spanish cause these feelings can not be translated.*

*Gracias a mi compañero de viaje, mi mitad entera, la persona que no solo no corta mis alas, sino que me hace siempre volar más alto incluso de lo que yo creo que puedo. Gracias por ser mi mano "izquierda", celebrar mis logros y mejorar los días no tan gloriosos. Tu apoyo está presente en cada una de estas páginas.*

*Y GRACIAS eternas a mi madre, sencillamente la causante de que yo esté aquí, de que escriba estas líneas y de que haya aprendido a luchar sin rendirme. Eres mi inspiración, mi guía, mi hogar, la mejor consejera y el más incondicional de los apoyos. Nunca te daré las gracias lo suficiente por todo el bien que me haces. Esto va por ti, mamá.*

*“You cannot get through a single day without having an impact on the world around you. What you do makes a difference, and you have to decide what kind of difference you want to make.”*

**— Jane Goodall**

# Table of contents

ABSTRACT ..... 1
ABSTRAKT ..... 2
1 INTRODUCTION ..... 7
1.1. The role of iron in living organisms ..... 7
1.2. Iron metabolism ..... 8
1.2.1. Iron in the body ..... 8
1.2.2. Iron absorption and transport ..... 9
1.2.3. Iron storage ..... 11
1.2.4. Function of iron in the body ..... 12
1.2.5. Iron excretion ..... 12
1.2.6. Regulation of iron homeostasis ..... 12
1.3. Iron metabolic disorders and pharmacological treatments ..... 13
1.3.1. Iron overload and iron deficiency ..... 13
1.3.2. Treatments to overcome iron deficiency ..... 19
1.3.2.1. Iron salts ..... 22
1.3.2.2. Iron nanoparticles ..... 23
1.3.2.2.1. Parenteral treatment ..... 24
1.3.2.2.2. Oral supplementation ..... 25
1.3.3. Pharmacokinetics of nanoparticles ..... 26
1.3.3.1. Administration route ..... 27
1.3.3.2. Distribution ..... 28
1.3.3.3. Elimination ..... 29
1.3.4. Impact evaluation in biological media: nanotoxicity ..... 30
1.3.4.1. Cell toxicity ..... 31
1.3.4.2. Oxidative stress ..... 33
1.4. Analytical strategies for the characterization and determination of metallic nanoparticles ..... 36
1.4.1. Non-hyphenated techniques ..... 38
1.4.1.1. Inductively coupled plasma mass spectrometry (ICP-MS) ..... 38
1.4.1.2. Electron microscopy ..... 44
1.4.1.3. Dynamic light scattering ..... 48
1.4.1.4. X-ray diffraction ..... 50
1.4.2. Hyphenated techniques ..... 51

1.4.2.1. Chromatographic and electrophoretic methods ..... 52
1.4.2.2. Field flow fractionation techniques coupled to ICP-MS ..... 56
1.5. Isotope dilution analysis ..... 57
2 OBJECTIVES ..... 67
3 EXPERIMENTAL SECTION ..... 71
3.1. Reagents and solutions ..... 71
3.2. Instrumentation ..... 73
3.2.1. Inductively coupled plasma mass spectrometry ..... 73
3.2.1.1. Agilent 7500 CE ..... 73
3.2.1.2. Agilent 7700x ..... 75
3.2.1.3. iCAP TQ Thermo Scientific ..... 76
3.2.1.4. Thermo Element XR ..... 78
3.2.2. High performance liquid chromatography ..... 79
3.2.2.1. HPLC systems ..... 79
3.2.2.2. Chromatographic columns and related parameters ..... 79
3.2.2.3. Hyphenation of HPLC to ICP-MS ..... 81
3.2.2.4. Experimental set-up for post-column IDA ..... 81
3.2.3. Laser ablation system ..... 82
3.2.4. Miscellaneous ..... 83
3.3. Data acquisition and treatment ..... 83
3.4. Experimental procedures ..... 84
3.4.1. Characterization of iron-sucrose formulations: Venofer® ..... 84
3.4.2. Incubation of serum and blood samples with Venofer® ..... 85
3.4.3. Evaluation of the quantitative association of released Fe to transferrin sialoforms ..... 86
3.4.3.1. Iron Transferrin saturation ..... 86
3.4.3.2. Optimization of Transferrin sialoforms separation ..... 86
3.4.4. Iron association to other binding proteins ..... 87
3.4.5. Iron nanoparticles ..... 87
3.4.5.1. Synthesis and purification procedure of FeNPs studied ..... 88
3.4.5.1.1. Synthesis of isotopically enriched $^{57}$FeNPs ..... 88
3.4.5.1.2. Synthesis of Holmium-doped FeNPs ..... 89
3.4.5.2. Acid lability assays ..... 89
3.4.6. *In vitro* studies ..... 90
3.4.6.1. Cell culture ..... 90
3.4.6.2. Cellular uptake studies ..... 90

3.4.6.3. Total iron quantification in cell samples ..... 91
3.4.6.4. Nanoparticle extraction protocol ..... 91
3.4.6.5. Sample preparation for LA-ICP-MS measurements ..... 91
3.4.6.6. Viability assays ..... 91
3.4.6.7. Oxidative stress assay ..... 93
3.4.7. *In vivo* studies ..... 94
3.4.7.1. Small intestine perfusion in rats ..... 94
3.4.7.2. Total iron quantification in animal tissues ..... 95
3.4.7.3. TEM images ..... 96
4 RESULTS AND DISCUSSION ..... 99
4.1. Evaluation of iron bioavailability from Venofer® in biofluids ..... 100
4.1.1. Characterization of iron-sucrose nanosuspension: Venofer® ..... 100
4.1.2. *In vitro* solubilization experiments ..... 103
4.1.3. Released iron incorporation into transferrin binding sites ..... 105
4.1.3.1. Separation of the transferrin sialoforms in serum by anion exchange chromatography ..... 105
4.1.3.2. Quantitative analysis of the iron incorporated in the different sialoforms of transferrin by Isotope Pattern Deconvolution ..... 106
4.1.4. Iron association to other serum proteins ..... 107
4.2. *In vitro* studies on iron nanoparticles for the oral treatment of anaemia ..... 110
4.2.1. Synthesis and purification of iron nanoparticles potentially used for the oral treatment of anaemia ..... 110
4.2.2. Characterization of synthesized iron nanoparticles ..... 113
4.2.2.1. Dextran coated iron oxide NPs ..... 113
4.2.2.2. Sucrose coated iron oxide NPs ..... 115
4.2.2.3. Tartrate modified coated Iron Oxide NPs ..... 116
4.2.2.3.1. Isotopically enriched $^{57}$FeNPs ..... 117
4.2.2.3.2. Holmium-doped FeNPs ..... 118
4.2.3. Uptake studies in different cell lines ..... 120
4.2.3.1. FeNPs characterization in cell culture medium ..... 120
4.2.3.2. Total iron quantification in cell samples by ICP-MS ..... 121
4.2.3.3. Iron uptake mechanism and subcellular distribution ..... 122
4.2.4. LA-ICP-MS experiments ..... 123
4.2.5. Toxicity assessment ..... 126
4.2.5.1. Cell viability assays ..... 126
4.2.5.2. Oxidative stress evaluation: Reactive Oxygen Species assay ..... 127

4.2.6. Speciation and quantitative analysis of nanoparticles and ionic species of iron by HPLC-ICP-MS in combination with Isotope Dilution Analysis ..... 129
4.2.6.1. Optimization of HPLC conditions ..... 129
4.2.6.2. Quantitative studies ..... 131
4.2.6.2.1. Recovery studies for Venofer®, FeNPs and soluble species of iron ..... 131
4.2.6.2.2. Analysis of iron species in Caco-2 cell samples ..... 132
4.3. *In vivo* studies on iron nanoparticles for the oral treatment of anaemia: distribution and bioaccumulation assessment in rats ..... 135
4.3.1. Acid lability assays to check the stability of FeNPs in gastric conditions ..... 135
4.3.2. Iron absorption and distribution through the small intestine ..... 136
4.3.3. Small intestine perfusion experiment using $^{57}$FeNPs ..... 138
4.3.4. Iron distribution in other tissues ..... 140
5 CONCLUSIONS AND OUTLOOK ..... 145
6 GLOSSARY ..... 151
7 BIBLIOGRAPHY ..... 155

# ABSTRACT

In this study, a characterization of iron supplements used as parenteral and oral preparations for the treatment of severe anaemia based on spheroidal Fe-carbohydrate nanoparticles and bioavailability studies of such in biological samples have been developed.

On the one hand, a complete characterization of a commercial preparation for the **parenteral treatment** of anaemia (**Venofer®**), has been carried out using High Resolution Transmission Electron Microscopy (HR-TEM), Dynamic Light Scattering (DLS), Energy Dispersive X-Ray analysis (EDX), and Size Exclusion Chromatography (SEC) coupled to UV-Vis and ICP-MS detection. With the aim of evaluating iron bioavailability from these sucrose coated-iron oxide nanoparticles, solubilisation studies of the drug have been conducted in serum and blood. Moreover, speciation experiments of serum proteins were conducted using UV-vis and ICP-MS detection, providing more in-depth information about the drug and its behaviour in the body.

On the other hand, tartrate-modified coated-iron oxide nanoparticles (**FeNPs**) have been synthesized according to a precipitation method of a Fe(III) salt in basic medium followed by an additional step of surface coating with sodium tartrate and adipic acid in order to obtain non-aggregated particles. This protocol has been also applied to the synthesis of isotopically enriched $^{57}$FeNPs. Nanoparticles were further characterized using HR-TEM, EDX, DLS, Small Angle X-Ray Scattering (SAXS), Wide Angle X-Ray Scattering (WAXS) and UV-vis. As these nanoparticles are potentially suitable for the **oral supplementation** in anaemia's treatment, the lability of these FeNPs in acidic medium (similar to stomach acidic conditions) was evaluated, and total Fe was quantified in nanoparticulate and soluble fraction. With the aim of determining nanostructure behaviour in cellular media, a speciation strategy for nanoparticles and ionic species of iron based on a reversed-phase high-performance liquid chromatography (HPLC) coupled to ICP-MS was carried out and applied for the first time to Caco-2 cell samples. Moreover, a quantification approach was also tackled by applying an online post-column isotope dilution analysis with $^{57}$Fe as isotopically enriched standard. With the aim of evaluating cytotoxicity from these tartrate-modified iron oxide nanoparticles, colorimetric assays have been conducted in different cell lines (THP-1, macrophages, Caco-2, and HT-29) and oxidative damage was assessed by measuring ROS production. Finally, *in vivo* models were used to determine iron absorption degree in the small intestine after perfusion experiments in rats. The fate of the FeNPs was also studied by analysing other tissues as liver, kidney, spleen, or blood after the intestinal uptake.

# ABSTRAKT

In dieser Studie wurde eine Charakterisierung von Eisenpräparaten entwickelt, die als parenterale und orale Präparate zur Behandlung schwerer Anämie auf Basis von sphäroidalen Fe-Kohlenhydrat-Nanopartikeln verwendet werden, sowie von Bioverfügbarkeitsstudien solcher in biologischen Proben.

Einerseits wurde eine vollständige Charakterisierung eines kommerziellen Präparats für die **parenterale Behandlung** von Anämie (**Venofer®**) unter Verwendung von hochauflösender Transmissionselektronenmikroskopie (HR-TEM), dynamischer Lichtstreuung (DLS), energiedispersiver X- Ray-Analyse (EDX) und Größenausschlusschromatographie (SEC) gekoppelt mit UV-Vis- und ICP-MS-Detektion. Mit dem Ziel, die Bioverfügbarkeit von Eisen aus diesen Saccharose-beschichteten Eisenoxid-Nanopartikeln zu untersuchen, wurden Solubilisierungsstudien des Arzneimittels in Serum und Blut durchgeführt. Darüber hinaus wurden Speziationsexperimente von Serumproteinen unter Verwendung von UV-vis- und ICP-MS-Detektion durchgeführt, die detailliertere Informationen über das Arzneimittel und sein Verhalten im Körper liefern.

Auf der anderen Seite wurden Tartrat-modifizierte Eisenoxid-Nanopartikel (**FeNPs**) nach einem Fällungsverfahren eines Fe(III) -Salzes in basischem Medium synthetisiert, gefolgt von einem zusätzlichen Schritt der Oberflächenbeschichtung mit Natriumtartrat und Adipinsäure um nicht-aggregierte Partikel zu erhalten. Dieses Protokoll wurde auch auf die Synthese von isotopenangereicherten $^{57}$FeNPs angewendet. Nanopartikel wurden mit HR-TEM, EDX, DLS, Kleinwinkel-Röntgenstreuung (SAXS), Weitwinkel-Röntgenstreuung (WAXS) und UV-vis weiter charakterisiert. Da diese Nanopartikel möglicherweise für die **orale Supplementierung** bei der Behandlung von Anämie geeignet sind, wurde die Labilität dieser FeNPs in saurem Medium (ähnlich den sauren Bedingungen im Magen) bewertet, und das gesamte Fe wurde in nanopartikulärer und löslicher Fraktion quantifiziert. Mit dem Ziel, das Verhalten von Nanostrukturen in zellulären Medien zu bestimmen, wurde eine Speziationsstrategie für Nanopartikel und ionische Eisenspezies basierend auf einer Umkehrphasen-Hochleistungsflüssigkeitschromatographie (HPLC) gekoppelt mit ICP-MS durchgeführt und erstmals angewendet Caco-2-Zellproben. Darüber hinaus wurde ein Quantifizierungsansatz durch Anwendung einer Isotopenverdünnungsanalyse mit $^{57}$Fe als Isotopen-angereichertem Standard durchgeführt. Mit dem Ziel, die Zytotoxizität von diesen Tartrat-modifizierten Eisenoxid-Nanopartikeln zu untersuchen, wurden kolorimetrische Assays in verschiedenen Zelllinien (THP-1, Makrophagen, Caco-2 und HT-29) durchgeführt und die oxidative Schädigung

wurde durch Messen der ROS-Produktion bewertet. Schließlich wurden *In-vivo*-Modelle verwendet, um den Eisenabsorptionsgrad im Dünndarm nach Perfusionsexperimenten an Ratten zu bestimmen. Das Schicksal der FeNPs wurde auch untersucht, indem andere Gewebe wie Leber, Niere, Milz oder Blut nach der intestinalen Aufnahme analysiert wurden.

# 1 INTRODUCTION

# 1 INTRODUCTION

## 1.1. The role of iron in living organisms

Iron (Fe) is a metal and an essential micronutrient for animals, plants, microorganisms, and human beings as it is required in the transport of oxygen and electrons, and catalysis of reactions necessary for the development, differentiation and cellular proliferation. It is found naturally in earth's crust at about 5 % concentration form as hematite ($Fe_2O_3$) and magnetite ($Fe_3O_4$) ore. In aquatic environments under anoxic conditions, iron is present in elemental form or as iron oxide when oxygen is available.

Regarding its composition, this metal has four natural isotopes, which masses and relative abundances are collected in Table 1 [1]. Additionally, it has 24 unstable isotopes, with lifetimes between 20 milliseconds ($^{46}$Fe) and 1.5x10$^6$ years ($^{60}$Fe).

**Table 1. Iron Isotopes.**

| Isotope | Lifetime | Relative abundance (%) | Atomic mass (u) |
|---|---|---|---|
| **$^{54}$Fe** | Stable | 5.845 | 53.9396 |
| **$^{56}$Fe** | Stable | 91.754 | 55.9349 |
| **$^{57}$Fe** | Stable | 2.119 | 56.9354 |
| **$^{58}$Fe** | Stable | 0.282 | 57.9333 |

Despite being one of the most abundant metals in the Earth's crust, its physico-chemical properties make it difficult to be available for living organisms as it is almost insoluble at pH 7. Most of the iron is present in oxidized/ferric insoluble forms and thus, microbes cannot assimilate it. In consequence, evolution has developed mechanisms to solubilize, capture from the environment, store, and use it in case of necessity [2].

Like most transition metals, iron has a variety of chemical reaction possibilities. The reversible change of Fe(II) into Fe(III) through redox-reactions and its naturally high abundance might explain why iron plays an extremely important role virtually in all living organisms [3, 4]. In plants this trace metal is involved in the photosynthesis, the generation of chemical energy by reaction of photons with photosynthetic membranes [5]. In vertebrates, iron is present in its most important oxidation states +2 and +3 and in cofactors like haem. This prosthetic group, more precisely haem b, is present in the haemoglobin (Hb), the oxygen transport protein in blood. It can also be

found in myoglobin, the haemoglobin analogue in the muscle tissue. Haem b contains Fe(II) in the centre of the planar porphyrin ring (bound to the four pyrrolic groups) which is responsible for the coordination and transport of oxygen [6].

Most of the iron present in living organisms is tightly complexed in proteins, although it can be also present in a soluble ‘‘pool’’ of low molecular weight complexes such as ferric citrate and Fe(III)-ATP [7].

Although the participation of iron in many biochemical processes explains its significant role in most living systems, its careful management is critical for them: an excess of iron can cause tissue damage, but a depletion of this trace metal is also harmful, as it is required for many physiological functions. Considering this ambivalent role, nature has developed a sophisticated system to maintain iron homeostasis by balancing its uptake, storage, and mobilization of reserves.

## 1.2. Iron metabolism

### 1.2.1. Iron in the body

Healthy humans contain between 2000 and 5000 mg of iron depending on various factors such as gender, age, or nutrition [8]. Around two third of it is within erythrocytes and 15-25 % is stored in splenic and hepatic macrophages. The rest is distributed in various proteins such as myoglobin, cytochromes, or other ferroproteins. Only about 3 mg are bound to plasma transferrin and constitute the mobile iron compartment that supplies the intracellular iron stores, but the daily exchange of iron through plasma transferrin is ten times this amount. About 1-2 mg of iron is lost every day, through skin and enteric desquamation and minor blood losses. This loss is tightly balanced by intestinal absorption. Therefore, iron recycling represents most of the iron homeostasis in human body. It is graphically represented in Figure 1.

The situation is different in menstruation women where there are controversial discussions about iron stores, ferritin, and haemoglobin levels. Apparently, lower haemoglobin and ferritin levels in menstruating women have been accepted as normal rather than possibly representing widespread iron deficiency [9].

Under pathological conditions (e.g. iron overload or serum transferrin deficiency) the amount of iron not bound to transferrin becomes important. This is distributed to organs in an inappropriate manner leading to iron overload in parenchymal organs such as liver and pancreas.

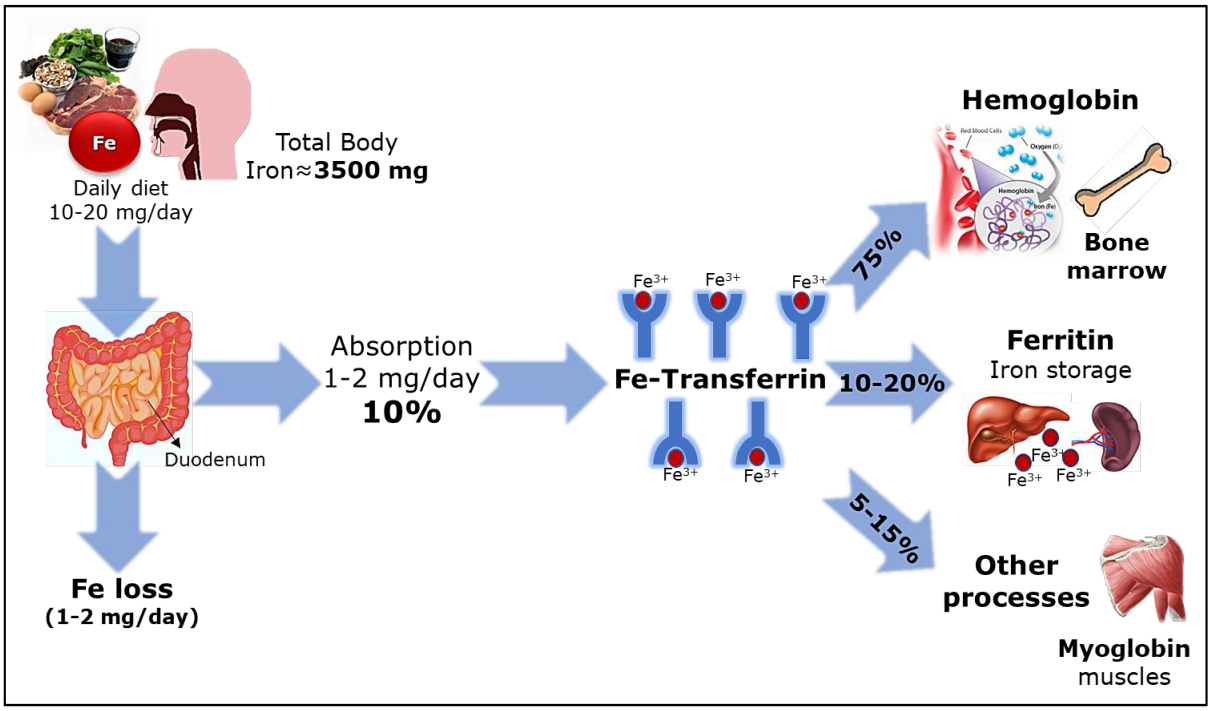


***Figure 1. Metabolic pathway of iron in the human body.***

### 1.2.2. Iron absorption and transport

Iron-containing food is the natural way to supply iron to the body. A normal diet daily provides 15-20 mg of iron in haem (10 %) and non-haem (ionic, 90 %) forms but only 10 % (1-2 mg) of that total amount is absorbed. Iron absorption occurs as the sum of complex mechanisms that take place throughout the entire intestine but more efficiently in duodenal enterocytes and polarized upper jejunal absorptive cells under acidic conditions [10]. Gastric acid lowers the pH in the proximal duodenum and thus, it reduces $Fe^{3+}$ in the intestinal lumen by ferric reductases. This allows the transport of the formed $Fe^{2+}$ across the apical membrane of enterocytes and the enhancement of ferric iron solubility and uptake [11]. The presence of a normal gastric juice is a crucial factor in facilitating iron absorption [12]. In Table 2 the different physiological pH values in the gastrointestinal tract are collected.

**Table 2. Physiological pH ranges throughout the gastrointestinal tract.**

| pH | | | | |
|---|---|---|---|---|
| Esophagus | Stomach | Intestine | | |
| | | Duodenum | Jejunum | Ileum |
| 5 - 7 | 2 - 5 | 2.7 - 4 | 4 - 7 | 7 - 8 |

This absorption depends on the form of iron that is present in the diet. The haem form is found in haemoglobin, myoglobin, cytochromes and other haemoproteins which are present mainly in food of animal origin. Ionic iron composed by inorganic salts of this metal is mainly found in food of plant origin and most of the pharmaceutical preparations used for the treatment of iron deficiency. Dietary non-haem iron primarily exists in an oxidized form ($Fe^{3+}$) that is not bioavailable and must first be reduced to $Fe^{2+}$ form by ferrireductase enzyme, expressed in the apical surface of the enterocyte, using vitamin C as coenzyme and hydrochloric acid present in the stomach [13]. This absorption can be facilitated by ingestion of meat and organic acids, particularly ascorbic acid. Conversely, polyphenols, phytates or a phosphate enriched diet decreases this absorption [14]. The DMT1 (Divalent Metal Transporter 1) is a membrane protein that transports ferrous ions through epithelial cells of the intestine. It can also transport other divalent metals such as zinc, manganese, copper, cadmium or lead [15].

Haem iron crosses cellular membranes of the enterocyte in the form of intact metalloporphyrin, after being separated from the globin by endoluminal proteases action. This is made by a transporter protein for the haem group called Haem Carrier Protein-1 (HCP1) [16]. Once inside the cytosol of the enterocyte, hemoxygenase releases iron from the tetrapyrrolic structure and incorporates it to bloodstream as a free metal. Although it represents only a 10 % of total iron from the diet, haem iron absorption is higher and is less affected by diet variations.

Once the iron is absorbed, 3-4 mg of the iron circulates in the bloodstream, mainly bounded to transferrin. This small amount plays an important role in the iron metabolism, since all the iron transported in the organism has to pass through the plasma. In this sense, the transferrin (Tf) is the main iron protein transporter both in serum and extracellular fluid. It is known that Tf can bind different metals, but it shows a special affinity for ferric ions, whereas it is not bound to ferrous species [15]. Tf is responsible of the transport of iron to bone marrow for the haemoglobin synthesis. It is also known that iron can also be bound to other proteins as ceruloplasmin, lactoferrin, $\alpha$1 and $\alpha$2-globulins, aminoacids as histidine or lysine, organic acids. ferritin and other plasma proteins not identified [17].

Most of iron in the organism (2.5 g) is found in the erythrocytes of haemoglobin, but the bone marrow is the place of most usage of iron (where red blood cells are formed). When erythrocytes reach the end of their average life (120 days approximately), they are destroyed by macrophages from the reticuloendothelial system, mainly in spleen, liver and bone marrow. Most of iron released from macrophages is incorporated into plasma where Tf binds and transports it to new

erythrocytes formation or to store in the liver. The reticuloendothelial system also receives a small amount of iron (around 2 mg) coming from the inefficient erythropoiesis [11].

### 1.2.3. Iron storage

Most of the stored iron is found in the liver (one third approximately), spleen and bone marrow, as ferritin and hemosiderin associated forms. The rest of iron is captured by different tissues for the synthesis of myoglobin, cytochromes, peroxidases and other enzymes and proteins which use iron as cofactor.

Iron contained in haemoglobin, tissues, and bloodstream remains practically constant whereas stored iron varies depending on the amount present in the organism and availability from the diet. For this reason, iron deposits act as a damper when there is a decrease in the haemoglobin, myoglobin or intracellular ferroenzymes levels [15, 18].

Ferritin concentration together with hemosiderin reflects the body iron stores, but most of iron is bound to ferritin and thus, serum ferritin concentrations correlate well with total body iron stores under steady state conditions [11]. The ferritin molecule is a hollow protein shell (outer dimeter 12-13 nm, inner diameter 7-8 nm; $M_r \approx$ 450 kDa) composed of 24 polypeptide subunits [7]. It has several functions such as acquiring Fe(II), catalysing its oxidation, and inducing mineralization inside the cavity, which can store up to 4500 atoms of iron. The high storage capacity is achieved by sequestering the iron as a compact mineral, resembling the structure of the mineral ferrihydrite FeO(OH). This is possible due to the two structurally similar, but mechanistically different protein subunits contained in the protein shell: the heavy (H) and the light (L) chains. The H-type subunit catalyses the oxidation of Fe(II) to Fe(III), while the L-type subunit promotes mineralization inside the protein cage [19].

On the other hand, hemosiderin is an iron storage complex that less readily releases iron for body needs. Despite the name "hemosiderin", the iron is in the nonheme form. Hemosiderin can be isolated as insoluble granules which may contain small amounts of ferritin, but most of the iron is not water-soluble. Most estimations of the iron content in hemosiderin granules lie in the range 24-45 % as compared with 16-23 % in ferritin. The morphology and properties of ferritin and hemosiderin iron, together with the results of experiments with radioactive iron, suggest that ferritin may be a metabolic precursor of hemosiderin and that the latter consists of aggregates of ferritin molecules from which much of the protein has been removed by proteolytic digestion. However, other results suggest that hemosiderin may be formed independently when the rate of

uptake of iron exceeds the tissue's capacity to make ferritin protein, and that hemosiderin iron may subsequently move into ferritin. These results are not necessarily contradictory but may reflect different responses to different conditions [20].

### 1.2.4. Function of iron in the body

In the human body, iron generally appears bound to proteins and not as free metal ions. As can be seen in Table 3, between 60-70 % of the total body iron is bound to haemoproteins (haemoglobin, myoglobin) and only a small fraction (≈ 2 %) of iron is incorporated in the porphyrin ring of other proteins such as cytochromes, peroxidases, catalases, and NO-synthases.

**Table 3. Iron distribution in human body**

| Protein | Function | Concentration | | | |
|---|---|---|---|---|---|
| | | Male | | Female | |
| | | $\mu g \cdot g^{-1}$ | % | $\mu g \cdot g^{-1}$ | % |
| **Haemoglobin** | **$O_2$ transport** | 31 | 62 | 28 | 74 |
| **Myoglobin** | | 5 | 10 | 4 | 11 |
| **Enzymes** | **Metabolism** | 1 | 2 | 1 | 2 |
| **Transferrin** | **Fe transport** | 0.1 | 0.2 | 0.08 | 0.2 |
| **Ferritin** | **Fe storage** | 13 | 26 | 5 | 13 |
| **Hemosiderin** | | | | | |

### 1.2.5. Iron excretion

Apart from iron losses due to menstruation, other bleeding or pregnancy, iron is highly conserved and not readily lost from the body. There is some obligatory loss of iron from the body that results from the physiologic exfoliation of cells from epithelial surfaces, including the skin, genitourinary and gastrointestinal tract. However, these losses are estimated to be very limited (1 mg/day). Iron losses through bleeding can be substantial and excessive menstrual blood loss is the most common cause of iron deficiency in women [11].

### 1.2.6. Regulation of iron homeostasis

The absorption of iron is dependent on body iron stores, hypoxia, inflammation and rate of erythropoiesis [21]. A constant balance is required between the absorption, transport, storage, and use of iron to keep iron homeostasis. Since there is no appropriate regulatory pathway for

active excretion of iron, iron homeostasis is only regulated by the release of the trace metal into the blood serum [11].

Mechanisms that regulate systemic iron homeostasis are mainly found in the liver and involve two molecules, hepcidin and ferroportin. These two proteins together regulate the flow of iron from cells into the systemic circulation. Ferroportin is the only known cellular iron exporter protein and is expressed especially in macrophages, duodenal enterocytes, and hepatocytes. Its expression can be controlled at the transcriptional, translational and post-translational levels. The transcription of macrophage ferroportin gene can be promoted by haem and inhibited by inflammatory stimuli. At a systemic level the most important mechanism regulating ferroportin involves the iron regulatory hormone hepcidin [22, 23]. This peptide was discovered in recent years after being isolated from human urine samples [24]. Then, it was found that hepcidin-25 can inhibit the iron efflux from cells by binding ferroportin [25]. Hepcidin binding to ferroportin induces the rapid ubiquitination and internalization of the hepcidin-ferroportin complex, thereby reducing cell surface expression and iron export. Since it was discovered, its interaction with ferroportin not only has been established as a critical factor for systemic iron regulation but also the perturbations in the complex are proven to be the basis of many iron-associated disorders [22].

## 1.3. Iron metabolic disorders and pharmacological treatments

Under physiological conditions, there is an equilibrium between iron absorption, iron transport, and iron storage in the human body. However, slightly modifications on the uptake from the diet or the regulatory system can affect directly the iron stores. Depending on there is an increment or a decreasing of iron concentration in the body, different metabolic disorders can be associated and will be discussed in the following section.

### 1.3.1. Iron overload and iron deficiency

#### *Iron overload*

Iron overload responds to an excess of iron accumulation in the human body and is the result of many disorders and could lead to the development of organ damaged and increased mortality [26]. Even in mild cases, iron excess can cause cellular damage by catalysing the formation of ROS and accumulating hemosiderin in the affected organs, especially liver, heart, pancreas, kidney, and cerebellum [17].

The main reason for iron overload is an inadequate iron absorption by means of altered hepcidin-25 secretion. Low plasma hepcidin leads to high ferroportin levels, which allow increased iron uptake, hepatic iron overload, and low levels of iron stored in macrophages. In addition, as transferrin becomes saturated in iron-overload states, non-transferrin bound iron appears. Part of this labile plasma iron is highly reactive, inducing free radical formation. Free radicals are responsible for the parenchymatous cell injury associated with iron-overload syndromes [27].

Alterations include hereditary defects either of compounds involved in the expression of hepcidin-25 which lead to low hepcidin-25 concentrations or the ferroportin, resulting in increased hepcidin-25 response known as **primary hemochromatosis** (it must be remarked that a decrease in hepcidin-25 produces a higher iron mobilization from cells into the bloodstream). Despite the alterations and degrees of iron induced damage are multiple, modifications in serum iron levels are comparable and targets of iron deposition and damage are identical. As a consequence of the progressive iron uptake, the binding capacity of transferrin in serum is exceeded, leading to non-specific iron binding and accumulation of iron in hepatic cells [28]. This is associated to liver pathologies such as cirrhosis and hepatic carcinoma, endocrine disorders (diabetes mellitus or impotence), heart damage (cardiac dysrhythmia, heart failure) and joint disease (destructive arthritis) [29, 30].

Another kind of iron overload is the transfusion iron overload or **secondary hemochromatosis** and it is not caused by primary genetic defects in the regulation of iron homeostasis. Actually, it may occur due to a variety of causes including the ingestion of large amounts of dietary iron, repeated blood transfusions and various haematological conditions that result in the increased absorption and storage of excess iron [22]. In this case, plasma hepcidin levels are elevated resulting in degradation of ferroportin. The reduced levels of ferroportin limit the uptake of iron from the intestine, reduce the export from macrophages and increase iron storage [30].

One more type of syndrome is called **iron loading anaemia** and is caused by an ineffective erythropoiesis which leads to low levels of hepcidin. Despite increased iron stores, increased erythropoiesis releases a number of growth differentiation factors, which in turn suppress liver hepcidin production by inhibiting inflammatory and iron-sensing pathways, causing an insatiably iron demand [28, 31]. A complete classification of the iron-overload syndromes is collected in Figure 2 [27].

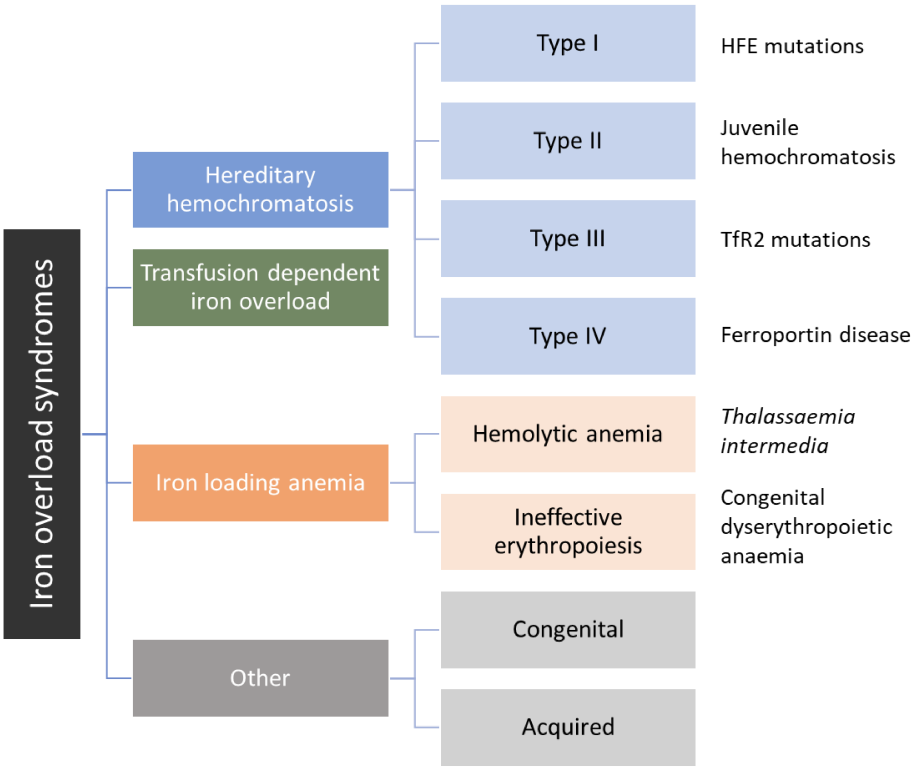


***Figure 2. Classification of iron overload pathologies.***

The concentration and total iron concentration in different tissues are critical parameters that determine clinical diagnosis in all systemic iron overload forms, either if it is caused by upregulated intestinal iron absorption or by blood transfusion [32].

The diagnosis of iron overload requires sequential steps: clinical evaluation, biochemical testing, assessment of total body iron, and molecular tests. The first analytic step is to detect some of the expected symptoms that are associated to iron overload (e.g. fatigue, dark skin, arthralgia, hepatomegaly, cardiomyopathy, endocrine disorder, etc). Second step consists on excluding mutations in the HFE gene, especially in Caucasian patients. If the diagnosis of HFE haemochromatosis is not confirmed, the third diagnostic step is to check an increased level of iron in the body, before starting expensive and time-consuming analysis in search for mutations in other genes. The fourth step is based on a precise molecular diagnosis, which requires demonstration of the nucleotide change at the DNA level. However, as molecular diagnosis is expensive, time-consuming and, in some cases, unable to provide a clear diagnosis, its utility is sometimes questioned [27].

Standard therapy for most patients with haemochromatosis and iron overload is, in general, the removal of blood to reduce ferritin levels to the low reference range (20-50 ng $mL^{-1}$), followed

by a life-long phlebotomy treatment to keep ferritin values at approximately 50 ng $mL^{-1}$, for preventing or reversing liver fibrosis [27].

### *Iron deficiency*

**Iron deficiency** and **iron deficiency anaemia (IDA)** may result from the interplay of three different factors: increased iron requirements, limited external supply, and increased blood loss. In Figure 3 main causes are collected and exemplified. Deficiency can be either absolute or functional. In absolute iron deficiency, iron stores are depleted, whereas in functional iron

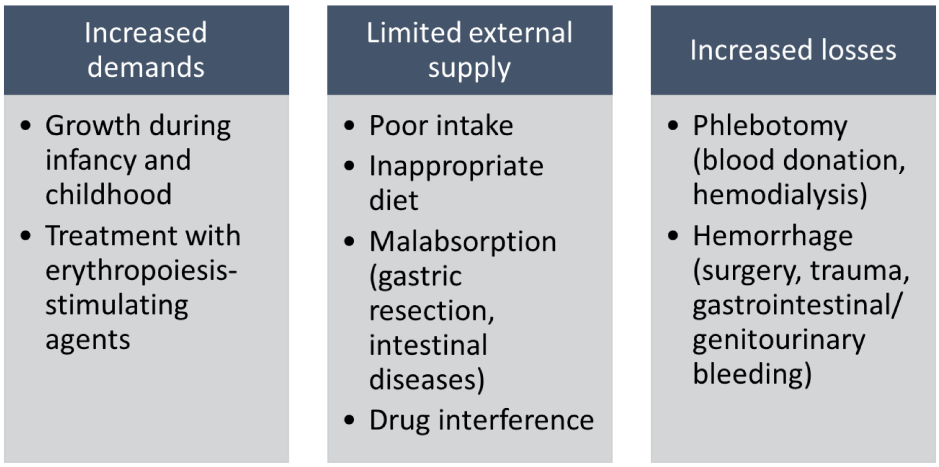


***Figure 3. Main causes of iron deficiency.***

deficiency, iron stores, although replete, cannot be mobilised as fast as necessary from the macrophages of the RES to the bone marrow [9, 27].

A sustained iron deficiency successively lowers the body iron stores which ultimately results in an iron-deficiency anaemia, since there is not enough iron available for erythropoiesis. Iron depletion and deficiency progresses through several stages [33]:

1. Mild deficiency or storage iron depletion: serum ferritin concentrations and levels of iron in bone marrow decrease.
2. Marginal deficiency, mild functional deficiency, or iron-deficient erythropoiesis (erythrocyte production): iron stores are depleted, iron supply to erythropoietic cells and transferrin saturation decline, but haemoglobin levels are usually within the normal range. In addition, plasma iron levels decline and plasma transferrin concentrations (measured by plasma total iron-binding capacity) rise, resulting in decreased transferrin saturation. Serum transferrin receptor concentrations also increase.

3. IDA: iron stores are exhausted; haematocrit and levels of haemoglobin decline; and the resulting microcytic, hypochromic anaemia is characterized by small red blood cells with low haemoglobin concentrations [34].

The term ***anaemia*** (from the ancient Greek ἀναιμία, *anaimia*, meaning 'lack of blood') is used for a clinical diagnosis caused by an inability of erythropoietin tissues to keep normal haemoglobin levels as a consequence of inadequate supply of one or more nutrients leading to a reduction in the total circulating haemoglobin. It might be triggered due to menstruation, childbirth, deficient vegetarian diet, malabsorption of iron, hookworm infections, or excessive blood loss. Among its common adverse effects maternal mortality, low weight at birth, reduced immune-competence, poor cognitive development, behavioural complications, and reduced work capacity are included. Initial diagnostic test is usually based on serum ferritin assessment as it seems to be the most sensitive assay. Dietary diversification, supplementation, and fortification of staple foods and nutrition education are the first approaches to combat iron deficiency anaemia [35].

Apart from these pathologies related to iron deficiency, patients can also suffer **anaemia of chronic disease (ACD)** or anaemia of inflammation which is an accompanying phenomenon of many chronic infections, neoplastic and autoimmune diseases. Anaemia of chronic disease and inflammation involve the same biological pathway: antimicrobial peptides like hepcidin are components of the host defense, synthesized by the liver where the immune response starts in human beings. Due to infection or inflammation, the hepatocytic expression of peptides is accelerated by lipopolysaccharides. As a direct response, an elevated hepcidin expression is detected correlated with the beginning of a hypoferremia after 6 hours [36]. This can be explained by the biochemical reaction of the increased hepcidin concentration. Iron absorption in the intestine decreases and recycling iron from erythrocytes by the macrophages is limited [37]. Moreover, this defense mechanism implies the abnormal behaviour of homeostasis detected in inflammation, accompanied by low serum iron and elevated hepcidin levels which can provoke anaemia. In patients with chronic diseases such as cancer, infections or autoimmune diseases, the same defense strategy is observed.

It can be diagnosed when the following conditions are found:

1. An evidence of chronic inflammation by detecting a high C reactive protein level (*C-reactive protein* (*CRP*), which is an annular, pentameric protein found in blood plasma, whose levels rise in response to inflammation).
2. Haemoglobin concentrations below 13 g $dL^{-1}$ for men and below 12 g $dL^{-1}$ for women.

3. A low transferrin saturation (less than 20 %), but normal or increased serum ferritin concentration (more than 100 ng $mL^{-1}$) or low serum ferritin concentration (30-100 ng $mL^{-1}$) and sTfR/log ferritin ratio under 1 [27].

A diagram summarizing important parameters in order to establish a correct diagnosis is shown in Figure 4 [27].

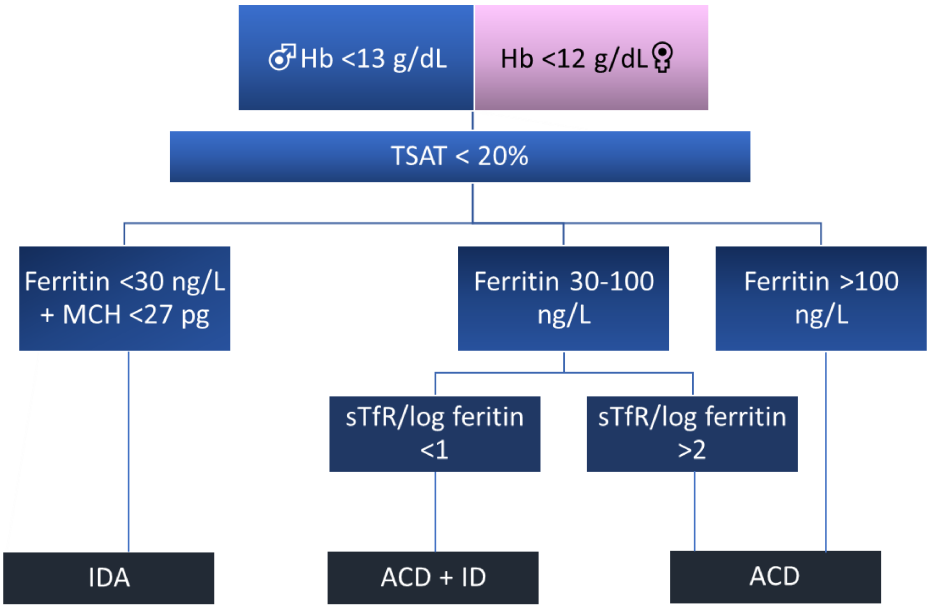


***Figure 4. Diagram for the diagnosis of iron deficiency anaemia (TSAT: Transferrin saturation; MCH: mean corpuscular haemoglobin; sTfR: serum transferrin receptor) [27].***

Iron deficiency affects a significant part, and often a majority of the population in nearly every country of the world. The World Health Organization (WHO), in 1992, estimated that 37 % of all women were iron deficient [38]. Additionally, pregnant women are at higher risk of preterm delivery when anaemic [39]. For these reasons, anaemia is considered as a major contributor to maternal mortality in the developing world. The WHO reports that anaemia causes the 20 % of maternal deaths [40, 41]. In a recent analysis of global anaemia burden, largely unchanged 13 years after the WHO report, Kassebaum et al., estimated that over 30 % of the world's population is anaemic, the majority being due to iron deficiency [42]. In addition to anaemia, iron deficiency causes decreases in energy, activity, quality of life, cognitive function, sexual function, and work productivity [43–46]. Moreover, iron deficiency in neonates is associated with delayed growth and development and a statistically significant decrement in cognitive function, including behavioural abnormalities which persist up to 10 years after iron repletion [47]. Extrapolating the data to years

lived with disability worldwide, 68.4 million human years were negatively impacted by anaemia in 2010 [48, 49].

### 1.3.2. Treatments to overcome iron deficiency

**Oral iron therapy** has a long and rich history as it has been used to treat the anaemia for more than 300 years. According to Stockman's review in 1893, Sydenham recognized the importance of iron replacement in chlorosis already in 1681 [50]. However, it was not until the 19$^{th}$ century when Pierre Blaud, the French physician who introduced pills containing ferrous sulphate, reported cures [49].

Oral iron supplements are an inexpensive and effective way of treating the majority of iron deficient states. However, it is important to remember that duodenal absorption of iron is limited and only a 10 % of the ingested non-haem iron is absorbed by the duodenum under normal steady-state conditions (approximately 1 mg/day). It was observed that duodenal absorption of iron is increased in iron-deficient states [51], however it is generally assumed that 25 mg of elemental iron is sufficient to essentially saturate the duodenal absorptive capabilities. Oral iron therapy is usually best carried out in 3-4 divided doses per day, with a total of 150-200 mg of elemental iron for adults or 6 mg iron/kg body weight in children [52].

Different preparations are available for oral iron supplements. These preparations are based on either the iron ferric or the iron ferrous salt forms, coated by shells of diverse nature (amino-acid chelates, carbonyl iron, polysaccharide-iron complex, combination products, extended-release products, etc.). Iron needs to be in the ferrous form to be absorbed by the intestinal mucosa. Thus, ferric forms need to be reduced to ferrous first, for optimal absorption. Since food can decrease absorption of iron up to 50 %, iron supplements should ideally be taken with an empty stomach. Haem-iron preparations are also available. While commercial forms of haem iron polypeptide are more expensive than the common iron salts, they represent an attractive alternative for those patients who cannot tolerate iron salts and who have reacted to or refuse parenteral iron replacement. Although this form of iron is better absorbed that iron salts, it is derived from animal sources and due to this in many countries, it is considered a "*medical food*" rather than a dietary supplement [53].

Among the most common causes why oral treatment can fail or induce undesirable responses are the following:

- Lack of adherence to therapy or insufficient length of therapy for the degree of iron deficiency.
- Concomitant/causal underlying blood loss pathology not resolved.
    - Poor duodenal absorption (gastrointestinal pathology associated)
    - Insufficient gastric acidity
    - Chemical inhibition of absorption (lead-aluminium)
- Side effects (nausea, constipation, upper gastrointestinal irritation).

Gastrointestinal side effects are the most frequent side effects reported for oral iron therapy affecting up to 70 % of patients [54]. In addition to diarrhea or constipation, upper gastrointestinal symptoms include nausea, abdominal discomfort/pain, and more rarely vomiting. The symptoms appear mostly in the first hour after the ingestion of iron supplements and may be alleviated by a reduction in the dose. In pregnant women, who already suffer from constipation due to elevated progesterone levels which slow bowel transit and pressure from the enlarging uterus on the rectum, oral iron may worsen symptoms.

Recently, several iron preparations that claim superior tolerance are marketed. These preparations often show a slow release property and some of them deliver the iron further down the intestinal tract. Although they seem to be better tolerated, these preparations may not be absorbed so efficiently as the cells with the greatest ability to absorb iron are found in the duodenum and proximal jejunum. In this sense, new studies are being developed trying to improve iron bioavailability with minimum side effects [55] and providing a better understanding about iron supplements effects, their dose dependence and the corresponding impact on iron absorption levels [56].

On the other hand, oral iron therapy should not be considered for patients on haemodialysis therapy and cancer patients receiving erythropoiesis-stimulating agents (ESA). In those cases, it has been proven that the addition of intravenous iron increased efficacy of ESA in cancer patients [52, 57].

For those contraindicated cases, intolerant of or unresponsive to oral iron, **intravenous iron** is an attractive and effective alternative. However, it is generally supposed by most physicians that parenteral iron is dangerous and associated with anaphylactic shock and death. The evidence actually indicates that this perception is incorrect but persists because of misinformation and misinterpretation of the incidence and clinical nature of infusion reactions associated with the administration of parenteral iron, especially in former times [49, 58].

Parenteral iron was first introduced in the early 20th century. Ferric hydroxide solutions were injected subcutaneously and intramuscularly into patients with hypochromic anaemia, and the observed increments in haemoglobin were proportional to the amount of iron administered. The lack of a carbohydrate shell resulted in immediate iron release and severe toxic reactions that led to use this therapy only in extraordinary circumstances [59]. Fortunately, in successive decades improvements in the intravenous preparations were accomplished and different biocompatible shells and iron nanoparticles cores are being commercialized with more effective and safer results for the patients. In fact, they present several advantages over oral supplementation: intravenous iron enables a fivefold erythropoietic response to significant blood-loss anaemia in normal individuals [60], Hb starts to rise after a few days, the percentage of responding patients is higher and iron stores are replete [27, 61]. Modern formulations in the market will be discussed in detail in following sections.

In general, intravenous iron administration is indicated in the following situations:

- In acquired or hereditary decreased intestinal iron absorption and/or liberation of iron from macrophages. Patients with high hepcidin levels secondary to any kind of inflammation [62] or cases where, because of surgery, intestinal iron absorption is abolished, e.g. post gastrectomy, are included.
- In cases with true severe iron deficiency due to constant severe iron bleeding (Rendu-Osler-Weber disease) [63] or because of increased iron needs (pregnancy) or a mixture of both previous situations (post-partum anaemia).
- As it was previously mentioned, in situations of functional iron deficiency particularly when an erythropoietin stimulating agent (ESA) is used such as in renal anaemia, anaemia of cancer patients and autologous blood donation before elective surgery.
- In cases where there is a short time to surgery [64].
- For intolerant patients to oral treatment or when there is a failure with such strategy.

Although parenteral iron efficacy for treating anaemia has been consistently proven in a variety of clinical settings [65], intravenous preparations have been reported to cause anaphylactoid reactions characterised by nausea, hypotension, tachycardia, chest pain, dyspnoea (lung oedema) and bilateral oedema of the hands and feet. Moreover, current information on the relationship between intravenous iron and infection, and between intravenous iron and oxidative stress, deserves special consideration. Elemental iron is an essential growth factor for bacteria with many species expressing iron transport proteins that compete with transferrin, and it has been suggested that patients with iron overload are at increased risk of infection [66]. The

evidence argues for caution in prescribing intravenous iron [67] and new insights are necessary to obtain the ideal formulation.

#### *1.3.2.1. Iron salts*

As it was commented before, oral treatment is mainly based on the use of iron salts. Most frequently used preparations are ferrous sulphate and ferric preparations with an iron polymaltose complex. They vary in their bioavailability, efficacy, side effects, and cost depending on chemical state of iron, salt biocompatibility or galenic forms. Table 4 shows most extended oral formulations, galenic form of administration and the percentage of elemental iron in each one.

**Table 4. Oral iron preparations in the market.**

| Formulation | % Elemental iron (w/w)[53] | Galenic form |
|---|---|---|
| **Carbonyl iron (Fe (0))** | 100 | Tablets, suspension, chewable tablets |
| **Ferric citrate ($Fe^{3+}$)** | 18 | Capsules |
| **Ferrous bisglycinate ($Fe^{2+}$)** | 20 | Capsules, tablets |
| **Ferrous fumarate ($Fe^{2+}$)** | 33 | Tablets, chewable tablets |
| **Ferrous gluconate ($Fe^{2+}$)** | 12 | Tablets |
| **Ferrous sulphate ($Fe^{2+}$)** | 20 | Oral solution, tablets, enteric-coated tablets, film- coated tablets |
| **Ferrous sulphate anhydrous ($Fe^{2+}$)** | 30 | Capsules, tablets, extended- release tablets, capsules |
| **Polysaccharide-iron complex ($Fe^{3+}$)** | 100 | Capsules, solution, film- coated tablets |

Ferrous sulphate preparations usually present good bioavailability, while bioavailability of some other iron ferric preparations is 2 to 3 times less than conventional ferrous salts [68]. This is due to the extremely poor solubility of ferric iron in alkaline media and the fact that ferric iron needs to be transformed into ferrous iron before being absorbed [69].

Despite the wide use of the ferrous salts in cases of iron deficiency, they have lately come under the spotlight in high-profile intervention trials as they may enhance systemic infection rates, induce undesirable changes to commensal bacteria of the colon and increase proinflammatory signalling of the gut epithelium. Moreover, concerns over 'available' iron in the colon as a risk

factor for colorectal carcinogenesis are being reported, showing a possible failure in these treatments and questioning their effectiveness [70, 71].

On the other hand, some forms of ferric iron (e.g. ferric pyrophosphate) are considered safer and better tolerated in the gut lumen than $Fe^{2+}$ but are still poorly absorbed. Chelation may overcome the issue of oral $Fe^{3+}$ bioavailability but then pronounced risk enhancement of colon cancer was detected in rodent models using EDTA [72] or citrate [73] as chelating agents.

Additionally, it should be remarked that non-absorbed iron salts may produce a variety of highly reactive oxygen species including hypochlorous acid, superoxide and peroxides leading to a possible digestive intolerance, causing nausea, flatulence, abdominal pain, diarrhea or constipation, and black or tarry stools, and perhaps an activation of inflammatory bowel disease. Therefore, lower doses of iron salts (50-100 mg of elemental iron) would be always preferable [27].

#### *1.3.2.2. Iron nanoparticles*

Nanoparticulate pharmaceutical drug delivery systems are widely used in pharmaceutical research and in clinical settings to enhance the effectiveness of diagnostic agents and drugs, including anticancer, antimicrobial and antiviral drugs [74]. The types of nanocarriers that exist are diverse and include the following: liposomes, polymeric nanoparticles, polymeric micelles, silica, gold, silver and other metal nanoparticles, carbon nanotubes, solid lipid nanoparticles and dendrimers. Thus, they can be separated into two broad categories: inorganic (metallic, oxides, etc.) and organic nanoparticles (polymeric, micelles, liposomes, etc.).

The main reasons behind the interest in nanoparticle technologies are the advantages they present in comparison to many ordinary pharmaceuticals: they can be designed and formulated to offer enhanced drug protection, controlled release, extended circulation and improved targeting to diseased tissues. Moreover, some specific nanoparticles benefit from stimuli-responsive functions that come from their surface plasmon resonance or magnetic responsiveness (e.g. magnetic resonance imaging) and analogous drugs cannot offer [75]. The use of nanoparticles can overcome several problems that are associated with traditional drugs, such as poor aqueous solubility, low bioavailability and nonspecific distribution in the body [76]. There are several studies demonstrating the increase of bioavailability when materials are prepared in the nanometer size range [77, 78]. In fact, there are evidences to believe that when nanocarriers are used for oral intake of iron, iron absorption increases 1.35 times compare to the reference ferrous

sulphate [79]. Moreover, *in vitro* assays showed that iron absorption from nanoparticles containing iron was 13.42 % more than ferrous sulphate [80]. Therefore, it is expected that nanoparticulate iron improves significantly bioavailability, minimizing doses required in the treatment, and consequently leading to reduced side effects in the gastrointestinal system [81, 82].

#### *1.3.2.2.1. Parenteral treatment*

Iron-replacement therapies for treatment of anemia are one of the clinical areas where nanoparticles have made a significant impact [83–85]. These nanoparticle approaches come from the need to address toxicity issues associated with the injection of free iron [86].

Structurally, all intravenous iron agents are colloids that consist of spheroidal iron-oxyhydroxide nanoparticles of less than 10 nm surrounded by a shell of carbohydrate as stabilizer that slows down the release of bioactive iron, maintains the resulting particles in colloidal suspension and protects the mineral core against further polynuclearization [87]. Different carbohydrates have been used as coating of the particles and examples of commercial formulations are included in Table 5 [83, 88].

The kinetic and thermodynamic stability of these formulations (mainly driven by the interaction of the organic shell with the metallic core) condition their mode of action in biological media. The mechanism of iron release depends on the lability of the bond in the complexes so the weaker the bond, the higher the bioavailability of iron in bloodstream [89].

In addition to their use as drug carriers and contrast agents in preclinical and clinical setting, iron oxide nanoparticles have recently revealed a hidden intrinsic therapeutic effect on early tumours. Zanganeh et al. reported that tumour cells co-injected with ferumoxytol exhibited a markedly delayed growth rate compared with tumour cells injected without addition of ferumoxytol [90].

**Table 5. Classification of intravenous iron NP preparations according to the nature of the binding.**

| | **Type 1** | **Type 2** | **Type 3** | **Type 4** |
|---|---|---|---|---|
| **Compound** | -Ferric carboxymaltose<br>-Iron dextran<br>-Ferumoxytol | -Iron sucrose | -Sodium ferric gluconate<br>-Iron(III)-citrate<br>-Iron(III)-sorbitol | -Iron(III)-citrate + Iron(III)-sorbitol + iron dextrin<br>-Sodium ferric gluconate + iron sucrose |
| **Commercial name** | Ferinject®<br>InFeD®<br>Cosmofer®<br>Imferon®<br>Dexferrum®<br>Feraheme® | Venofer®<br>Fesin® | Auryxia™ | Jectofer®<br>Ferrlecit®<br>Nulecit® |
| **Characteristics** | Robust, strong | Semi-robust, moderately strong | Labile, weak | Mixtures containing at least two different iron complexes |
| **Molecular weight (Da)** | > 100000 | 30000-100000 | < 50000 | < 50000 |

#### *1.3.2.2.2. Oral supplementation*

The physiology of the gastrointestinal tract can lead to poor absorption and availability of the drugs or actives because of the low mucosa permeability and drug degradation prior to absorption. In fact, drugs should go through the stomach, intestinal lumen, the mucus membrane coating the intestinal epithelium, and finally the epithelium itself after oral administration. Nanomedicine offers improvement of oral delivery by bioavailability enhancement, adverse-effect minimization, and food-effect mitigation. By using nanocarriers, dissolution rate of poorly soluble molecules in the gastrointestinal tract can increase significantly. The nanocarrier systems provide intimate contact with the gastrointestinal epithelium, prolonging residence time and improving permeation for drug delivery [91].

In the particular case of the oral treatment for iron deficiency anaemia, iron nanoparticles are mainly found related to encapsulation strategies. This process consists on a micro-packaging where a great variety of iron compounds are protected with different matrix materials leading to a wide range of size particles (from millimetres to nanometres) by using diverse methodologies [92]. Main reasons to encapsulate iron for the treatment of anaemia are:

- The enhancement of non-haem iron bioavailability by protecting iron compounds through the gastrointestinal path;
- The decrease of gastrointestinal side effects commonly associated to iron salts (e.g. abdominal pain, sickness, diarrhoea, constipation);
- The reduction of iron precipitation in the stomach by selecting certain encapsulant materials so that the release of the mineral can be reduced to a minimum and totally degraded in duodenum, where iron is absorbed (*controlled release*);
- The possibility to mix different iron sources in the same nanocapsule so it can be combined with compounds which promote iron absorption (e.g. haem/non-haem, ascorbic acid).

It is observed that encapsulated iron increases efficiency by improving the bioavailability and reducing its negative organoleptic characteristics. It has shown a significant impact on haematological indexes and thus, this strategy provides a competitive alternative in the food fortifications and oral supplements for the treatment of anaemia [93].

In pursuit of strategies for optimal oral iron supplementation designed studies have shown that $Fe^{3+}$ is well absorbed from ferritin. Ferritin is found in both meat and plant-based foods of the human diet: it is composed of a protein shell with a ferrihydrite-like mineral core. Ferrihydrite is a poly oxohydroxide Fe(III) nanoparticle (about 2- to 5-nm diameter) and it is surrounded by a soluble protein coat which not only prevents the uncontrolled growth and coalescence of the small mineral particles into larger insoluble aggregates, but also limits the accessibility of cell constituents to the iron mineral [94]. However, it is still unknown whether the protein shell and ferrihydrite-like core of ferritin controls the slow release of $Fe^{3+}$ ions from the gastric environment, or, if entire ferritin or the protein-detached mineral nanoparticle is rapidly emptied from the stomach, endocytosed by the enterocytes and broken down via intra-lysosomal pathway [95, 96].

Although ferritin is an effective, bioavailable form of dietary iron, supplementation with pure ferritin would be immensely challenging due to the required scale of purification or the complexity of in vitro synthesis, leading to expensive overall costs. As an alternative, synthetic routes to get the ferritin core model were assayed using different low-molecular-weight organic acids as ligands with promising results [71, 97].

### 1.3.3. Pharmacokinetics of nanoparticles

A nanodrug system can offer several pharmacokinetic advantages such as specific drug delivery, high metabolic stability, high membrane permeability, improved bioavailability and long

duration of action. By altering these pharmacokinetic properties of nanodrugs, they can become drugs of promising efficacy [98]. These characteristics are determined by particle size, chemical structure, and surface chemical characteristics and absorption, distribution and clearance pathways will depend on them.

Generally, nanomedicines can be classified according to their pharmacokinetic properties [99]. A classification example is collected in Table 6.

**Table 6. Classification of nanodrugs considering pharmacokinetic properties.**

| Formulations | | Pharmacokinetic properties | |
|---|---|---|---|
| | | **Advantages** | **Disadvantages** |
| **Dendrimers** | Polysine<br>Poly(amidoamine)<br>PEGylated polylysine<br>Lactoferrin-conjugated | - High permeability<br>- Release control<br>- Drug-selective delivery<br>- Improved solubility | Limit of administration routes |
| **Engineered materials** | Nanocrystal<br>Nanosized<br>Amorphous | - Improved systemic exposure<br>- Increased retention time in mucus<br>- Various routes of administration | Insufficient persistent emission |
| **Lipid nanosystems** | Emulsion<br>Liposome<br>Solid lipid<br>Nanoparticle | - Degradation or metabolism of formulated materials<br>- Improved systemic exposure<br>- Drug-selective delivery<br>- Accumulation in tumour cells | - Quick removal by RES uptake<br>- Limit of administration routes |
| **Micelles** | | - High permeability<br>- Improved solubility<br>- Improved systemic exposure | Insufficient persistent emission |
| **Polymeric nanoparticles** | Ethyl cellulose/casein<br>PLGA alginate<br>PLGA-PEG<br>Hydrogel<br>Albumin<br>Chitosan analog | - Stable drug release in vivo<br>- Increased retention time of drug | - Required initial burst protection<br>- Limit of administration routes |

#### *1.3.3.1. Administration route*

The administration route determines whether the action will be systemic or local. Also, the physicochemical characteristics of nanoparticles and the ligands employed affect the uptake. The

choice of local administration route depends on the target region. If the target is the liver or spleen, intravenous route is the best alternative. In the case of muscle or skin targeting, the route used can be topical, intramuscular, intradermal or subcutaneous. Whereas oral or intranasal administration are used in the case of targeting the mucosa. The advantage of these routes is the reduction of systemic toxicity associated. In this case, mucoadhesive nanoparticles are more useful because they increase the residence time at the absorption site. Considering this characteristic, different nanosystems, such as liposomes and polymeric nanoparticles, have been designed for treatment of pulmonary infections through inhalation [100, 101].

#### *1.3.3.2. Distribution*

Nanoparticle size and physicochemical characteristics of the nanoparticle surface play a decisive role in uptake and other important processes like biodistribution or clearance. Uptake can occur through different mechanisms such as phagocytosis, macropinocytosis or endocytosis. This mainly depends on size, being the endocytosis pathway the most common one, owing to the typical small size of nanoparticles. Moreover, the smaller the nanoparticles, the slower the uptake rate by phagocytic cells, and faster biodistribution due to rapid dissolution [102]. Small size is better for reaching the lymphatic system, preventing uptake by RES and guiding distribution inside the cell [103]. In addition, small size is sometimes necessary for nanoparticles to circulate through capillaries, sinusoids, tissue structures and membrane or mucosa pores in order to reach extra- and intracellular compartments [104]. So, it is proved that smaller sizes increase the drug loading efficiency and the antimicrobial effect, lowering minimum inhibitory concentration (MIC) [101].

Another factor affecting biodistribution and uptake is the zeta(ζ)-potential because interactions with proteins of the blood, tissues or mucosa, and with the cellular membrane are charge dependent. In fact, these interactions will be responsible for the amount and type of proteins adsorbed; the adhesion or not to the mucosa and for how long; the endocytosis mechanisms; and biodistribution. The increment of hydrophobicity also affects the distribution as it decreases the diffusion kinetic in mucus, favours cellular uptake (due to interactions with the lipids of the cell membrane), and influences output from endosome and drug release [101, 105].

Distribution and uptake can also be driven by the addition of specific compounds or ligands to the nanoparticle surface which favour interactions with the cell membrane, enhancing the recognition of nanoparticles by cells. As an example, saccharide ligands have shown to be useful for targeting to macrophages and phagocytic cells [106]. So, the ligand is chosen depending on its

stability and selectivity considering the target cells, too. The availability and interactions with immunologic cells or with membranes must be also taken into account. Ligands also play an important role in intracellular biodistribution of the particle, because the carrier could remain within the endosome or escape from it to reach other organelles in the cytoplasm, depending on the ligand nature.

Once nanoparticles reach the target site, the drug must be released. Some polymers can control and self-regulate drug delivery by modifying their structure, which may occur immediately or be sustained over a certain time. Modifications are induced by physiological conditions such as pH, hydrophilic/hydrophobic equilibrium, ionic strength or presence of specific molecules. The pH can modify the kinetics of release, thus protecting the drug from degradation in undesirable conditions or, conversely, promoting nanoparticles destruction and total release of the drug [107]. Similarly, ionisable polymers can modify their size, solubility and fluorescence due to changes in ionic strength [108]. Changes can also be provoked by external stimuli, such as electricity, magnetic fields, ultrasound or light which strengthen the drug release [109]. Therefore, the stimulus can be used in different ways to favour the treatment [101].

#### *1.3.3.3. Elimination*

Elimination pathway has a crucial role in determining chronic toxicity of nanoparticles. When drug release is completed, nanoparticles must exit the cell if they have not been degraded. The exocytosis rate depends mainly on particle composition, ligands and surface properties. In this sense, cationic nanoparticles have a slow rate of exocytosis from macrophages because they agglomerate intracellularly [110], whereas PEG nanoparticles have the highest exocytosis rate because they hardly have interactions with intracellular proteins [111].

Eventually, nanoparticles are excreted from the body. In case they are smaller than 5 nm, it can occur by urine. Bigger ones are reabsorbed and trapped in the collagen network of the glomerular basal membrane, where they are taken up by macrophages [112]. If they are smaller than 200 nm, they are mainly excreted in the bile, but the process is slow and saturable, and accumulation is possible. However, this effect is of concern in the case of naked nanoparticles. According to some clinical trial results, this effect is reduced or even disappears when nanoparticles are protected with ligands or drugs [101, 112, 113].

### 1.3.4. Impact evaluation in biological media: nanotoxicity

Nowadays, our exposure to nanomaterials is significantly increasing but, there is still little understanding about toxicological properties of nanoparticles and their long-term impact on human health. There is a considerable gap between the available data on nanomaterials production and their corresponding toxicity evaluations.

The most challenging aspect with the use of nanotherapeutic products is accumulation, analysis, classification, and characterization of the safety data about their clinical applications. Due to their small size, nanoparticles represent a huge health hazard since they can penetrate the barriers present within the human body and entering the organism by inhalation, ingestion, skin penetration or injections. Consequently, nanoparticles have the potential to interact with intracellular structures and macromolecules for long periods of time. There are evidence of these particles causing serious harm to cellular membranes, organelles and DNA owing to generation of free radicals [114]. Nanotoxicity assessment must be taken in consideration, especially in the case of new nanomaterials in the early stages of production [115].

Physicochemical properties such as chemical composition, small size, large surface- to-volume ratio, and surface property influence the biological interaction of nanoparticles and thus, they must be evaluated for determination of potential toxicity of nanomaterials [116].

**Particle size** and **surface area** are crucial material characteristics, as interactions between nanomaterials and biological organisms typically take place at the surface of the nanosystem. As the size decreases, the surface area increases, and a greater proportion of atoms or molecules will be displayed on the surface of the particle rather than within the bulk of the material. Thus, the nanomaterial surface becomes more reactive with surrounding biological components with decreasing size, and the potential catalytic surface for chemical reactions increases [117].

**Shapes** and aspect ratios are key factors to determine the toxicity of the nanoparticles. Nanomaterials can present different shapes including fibres, spheres, tubes, rings and planes and this can influence the membrane warping process during particle internalization via endocytosis or phagocytosis [118].

Importance of **chemical composition** has been also demonstrated, especially concerning cell molecular chemistry and oxidative stress [119].

The potential adverse effects of nanoparticles maybe eliminated or minimized by incorporation of **surface coatings**. Proper surface coatings can stabilize particles, avoid agglomeration and prevent from dissolution and release of toxic ions [120].

**Surface charge** also plays an important role in toxicity, as it influences the adsorption of ions and biomolecules that may change organism or cellular responses toward particles. Moreover, surface charge is a major determinant of colloidal behaviour, which influences the organism response by changing the shape and size of nanoparticles through aggregate or agglomerate formation. In general, cationic nanoparticles are considered more toxic than neutral or anionic ones, possibly due to their high affinity towards the negatively charged plasma membrane. Therefore, nanotoxicity must be evaluated by changing nanoparticle properties systematically, one at a time [117].

Additionally, the **medium** that contains nanoparticles can affect negatively the toxicity of nanomaterials. Proper and stable dispersion of nanoparticles are necessary for their biological distribution and activity. However, the tendency to agglomerate makes the use of dispersion or wetting agents essential. These media would improve the physicochemical and solution properties of nanomaterials formulations but could have adverse effects on the safety of these materials [121, 122].

In the case of iron oxide nanoparticles, the information reported in the literature may be conflicting. Depending on the chemical nature of their coating, iron nanoparticles do not have the same behaviours in biological systems, e.g. they can be internalized into cells or attached onto the cell membranes, leading to cell death or cell proliferation. Uncoated iron-based nanoparticles induce a dramatic decrease in the metabolic activity and proliferation of human cells. Generally, the coating of these nanoparticles seems to be of great importance with regard to cell adhesion, internalization efficiency, and cytotoxic effects [123–125].

#### *1.3.4.1. Cell toxicity*

Due to the effect of the aspects previously commented, it is expected that nanoparticles exert several mechanisms by which they affect cell homeostasis, apart from some nanoparticle-type specific considerations.

As nanoparticles have defined physical dimensions, the intracellular volume they occupy can lead to alterations in cellular morphology or affect the structure of the cellular cytoskeleton network. For different types of nanosystems, the effects described have been dependent on intracellular nanoparticle concentration and transient, where after recurrent cell divisions, the intracellular nanoparticle concentrations decrease exponentially, and the effects are no longer observed.

Inorganic nanoparticles can also interfere with the delicate balance of cellular homeostasis and hereby alter complex intracellular signalling pathways, resulting in a cascade of possible effects. These interactions can occur by several mechanisms, such as:

(1) Genotoxic effects caused by high levels of ROS (explained more in detail in the following section).
(2) Modified protein or gene expression due to the perinuclear localization of the particles which may hinder the functioning of the transcription and translation steps.
(3) Altered protein or gene expression levels due to leaching of free metal ions.
(4) Different activation status of proteins by interfering with stimulating factors such as cell-surface receptors.
(5) Altered gene expression levels in response to the cellular stress induced by the nanoparticle.

As it was already mentioned, the high surface area and high local charge densities of nanostructures generate a large area ready to interact with surrounding biological molecules. When the nanoparticles are subjected to physiologically relevant conditions, the surface charges favour the binding of available serum proteins, leading to a so-called protein corona [126]. The presence of serum proteins in the surrounding media of nanoparticles automatically lead to a tight association of both entities, unless a specific nanoparticle coating which inhibits protein attachment is employed. In terms of possible biological/toxicological effects, it was further observed that the proteins interacting with nanoparticles undergo conformational changes. These conformational changes could have profound effects on cellular stability since our immune system may then not recognize these proteins as native but rather as foreign objects and may try to eliminate them, inducing then autoimmunity. Binding of serum proteins to nanoparticles may also directly affect their endocytic route and degree of cytotoxicity [127, 128].

Currently, most nanoparticle-related cytotoxicity data are generated by individual studies, with a few specific parameters monitored for a certain type of nanostructure and a certain cell line. To enhance the comparison of generated data and improve our understanding in this matter, there is an urgent need for standardization of the protocols used. For a specific sort of nanoparticle, the range of concentrations and incubation times employed should always be precisely defined and should be the same for all studies. The type of cells used is also of great importance as different cell types can react quite differently even for the same type of nanomaterial. In general, those cell lines which are most involved in the biomedical applications

of the nanoparticles should be preferably tested (epithelial, endothelial cells), or multiple cells derived from the different germ layers.

Standardization is also necessary concerning the kind of assays used. The *in vitro* methods are ideal in nanotoxicology research because they can produce reproducible results rapidly and inexpensively without the use of animals [121]. Basically, to assess the toxicity profile of nanoparticles, two main approaches have been established:

1) Functional assays evaluate the effects of nanoparticles on cellular processes;
2) Viability assays probe whether the nanoparticles cause death in a cell or a system of cells [117].

Cell viability is quite a general term and can be investigated by numerous assays which determine one or more cellular parameters:

a. WST or MTT assays measure mitochondrial activity
b. Lactate dehydrogenase (LDH), trypan blue or propidium iodine assay check cell membrane permeability
c. Calcein AM for the assessment of intracellular esterase activity
d. Fluorescent Annexin V or caspase substrates focus on apoptosis indicators.

Although the cytotoxic effects of iron oxide nanoparticles are known, the mechanism(s) of their induced cytotoxicity is not clearly understood. Moreover, there is a lack of consensus among the different studies found in the literature, but it is clear that the surface coatings and particle size are crucial for iron nanoparticle-induced effects, as they are critical determinants of cellular responses, intensity of effects and potential mechanisms of toxicity. In order to make results comparable across these investigations on iron nanoparticles with different coatings and characteristics, the use of standardized methods would be highly desirable [129].

#### *1.3.4.2. Oxidative stress*

The generation of reactive oxygen species (ROS) by cultured cells incubated with nanoparticles is quite a common phenomenon. When cells are exposed to environmental stress such as pathogens or heat, they can generate chemically active oxygen-containing molecules [128]. ROS can be classified into two different types: radical ROS (superoxide anion and hydroxyl radical) and non-radical ROS (hydrogen peroxide and hypochlorous acid). Cells have defense mechanisms to clear radicals, such as glutathione redox system (GSH). Under normal conditions, a balance exists between the generation and clearance of radicals that does not negatively affect the body. However, when the increase in ROS is too high that it cannot be handled by normal removal

mechanisms, ROS accumulate and can damage the structure of cells, affecting their functions. ROS can oxidize membranes, and the end-product of lipid oxidation is malondialdehyde (MDA). Therefore, ROS, GSH, and MDA are usually used as biomarkers of oxidative damage to measure the toxicity of a material [116].

There are different pathways by which nanoparticles can induce oxidative stress:

a) A nanomaterial present in the acidic environment of lysosomes can induce ROS by direct reactivity of their surface coating, degradation of the coating and direct interaction of the acidic media on the metal surface or degradation of the whole nanoparticle and production of ions ($Fe^{2+}$, $Cd^{2+}$) which can induce ROS species by various chemical reactions.
b) They can also directly interact with oxidative organelles such as the mitochondria by destabilizing the outer membrane, deregulating the mitochondrial membrane potential and disrupting the electron transport chain of the oxidative phosphorylation.
c) Nanoparticles can directly interact with redox active proteins such as NADPH oxidase and hereby stimulate large ROS production in cells of the immune system.
d) Interaction of nanoparticles with surface located receptors can lead to receptor activation and triggering of intracellular signalling cascades (activation of second messenger or calcium waves), finally resulting in expression of stress response genes which can upregulate ROS (Figure 5 [128] (d)).

As ROS has been claimed to be of major importance in the toxicological profile of nanoparticles, the evaluation of elevated ROS levels is of crucial importance. Commonly,

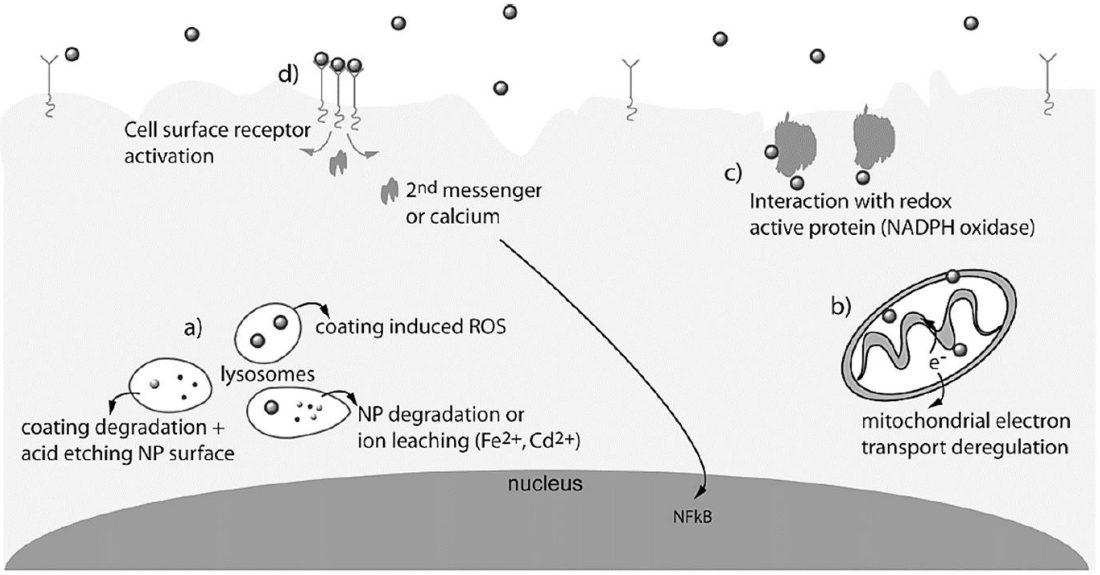


***Figure 5. Graphic overview of different pathways to induce oxidative stress from nanoparticles [128].***

fluorescent probes such as dichlorodihydrofluorescein and its derivatives are used to assess ROS levels. It is important to use multiple time points to accurately define the maximal ROS levels, as the kinetics of ROS induction can largely differ between various nanoparticles and it is also important to know whether the effects are transient or more long-lasting. As the link between elevated ROS levels and cytotoxicity is unclear, it is also important to further investigate any possible secondary effects in case significant ROS induction is observed. Useful parameters to study would be mitochondrial metabolism (using fluorescent probes), lipid or protein peroxidation, cytoplasmic calcium levels, cytoplasmic redox state (by measuring glutathione levels) or DNA defects [128].

Iron, which plays an active redox-catalytic role in many energy-transfer or electron-transfer processes due to its partially filled *d* orbitals and variable oxidation states, is intimately linked to ROS chemistry. Successive one-electron or two-electron reduction of molecular oxygen to water in the aqueous solution yields a series of ROS such as superoxide radicals ($O_2^-/HO_2\cdot$), hydrogen peroxide ($H_2O_2$), and hydroxyl radicals ($OH\cdot$). Metal iron and iron oxide nanoparticles can be involved in these redox reactions as a reactant or a catalyst via homogeneous or heterogeneous methods, based on dissolved iron species or solid surfaces, respectively.

Many *in vitro* experiments confirmed the production of these radical species which can be explained in terms of the following reactions:

- The classic homogeneous Fenton reaction, which involves one-electron reduction of hydrogen peroxide by soluble ferrous iron species, generates hydroxyl radicals that are powerful enough to oxidize most organic molecules:

$$Fe\ (II) + H_2O_2 \rightarrow Fe\ (III) + OH^- + OH^{\cdot} \qquad \textbf{(1)}$$

- The non-radical mechanism for the homogeneous Fenton reaction involves the generation of ferryl-oxo complexes, less powerful oxidants compared to hydroxyl radicals, via two-electron reduction of hydrogen peroxide with soluble ferrous iron species:

$$Fe\ (II) + H_2O_2 \rightarrow Fe\ (IV)O^{2+} + H_2O \qquad \textbf{(2)}$$

- The homogeneous Fenton-like reactions, which involve the generation of superoxide radicals, hydroxyl radicals, or ferryl-oxo complexes from hydrogen peroxide and soluble ferric iron species, consist of two steps; a slow one-electron reduction of ferric iron by hydrogen peroxide and a rapid generation of powerful oxidants via reaction **(1)** or **(2)**:

$$Fe\ (III) + H_2O_2 \rightarrow Fe\ (II) + HO_2^{\cdot}/O_2^{-\cdot} + H_2O \qquad \textbf{(3)}$$

- The Haber-Weiss reaction, which involves generation of hydroxyl radicals from hydrogen peroxide and superoxide, can be catalyzed by soluble ferric iron species through reaction **(4)** and **(1)** [130]:

$$Fe\ (III) + HO_2^{\cdot}/O_2^{-\cdot} \rightarrow Fe\ (II) + H_2O/OH^- + O_2 \quad \textbf{(4)}$$

Iron-induced oxidative stress has the following implications: (i) failure in redox regulation leading to DNA damage, lipid peroxidation and oxidative protein damage and free radical-induced activation of signal transduction pathways [131].

In spite of the large number of studies on iron nanostructures, there is still too much unknown about how their intrinsic physicochemical properties affect the redox reactivity of iron nanoparticles. Additional work is needed to characterize the redox activities of these nanostructures under various bio-microenvironmental conditions, which is one of the aims in this study.

## 1.4. Analytical strategies for the characterization and determination of metallic nanoparticles

The analysis of metallic and metal oxide nanoparticles in biological and environmental samples is a complex analytical challenge due to different factors:

- Low concentration level (mg $L^{-1}$ to ng $L^{-1}$) that makes the use of highly sensitive and selective detection techniques essential to obtain low detection limits.
- In complex matrixes, dilution or pre-treatment is a must, with the consequence of decreasing of the metal concentration.
- Nanoparticles characterization may be a difficult task in biological or environment samples due to agglomeration/aggregation or protein corona formation that usually occur in presence of proteins or saline solutions.
- Sample handling during all analytical steps must be careful in order to keep the nature of metallic species in the nanostructure and avoid wrong information about degradation or particle size.
- The target metal, which is in low concentration in the nanostructure, can be found in different species (different size particles, ions, biomolecules, protein complex, etc.) so limits of detection required for the target would be significantly lower than for total concentration, or impossible to differentiate.

- Possible analyte losses or sample transformation during the analytical process are important variables to monitor in order to get reliable results in ultra-trace analysis.

In addition to all these general factors, it is remarkable that nanoparticles in biological matrixes usually present polydispersity and can experience degradation, functionalization, agglomeration and other *in vivo* processes leading to different species formation in the medium. This can affect the separation or speciation strategy chosen, as it should be able to distinguish between nanoparticles, conjugates, agglomerates and free ions. The ideal technique would be able to differentiate among different species without their modification, allowing quantitative recoveries in less time possible with the highest reproducibility.

Analytical chemistry for the determination and characterization of nanoparticles is mainly focused on searching strategies which provide information about chemical composition (core and surface), size/size distribution and shape, agglomeration state and crystalline structure.

As it has already been explained, most of properties and applications of nanoparticles depend on their size. Likewise, their separation is based on particle size or size distribution. In Table 7, a summary of principal techniques used for the characterization of particle size is presented with their major advantages and limitations according to a review from Shang et al. [117]. Most of them will be discussed in more detail in following sections.

**Table 7. Most common techniques to characterize nanoparticle size.**

| Technique | | Advantages | Limitations |
|---|---|---|---|
| **ICP-MS** | *Single Particle mode* | - Determines the particle number concentration (particles/mL) and the mass of metal in individual particles and size distribution | - Does not provide direct information on particle shape or diameter<br>- Minimum particle size is limited by ICP-MS sensitivity, background and dissolved (ionic) element content |
| | *Hyphenated Techniques* | - Minimum particle size is not limited by ICP-MS sensitivity<br>- Determine total metal concentration as a function of particle size fraction | - Do not provide direct information on number of particles or characteristics of individual particles |
| **TEM (Transmission Electron Microscopy)** | | - Direct visualization<br>- High resolution | - NP aggregation during sample preparation<br>- Electron beam damage<br>- Preference for electron-dense atomic species |
| **DLS (Dynamic Light Scattering)** | | - Size distribution information available<br>- Fast, simple | - Signal dominated by larger NPs<br>- Interference from luminescent species |
| **Absorption spectra** | | - Simple, fast | - Applicable to plasmonic (Au, Ag) and semiconductor (CdSe, CdTe) NPs |
| **Analytical centrifugation** | | - Size distribution information available<br>- High size resolution | - Density of NPs needs to be known<br>- Long measurement time |

### 1.4.1. Non-hyphenated techniques

#### *1.4.1.1. Inductively coupled plasma mass spectrometry (ICP-MS)*

Since its development in the early 80s, ICP-MS has become one of the most important techniques in the field of atomic spectroscopy. The technique has been continuously refined over the years and adapted to new requirements, but the basic principle remains nearly unchanged. ICP-MS allows the analysis of gaseous, liquid and solid samples which are introduced as an aerosol into an atmospheric plasma. The plasma torch is the centrepiece of this ionization source and is represented in Figure 6. A plasma torch is composed of three concentric quartz tubes which

different Ar gas flows are injected: a cooling gas flow of ≈ 12-17 L·min$^{-1}$ injected tangentially, preventing the outer quartz tube from melting by physical contact to the extremely hot plasma; an auxiliary gas flow (≈ 0.5-1.5 L min$^{-1}$) applied to change the position of the plasma base relative to the injector tube and prevent it from melting; and the nebulizer gas flow (0.5-1.5 L min$^{-1}$ depending on the applied nebulizer) that allows the introduction of the sample as an aerosol [132,

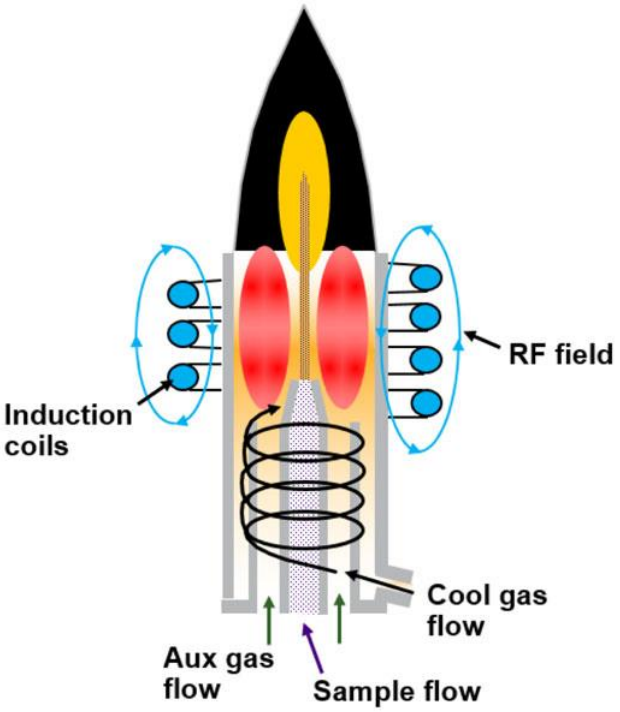


***Figure 6. Schematic setup of the plasma torch in the ICP-MS (source: www.thermoscientific.com).***

133].

The end of outer quartz tube is surrounded by a load coil, typically made from copper. Before plasma ignition, a tangential argon gas flow is injected between the outer and middle tube quartz torch (auxiliary gas). Then, an oscillating electric current (750-1500 W) is applied to the load coil. For power supply, radio frequency (RF) generators using frequencies of 27 MHz are used. As a result, a strong oscillating electromagnetic field is generated at the end of the torch. By introduction of a start ignition spark, free electrons are generated that are accelerated by the influence of the electromagnetic field. The electrons collide with neutral Ar atoms resulting in the formation of further ions by either direct ionization (electron impact) or secondary ionization (charge transfer from ionized Ar species). This process results in the formation of a plasma discharge which is sustained as long as RF power is supplied to the load coil. Since the plasma is consisted of ions, excited ions, electrons, and neutrals it is electrically conductive but neutral to its surrounding (*electroneutrality* of the plasma) [132].

If a sample aerosol, containing the analyte in solution, is injected into the plasma, the droplets are first desolvated by the influence of the plasma temperature (≈ 6000-10000 K). The remaining solid or liquid particles are then vaporized or sublimated. Then, the high energy density in the plasma causes that molecules break down into their atomic components (atomization). Consequently, all structural information is lost and only the total element amount is accessible. Finally, the atoms are excited due to the high plasma temperature. Also, sufficient energy is transmitted to remove an electron from the outer electron shell of the atom, leading to the formation of positively charged ions as well. This process depends on the first ionization energy of the corresponding element. Therefore, all elements having a first ionization potential below 15.75 eV (first ionization potential of Ar) are ionized in the Ar-based plasma. The ionic species generated can be analysed by the mass spectrometer (MS). In this case, the ions must be transferred from the atmospheric pressure of the plasma (≈ 1 bar) to the high vacuum of the mass spectrometric device (≈ $10^{-9}$ bar) thanks to the interface of the ICP-MS. More precisely, ions from the plasma are extracted through two adjacent metal cones: the sampler and the skimmer cone (orifice diameter 0.8-1.2 mm and 0.4-0.8 mm, respectively). Between both cones, a pressure of approximately $2 \cdot 10^{-3}$ bar is maintained by a rotary vane pump. Behind the skimmer cone, the high vacuum part of the MS devices keeps the ion optics, the mass analyser and the detector [132, 134].

The ICP-MS enables a very sensitive and robust determination of a certain hetero atom present in a sample. Moreover, due to the fact that ICP-MS is well suited for gaseous and liquid samples, it can be hyphenated online with powerful separation techniques such as gas chromatography, high performance liquid chromatography or electrophoretic techniques.

In terms of nanoparticle analysis, ICP-MS has demonstrated to be a rapid, accurate, sensitive technique for characterizing and quantifying nanoparticles in a wide range of sample types. The main benefits of ICP-MS for the detection, characterization, and quantification of nanoparticles are related to its high sensitivity and specificity, which can provide additional information compared to other techniques such as dynamic light scattering. ICP-MS is also fast and requires little sample preparation compared to techniques such as scanning or transmission electron microscopy (SEM, TEM), atomic force microscopy (AFM), or separation techniques such as differential centrifugation. Characterization of nanoparticles using ICP-MS detection can be achieved via one of two different strategies: single particle or hyphenated mode [135]. Both will be described in more detail in following sections.

However, ICP-MS analysis implies some limitations related to interferences that can affect sample measurements. There are three major groups of interferences: spectral, matrix, and physical. Each of them is potentially problematic, but modern instrumentation and good software, combined with optimized analytical methodologies, has minimized their negative impact on trace element determinations by ICP-MS [136].

Among the spectral interferences, the most common type is known as a polyatomic or molecular spectral interference, which is produced by the combination of two or more atomic ions. They are caused by a variety of factors but are usually associated with either the plasma and nebulizer gas used, matrix components in the solvent and sample, other analyte elements, or entrained oxygen or nitrogen from the surrounding air. There are several alternatives to avoid these interferences: blank subtraction, matrix modifications, mathematical corrections or chemical separations. But there are other solutions based on instrumental corrections such as the use of collision/reaction cells or a high-resolution mass analyser. In the case of collision/reaction cells, the basis is the use of ion–molecule collisions and reactions to cleanse the ion beam of harmful polyatomic and molecular interferences before they enter the mass analyser. For that purpose, inert gases (mainly He) are used to collide with interferent ions, or reaction gases ($H_2$, $O_2$ or $NH_3$) are applied to convert the ion into a new mass that is not interfered. Thus, collision/reaction cells are showing enormous potential to eliminate spectral interferences and make available isotopes that were previously unavailable for quantitation. However, the best and probably most efficient way to remove spectral overlaps is by the use of a high-resolution mass spectrometer. During the past 10 years this approach, particularly with double-focusing magnetic sector mass analysers, has proved to be invaluable for separating many of the problematic polyatomic and molecular interferences seen in ICP-MS, without the need to use cool plasma conditions or collision/reaction cells [136]. Lately, a more "affordable" alternative that allows removal of isobaric and polyatomic interferences has been developed based on a mass shift mode by using a triple quadrupole system. Basically, it consists on the online configuration of two quadrupoles and one reaction cell between them. The first quadrupole acts as a filter and rejects all masses except analyte mass (analyte and on-mass interferences). Then, analyte reacts selectively with a reaction gas in the reaction cell, turning into a new product ion mass and being differentiated from the interferences that are not reactive. Finally, last quadrupole rejects all cell formed ions apart from analyte product ion, leaving analyte free from overlap. It can only be seen as a reaction cell ICP-MS evolution [137].

Another type of spectral interferences is called "isobaric overlaps" and are produced mainly by different isotopes of other elements in the sample that create spectral interferences at the

same mass as the analyte. For example, both Fe and Ni have isotopes at mass 58. Therefore, any signal measured at m/z 58 will have contributions from both Fe and Ni. To avoid this kind of interferences it is necessary to choose different isotopes of the analyte or apply mathematical corrections [138].

In the case of the Fe, the determination of the four isotopes ($^{54}$Fe 5.845 %, $^{56}$Fe 91.754 %, $^{57}$Fe 2.119 %, $^{58}$Fe 0.282 %) by ICP-MS using single quadrupole mass analysers, is limited by the isobaric and molecular interferences collected in Table 8.

**Table 8. Spectral interferences of the four isotopes of Fe.**

| | **$^{54}$Fe** | **$^{56}$Fe** | **$^{57}$Fe** | **$^{58}$Fe** |
|---|---|---|---|---|
| **Isobaric interferences** | $^{54}Cr$ | | | $^{58}Ni$ |
| **Polyatomic interferences** | $^{40}Ar^{14}N^+$<br>$^{38}Ar^{16}N^+$<br>$^{36}Ar^{18}N^+$ | $^{40}Ar^{16}O^+$<br>$^{40}Ca^{16}O^+$ | $^{40}Ar^{16}OH^+$<br>$^{38}Ar^{18}OH^+$<br>$^{40}Ca^{16}OH^+$ | $^{40}Ar^{18}O^+$<br>$^{40}Ca^{18}O^+$<br>$^{42}Ca^{16}O^+$ |

The most common way to overcome Fe interferences such as the one produced by $^{40}Ar^{16}O^+$ (m/z 55.957) over the most abundant isotope of iron $^{56}$Fe (m/z 55.935) is by using $H_2$ as reaction cell gas [139, 140] and so it was done in this work. Other gases like $NH_3$, $N_2$, CO, $CH_4$, He, Kr, etc. have also been used for the same aim [141]. Similarly, polyatomic interferences of Ar over other isotopes like $^{54}$Fe or $^{57}$Fe can also be reduced by using collision/reaction cells [142, 143].

### *Single Particle detection (spICP-MS)*

Single particle detection or spICP-MS is a relatively simple and direct technique for the determination of particle size and concentration in terms of number of particles present in a sample. The main principle behind spICP-MS is detection of a discrete pulse, originated from ionization of a single particle, using short detection or dwell time. If the particle composition is known, the signal from a single particle event can be correlated to particle mass, and the number of signals detected in the sample to particle number concentration.

It requires an ICP-MS system properly configured and an appropriate dilution of the sample. ICP-MS configuration will be discussed in following sections. This technique enables not only the determination of particle size, but also size distribution with corresponding percentage of each population present in the sample. Number of events or signals per nanoparticle gives information about concentration of particles, while signal intensity is related with the element mass and can

be turned into size particle if particle shape is assumed as perfectly spherical. On the other hand, released ions from nanoparticles (at a sufficiently high concentration to be detected) produce signals in constant intensity pulses [144]. The concentration of these ions is related to the background signal of the analysis and therefore, can be easily calculated using an external calibration.

A proper adjustment of detection time (dwell time) and an accurate concentration of nanoparticles in the sample are critical factors for the optimization of the measurement and key steps to overcome the main limitation of this method in terms of calculations: partial signal counting (too short dwell time) or double counting of particle events (too long dwell time or too high concentration of the sample). Additionally, transport efficiency estimation is the major source of error for the calculation of particle size. In this sense, differences between transport efficiency for the calibration matrix and sample matrix must be taken into account for the calculation [145].

Although the spICP-MS can be a suitable tool for the direct characterization of metallic nanoparticles, it is highly dependent on the signal to noise ratio of the ICP-MS used for the analysis, especially between nanoparticles signal and background caused by the ions. This does not allow to distinguish between small nanoparticles signal and ions in the sample or coming from nanoparticle degradation. Actually, detection limits in terms of particle size for silver, gold, and titanium oxide nanoparticles were recently established at 13, 13 and 91 nm, respectively [146].

### *Laser Ablation coupled to ICP-MS (LA-ICP-MS)*

In addition to quantitative MS-based methods, which allow the quantification of nanoparticles and their elemental composition in solutions, methods that allow similar analysis to be performed on surfaces have also been developed. In Laser Ablation coupled to ICP-MS (LA-ICP-MS), also referred to as "*chemical imaging*" [147, 148], a pulsed laser beam is used to ablate (eject) small quantities of material from the solid surface of a sample, enclosed in a chamber filled with inert gas. The ablated aerosol is transported with the stream of carrier gas to an ICP-MS instrument for elemental and/or isotopic analysis. A schematic set-up of the coupling between the laser ablation and the ICP-MS from Günther et al. [149] is presented in Figure 7.

LA-ICP-MS requires little or no sample preparation, offers good sample throughput and in optimal conditions sample resolution < 1 μm. This resolution can be achieved using a narrow beam

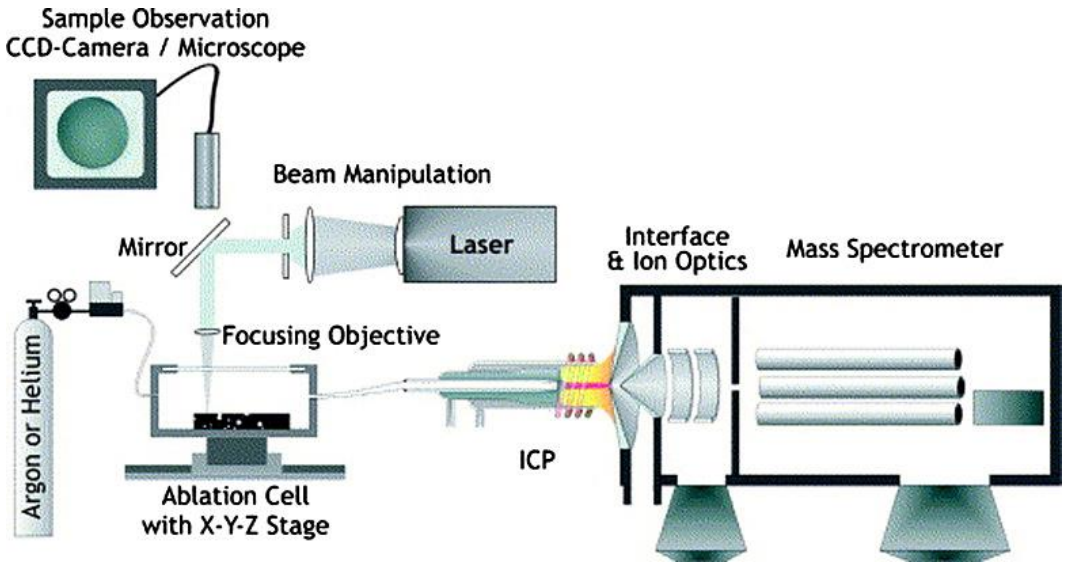


***Figure 7. Schematic set-up of laser ablation system coupled to ICP-MS [149].***

diameter and low laser rastering rate but decreasing the number of detectable atoms in this area and thus, sacrificing analyses time and sensitivity. Still, the µ-range resolution is not enough for the detection of nanoparticles, and for nano-range resolution, additional methodological advances are to be expected [150].

Examples of studies where LA-ICP-MS has been used to evaluate cell–NP interactions include the work of Drescher et al., which demonstrated the applicability of the technique for the quantitative imaging of 50 nm-silver and 25 nm-gold nanoparticles in single eukaryotic cells. Quantification was achieved based on a matrix-matched calibration using nitrocellulose membranes doped with nanoparticle suspension [151]. Böhme et al. applied LA-ICP-MS to study metallic NPs in crustaceans and zebrafish embryos [152] and Managh et al. showed the applicability of LA-ICP-MS for the analysis of single human macrophages exposed to 50 nm Au particles [153]. All these results demonstrate a great potential of LA-ICP-MS for nanotoxicity investigations, nanobioanalytics, and quantitative elemental microscopy.

#### *1.4.1.2. Electron microscopy*

Microscopic techniques are employed for the characterization of nanoparticles in terms of size, morphology, and, in some cases, composition and has made research of these nanomaterials possible. Electronic microscopy (EM) is often used for the characterization of metallic nanoparticles due to sub-nanometer range resolution and the information they can provide about

particle size, size distribution, dispersity, morphology, and aggregation state from the direct visualization of metallic core of nanoparticles [154].

There are basically two alternatives available in electron microscopy: **Transmission Electron Microscopy** (TEM) and **Scanning Electron Microscopy** (SEM). All these techniques use high vacuum mode (at around $10^{-4}$ Pa) which minimises scattering of the electron beam before reaching the specimen. This is important as scattering or attenuation of the electron beam would increase the probe size and reduce resolution.

Among all of them, **TEM** is the most used technique and it is based on the use of a beam of highly energetic electrons that impacts on a sample deposited on an ultrafine grid. On the way through the sample, some parts of the material stop or deflect electrons more than other parts. The electrons are collected from below the sample onto a phosphorescent screen or through a camera. In the regions where electrons do not pass through the sample the image is dark. Where electrons are unscattered, the image is brighter, and there are a range of greys in between depending on the way the electrons interact with and are scattered by the sample. Magnifications of up to 1,000,000 and resolution below 1 nm are achieved routinely. A scale is essential on a TEM image. From this the actual size of structures in the image can be calculated. It also enables the possibility of coupling to other techniques such as Electron Energy-Loss Spectroscopy or energy dispersive X-ray analysis, providing additional information about electronic structure and chemical composition of the nanomaterial, respectively [155, 156].

In summary, TEM is a useful tool for:

- Imaging morphology of samples e.g. view sections of material, fine powders suspended on a thin film, small whole organisms such as viruses or bacteria, and frozen solutions.
- Analysing the composition and some bonding differences (through contrast and by using spectroscopy techniques: microanalysis and electron energy loss).
- Acquiring electron diffraction patterns (using the physics of Bragg Diffraction).
- Perform electron energy loss spectroscopy of the beam passing through a sample to determine sample composition or the bonding states of atoms in the sample [157].

However, it also has some limitations:

- TEM cannot take colour images so it could not be used for staining procedures.
- TEM cannot image through thick samples: the usual sample thickness is around 100-200 nm because electrons cannot readily penetrate sections thicker than 200 nm.

- A standard TEM cannot image surface information.
- The TEM cannot reliably image charged molecules that are mobile in a matrix. For example, some species (e.g. $Na^+$) are volatile under the electron beam because the negative electron beam exerts a force on charged material.
- It is a laborious and expensive technique to be established as routine analysis [158].

High Resolution Transmission Electron Microscope (HR-TEM) is an image mode used to study nanomaterial properties and structure at atomic scale and create crystallographic structure images [159]. It is also used on the study of coatings and the protein corona surrounding the nanoparticle in commercial and biological samples [160].

TEM analysis in biological samples such as cell cultures or tissue samples enables the assessment of nanoparticle incorporation into the tissues and allows to follow the fate inside the cells. Conditions must be modified to work with these biological matrixes in order to avoid the excessive damage that the electron beam can cause on the sample (accelerating voltage must be reduced to 100 keV). Moreover, a pre-treatment of the samples is required based on fixation, dehydration and staining processes [161].

**SEM** uses a focused beam of high-energy electrons to generate a variety of signals at the surface of solid specimens that derive from electron-sample interactions and reveal information about the sample including external morphology (texture), chemical composition, and crystalline structure and orientation of materials making up the sample. In most applications, data are collected over a selected area of the surface of the sample, and a 2-dimensional image is generated that displays spatial variations in these properties. Accelerated electrons in a SEM carry significant amounts of kinetic energy, and this energy is dissipated as a variety of signals produced by electron-sample interactions when the incident electrons are decelerated in the solid sample. These signals include secondary electrons (most valuable for showing morphology and topography on samples), backscattered electrons (most valuable for illustrating contrasts in composition in multiphase samples), diffracted backscattered electrons (used to determine crystal structures and orientations of minerals and most valuable for illustrating contrasts in composition in multiphase samples), photons (characteristic X-rays that are used for elemental analysis and continuum X-rays), visible light (cathodoluminescence–CL), and heat [162].

However, it is not possible to:

- Image through water.

- Reliably image charged molecules that are mobile in a matrix.
- Quantify surface roughness at small scale. Atomic Force Microscope (Scanning Probe Microscopy) is more useful for this task.
- Do directly measurements that involve height (z-axis). This requires two images that have been tilted relative to one another to create a 3D image, and specialised processing software.
- Use for experiments involving liquids, chemical reactions, and air-gas systems although some specialised machines and sample chambers do allow for these experiments.
- Achieve high enough resolution to image individual atoms (it is better to use a transmission electron microscope).
- Carry out elemental analysis below micron scale (although it would be possible to get elemental information on the sub-micron scale working below 7keV) [163].

Main characteristics of the two techniques are summarized and collected in Table 9 according to publication of Eaton et al. [164]:

**Table 9. Main aspects of Electron microscopy techniques.**

| Technique | Resolution | Physical basis | Environment | Parameters measured |
|---|---|---|---|---|
| **TEM** | 0.1 nm | Scattering of electrons | Vacuum | Size and shape |
| **SEM** | 1 nm | Emission of electrons | Vacuum | Size and shape |

In Figure 8, examples of 15 nm-gold nanoparticles (6A) and 50 nm-silica nanoparticles (6B) images taken from AFM, TEM, and SEM can be observed according to the previous cited paper [164].

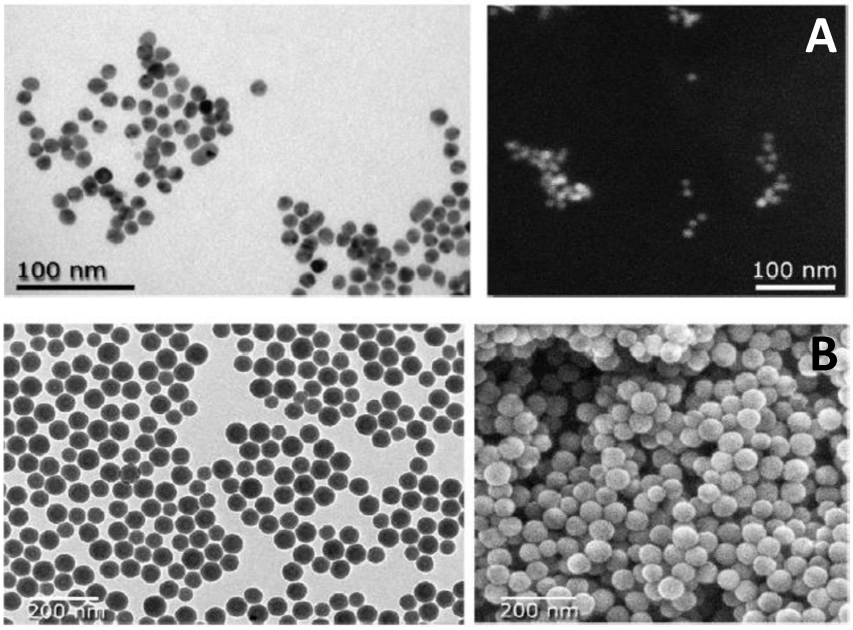


***Figure 8. Examples of 15 nm-AuNPs (A) and 50 nm-silica NPs (B) images taken from TEM (on the left), and SEM (on the right). [164]***

#### *1.4.1.3. Dynamic light scattering*

Dynamic Light Scattering (DLS) is one of the fastest and most often used techniques to determine the particle size and study the diffusion behaviour of macromolecules in solution [165]. It is also known as photon correlation spectroscopy or quasi-elastic light scattering and it primarily measures the Brownian motion of nanoparticles in solution that arises due to bombardment from solvent molecules and relates this motion to the size of particles. Such motion of nanoparticles depends on their size, temperature, and solvent viscosity. Therefore, knowledge of accurate temperature is essential for DLS measurements, since the viscosity of solvent depends on this parameter. When the movement of particles over a time range is monitored, information on the size of nanoparticles can be obtained. Large particles diffuse slowly compared to small particles (such as solvent molecules) which move faster and therefore do not adopt a specific position [166]. Particle size is calculated in terms of hydrodynamic volume, so not only the metallic core is included, but also the surface structure.

This technique has been applied for the determination of mean size of particles, size distribution and polydispersity index of silver, gold or iron oxide nanoparticles [167–169], and it is often used to monitor hydrodynamic size variations during a synthesis procedure [170] or as

detector coupled to other separation techniques such as Field Flow Fractionation, liquid chromatography or capillary electrophoresis [171–173].

One of the major advantages is that the sample can be measured in solution and thus, in conditions closer to original state, which means without altering the structure. DLS also provides information about nanoparticles stability in solution with time [174].

Although DLS is a highly powerful technique, it suffers some limitations such as:

- High sensitivity to temperature and solvent viscosity. Therefore, the temperature must be kept constant and solvent viscosity must be known for a reliable DLS experiment. This implies that samples must be thermodynamically stable during measurements.
- It is a low-resolution method that often cannot separate molecules that are closely related (e.g., monomer and dimer).
- Particles must have a different refractive index from the matrix or solvent.
- Concentration must be high enough but DLS is also restricted to transparent solution preparation, so a compromise must be reached in order to get reliable results.
- Large aggregates, even a very small amount, can affect the measurements. Therefore, the sample-holding cuvette must be cleaned thoroughly, and sample must be filtered prior to DLS measurements [166].

Scattering intensity depends on the sixth power of the hydrodynamic diameter of the particle and thus, signal decreases significantly when particle size also decreases. Therefore, it is also difficult to determine accurate size distributions by DLS in highly polydisperse nanoparticle samples.

Multiangle light scattering (MALS) is a scattering variant technique which measures the light scattered by a sample into a plurality of angles. It is used for determining both the absolute molar mass and the average size of molecules in solution. Collimated light from a laser source is most often used, in which case, the technique can be referred to as multiangle laser light scattering (MALLS). The "multiangle" term refers to the detection of scattered light at different discrete angles as measured, for example, by a single detector moved over a range that includes the particular angles selected or an array of detectors fixed at specific angular locations. It requires cleaner or more diluted samples than DLS to detect particle size. MALS is frequently used as a detector in separation techniques to monitor eluting colloidal and nanoparticle fractions [175–178].

#### *1.4.1.4. X-ray diffraction*

X-ray diffraction (XRD) is a non-destructive tool for the investigation of the matter structure. X-rays are photons whose energies range from 100 eV to 100 keV (wavelength from 0.01 to 10 nm). Photons with energies above/below 5–10 keV (below/above 0.2–0.1 nm wavelength) are called hard/soft X-rays, respectively. X-rays are scattered by interaction with the electrons of the atoms in the material investigated, providing information of the atomic structure and chemical bonds within the nanoparticles. Basically, the X-ray beam impacts the sample forming an angle, Θ, to subsequently, generate diffraction X-rays collected at angles 2Θ [179].

This technique uses X-rays to examine and quantify the crystalline nature of materials by measuring the diffraction of X-rays from the planes of atoms within the material and is sensitive to both the type and relative position of atoms in the material as well as the length scale over which the crystalline order persists. Thus, it can be used to:

- Measure the crystalline content of materials.
- Identify the crystalline phases present (including the quantification of mixtures in favourable cases).
- Determine the spacing between lattice planes and the length scales over which they persist.
- Study preferential ordering and epitaxial growth of crystallites.

Essentially, it probes length scales from approximately sub-angstroms to a few nanometres and is sensitive to ordering over tens of nanometres [180–182].

**Small-angle X-ray scattering** (**SAXS**) belongs to X-ray techniques and allows the quantification of nanoscale density differences in a sample. Therefore, it can determine nanoparticle size distributions, resolve the size and shape of (monodisperse) macromolecules, determine pore sizes and characteristic distances of partially ordered materials by analysing the elastic scattering behaviour of X-rays when travelling through the material, and recording their scattering at small angles (typically 0.1 - 10°). The major problem that must be overcome in SAXS instrumentation is the separation of the weak scattered intensity from the strong main beam. The smaller the desired angle, the more difficult this becomes. However, it enables the characterization of a wide variety of samples including solid or liquid, crystalline or amorphous materials, colloids of all types, metals, cement, oil, polymers, plastics, proteins, foods and pharmaceuticals [183, 184].

Small and **wide-angle diffraction** and **scattering** are often used as synonymous (SAXD and SAXS working at the nanoscale; WAXD and **WAXS** working at the atomic scale) [179]. Only the distance from sample to the detector is shorter in WAXS and thus, diffraction maxima at larger angles are observed. Depending on the measurement instrument used it is possible to do WAXS and SAXS in a single run (SWAXS).

**Energy-dispersive X-ray spectroscopy** (EDS, EDX, EDXS or XEDS), sometimes called energy dispersive X-ray analysis (EDXA) or energy dispersive X-ray microanalysis (EDXMA) provides information about the elemental composition or chemical characterization of a sample. Its use is frequently associated to electronic microscopy instruments (TEM or SEM) for the analysis of metallic and metal oxides nanoparticles composition [185, 186]. Due to this coupling, determination of elemental composition in liquid samples, assessment of nanocrystals growing, or the assurance of crystals purity are possible. Application of EDX as a technique for qualitative and quantitative analyses has been found in the analysis of a great variety of materials (macro to nano scale) in organic and inorganic syntheses, in the metallurgical, environmental or pharmaceutical fields. However, the overlapping over spectral peaks and its inability to determine light elements with atomic number lower than oxygen are few of the drawbacks associated with the techniques. Hopefully, limitations could be overcome with further innovative and engineering research [187, 188].

### 1.4.2. Hyphenated techniques

Hyphenated techniques combine chromatographic and spectral methods of detection to exploit the advantages of both. Chromatography produces pure or nearly pure fractions of chemical components in a mixture; spectroscopy produces selective information for identification using standards or library spectra [189]. Hirschfeld introduced the term ‘‘*hyphenation*’’ to refer to the on-line combination of a separation technique and one or more spectroscopic detection techniques [190].

In the case of nanoparticles, where there is a strong need of separation from other constituents (coming from synthesis or partial degradation) and among different size particles, hyphenated techniques are attractive and competitive strategies that must be optimized to get the best results.

#### 1.4.2.1. Chromatographic and electrophoretic methods

**High-performance liquid chromatography** (HPLC) is considered as one of the most exploited technique for metallic nanoparticles determination and separation. In fact, it has demonstrated to enable the separation among particles of different sizes and even among the metallic ions coming from the degradation of nanoparticles themselves.

In this sense, ICP-MS is the most competitive detection mode and size exclusion, hydrodynamic, reversed phase, and ion exchange chromatography are the most widely used hyphenations in nanoparticles applications.

In **size exclusion chromatography (SEC)**, separation of NPs is based on the entrapment of the species in a porous stationary phase as they pass through the column carried by the mobile phase flow. Residence time depends on the size and shape of the particles, so the bigger the particles, the shorter the time they keep retained in the column. Particles with significantly smaller diameters than the pore size can penetrate deeply and thus, be trapped in the column during longer times. In the case of medium size particles, they can be trapped in the column to a lesser or greater extent depending on their specific size and consequently, fractionation is achieved.

It is important to avoid or minimize possible chemical interactions between analyte and the stationary phase to guarantee that a combined separation mechanism does not take place and thus, efficacy of the column is not compromised. This theoretical lack of interaction with analytes and short analysis times makes this technique very attractive to evaluate nanoparticles size [191–193], shape [194], stability or progression during synthesis process [195, 196], incubations or reactions in different media.

The main limitation when analysing some specific nanoparticles (gold, silver) is the high surface activity they show. Therefore, they not only interact with stationary phase, but also are irreversibly adsorbed by the column. In order to overcome this drawback, different stabilizers, commonly used during the synthesis of nanoparticles (e.g. sodium citrate, tannic acid, sodium chloride or surfactants) have been added to the mobile phase [191, 197]. Some of them proved to prevent from agglomeration and surfactants as SDS has been seen as efficient additive that prevents nanoparticles from adsorption on the column, enabling the elution and separation of gold nanoparticles [197, 198].

There are several studies where SEC is coupled to ICP-MS satisfactorily. One recent example is reported by Jiménez-Lamana et al. and shows the detection of silver ions released from

nanoparticles oxidation in biological media. Moreover, separation of different silver species associated to proteins in the range of 70-25 kDa was achieved [199].

**Hydrodynamic chromatography (HDC)** is a solution-phase liquid chromatographic separation method in which the dissolved sample is injected into an open tube, a column packed with solid beads, or a column packed with porous beads of pore size substantially smaller than the size of the analytes in solution. In packed-column HDC, the beads should be inert so the non-HDC enthalpic interactions between the beads and the dissolved analytes are minimized. Separation in HDC arises from the parabolic or Poiseuille-like flow profile that develops, under laminar flow conditions, in an open tube or in the interstitial medium of a packed column, where the fastest streamlines of flow are in the middle of the tube (or the interstitial medium) and the slowest are near the walls (or the packing particles). The larger analyte remains near the centre of the tube, preferentially experiencing the faster streamlines, whereas the smaller analyte experiences a slower average velocity through the tube because of its ability to sample slower streamlines near the tube walls. Thus, elution order in HDC is the same as in SEC: the larger analytes elute ahead of the smaller ones in both cases. However, the mechanisms of retention of these two techniques are different: in SEC, retention is due to preferential sampling of pore volume, whereas in HDC, it is due to preferential sampling of the streamlines of flow (or to a preferential distribution of analyte between fluid mechanical phases) [200].

HDC has become a powerful technique for characterizing NPs due to separation relies solely on size and does not depend on the coating or the surface charge of the particle. Tiede et al.[201] published an application of HDC coupled to ICP-MS for separating a mixture of $TiO_2$, $SiO_2$, $Al_2O_3$, and $Fe_2O_3$ NPs in sewage sludge, showing this method as versatile and suitable for the separation from ionic/molecular background signals, simultaneous sizing, and quantification in a short time frame. However, HDC-ICPMS has a detection limit in the $\mu g \cdot L^{-1}$ range and does not provide information on the structure or the mass of the particles as it measures only the effective diameter. Thus, combinations of sp-ICPMS and HDC (HDC-sp-ICPMS) are being used more frequently to determine the size, number concentration, and mass fraction of metallic NPs [202] and give information about agglomerates of mixing particles [203].

**Reversed phase chromatography (RP-HPLC)** is also reported as an alternative for the separation of metallic nanoparticles. The most popular column is an octadecyl carbon chain (C18) with large size of particle and small pores in its packing (1000 Å). This added to the functionalization of the stationary phase with SDS to avoid adsorption between nanoparticles and

the column, makes possible the elution of the particles from the column without undesirable interactions. In other words, a mechanism similar to size exclusion is achieved.

It has been applied by Helfrich et al. for the separation of gold nanoparticles coupled to ICP-MS detection [192, 193]. A C18 column with 7 µm of particle size and 1000 Å of pore size was used. Irreversible adsorption of metallic nanoparticles to the stationary phase by the forming bonds with silanol groups of the column is solved by SDS addition to the mobile phase. At the same time, a modification of the stationary phase is produced by changing the chemistry nature of the surface and thus, enabling the elution of nanoparticles. As it has been described, nanoparticles fractionation depends on their size, hydrodynamic volume and shape. As it occurs in SEC, the smaller the particle, the more probability to keep entrapped in stationary phase pores and elute from the column at longer retention times. However, larger particles are retained in the column due to adsorption mechanisms or pore clogging [204].

**Ion Exchange chromatography (IC)** is based on the separation of ions and polar molecules depending on their affinity to the ion exchanger (stationary phase). The water soluble and charged molecules bind to oppositely charged stationary phase by forming covalent bonds. It has been applied for separation of silver ions and nanoparticles in the range of 1-100 nm in food supplements and water samples [205, 206].

In this sense, Hanley et al. proposed a method based on the use of a carboxylic acid functionalization of the column and $HNO_3$ and ethanolamine 0.1 % (w/v) as mobile phase for the separation of silver nanoparticles and ions. Quantification was achieved in a concentration range between 40 µg $kg^{-1}$ and 50 mg $kg^{-1}$ and recoveries of 90 % are obtained for 10 nm AgNPs and $Ag^+$, and 33 % for 100 nm AgNPs. It is proved to be rapid and valid for discrimination between nanoparticles and ionic species, although differentiation among different size nanoparticles is not possible as they all elute at the death volume of the column [205].

Although IC is a competitive tool for preparative and analytical chromatography, one of the main disadvantages is its buffer requirement. Ion exchange columns must be loaded in low-salt buffers because binding to media is dependent on electrostatic interactions between analytes of interest and the stationary phase. For some applications, this restriction may require a buffer exchange step prior to analysis. Another limitation of weak ion exchangers is their pH dependence. When working outside of their optimal pH range, these resins rapidly lose capacity and resolution.

Nanoparticle separation by **electrophoretic methods** is based on the migration of charged species due to the application of an electric field. The most common techniques and highly applied to metallic and metal oxides nanoparticles separation are gel and capillary electrophoresis.

**Gel electrophoresis (GE)** is a separation technique based on differential migration of species according to their size and charge, normally proteins or nucleic acids, in a gel medium placed in an electric field. Different types of nanoparticles could also be separated by gel electrophoresis. Thus, smaller particles experience less resistance from the gel and can move more rapidly [207].

Regarding detection methods, gel electrophoresis separation tends to be coupled to visual detection, optical extinction spectroscopy or TEM. Coupling to ICP-MS needs the use of a laser ablation system, but it was demonstrated by Helfrich et al. that on-line coupling of LC and gel electrophoresis to inductively coupled plasma for a separation by size of gold nanoparticle standards was also possible [192].

In the case of **capillary electrophoresis (CE)**, separation occurs due to the differential mobilities of the species that are injected into hair-thin capillaries filled with an electrolyte, whilst a high voltage is applied to the electrolyte reservoir-dipped capillary ends. In fact, a major breakthrough in the separation of nanoparticles by size has been achieved by application of this technique. The methods developed for nanoparticles offer all the advantages associated with CE, including automation [207].

Detection methods are mainly based on UV-vis spectroscopy due to its simplicity, acceptable results and low cost. However, for the detection of metallic nanoparticles in biological or environmental samples at ultra-trace levels, ICP-MS must be employed.

**Micellar Electrokinetic Chromatography (MEKC)** is a CE mode more suitable for the separation of metallic nanoparticles by size. It is based on the addition to the buffer solution of a micellar "*pseudo-stationary*" phase, which interacts with the analytes according to partitioning mechanisms, just like in a chromatographic method. The "*pseudo-stationary*" phase is composed of a surfactant added to the buffer solution in a concentration above its critical micellar concentration (CMC). The most commonly surfactant used is sodium dodecyl sulphate (SDS), an anionic surfactant that adheres to the surface of the particles and determines the particle size Vs. charge and consequently, achieves the migration [208, 209].

Main advantages of CE are the high resolution, short measurements time and the possibility of analysing both nanoparticles and metallic ions. However, it must be remarked that nanoparticles mobility depends on surface charge and this can be modified when a surfactant is

irregularly adsorbed, or the protein corona is formed. Moreover, analytical standards and reference materials are not generally available for nanoparticles now. Thus, development of precise quantitative methods for the analysis of nanoparticles in real samples is still challenging. Reference techniques such as electron microscopy, could initially facilitate validation of the electrophoretic protocols developed in future [207].

#### *1.4.2.2. Field flow fractionation techniques coupled to ICP-MS*

Field-flow fractionation, commonly designated as FFF, is a flow-based fractionation method, invented and theoretically described by John Calvin Giddings in 1966 for the separation of colloids, particulate material and macromolecules between 1-100 µm of diameter [210]. Fractionation takes place within a trapezoidal channel without a stationary phase. Therefore, FFF does not belong to the class of chromatographic separation techniques. The separation channel is continuously filled with a carrier, developing a parabolic flow profile. The velocity of the carrier-flow stream varies as a function of distance from the channel walls (with the lowest velocity close to the channel walls). Depending on the diffusion coefficient of the sample, fractions expand into different channel heights. A perpendicular field of adjustable strength is applied contrary to the sample diffusion. Upon the establishment of equilibrium, the different sample fractions move in different channel heights and interact with different flow-profile velocities, thus separation and/or fractionation is achieved. Fractions containing constituents with a small diameter and/or molar weight elute before larger ones (normal mode) [211]. The basis of the separation is represented in Figure 9.

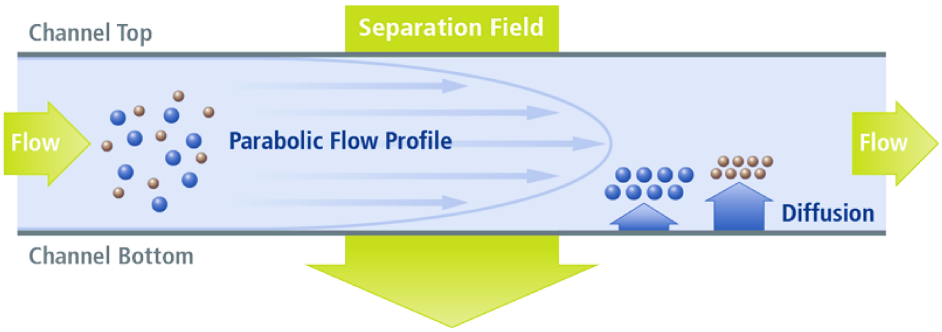


***Figure 9. Separation principle in FFF (source: www.postnova.com).***

Depending mainly on the type of perpendicular field applied, several FFF sub-categories are defined. The most applied technique is the AF4, where the separation is achieved by a liquid cross-flow which takes place in a narrow, ribbon-like channel of trapezoidal geometry, which is built up by a spacer, between a porous and a nonporous plate. During the transport of the analyte by the

eluent, the application of the cross-flow results in a force, dragging the particles/macromolecules to the surface of the membrane [212, 213].

At first, FFF was mostly coupled to UV–visible detection and mainly used in biomolecule research [214]. The introduction of multi-angle light scattering detectors in the 1990s promoted the appearance of several applications in polymer research, enabling fractionation and molar-mass determination [215]. However, neither UV–visible nor light-scattering detection was selective and sensitive enough to answer questions regarding the interaction of natural aquatic colloids and trace metals. Few years later, ICP-MS emerged as the ideal detector providing high sensitivity, elemental selectivity, a species and/or fraction-unspecific response, enabling quantification [211, 216], and isotope information enabling the use of isotopically enriched tracers and isotope dilution.

Published studies show FFF-ICP-MS as a powerful, applicable tool for nanoparticle analysis. However, some challenges have been identified, especially regarding sample preparation and studies conducted in real matrices. Hence, further basic investigations concerning nanoparticle stability and its interaction with the fractionation system are necessary [217]. Additional basic studies on membrane-NPs interactions are also highly necessary [218]. Once more, a crucial point not yet addressed is the need for stable, certified nano reference materials, certified in size and fraction-related quantity for method calibration and validation. However, institutions (NIST, IRRM, and BAM) are working on this requirement and will probably overcome existing challenges in the near future.

## 1.5. Isotope dilution analysis

During this work, IDA has been conducted for the quantification of iron in serum and cell samples for the speciation of nanoparticles and ionic species. The basic principle of this analytical method is graphically described in Figure 10 by a diagram adapted from Alonso and González [219]. Basically, the addition of a known amount of an internal standard (*black spheres*) to a sample containing an unknown (n) number of an analyte (*blue spheres*) changes the concentration of the analyte. By determining the ratio of internal standard to unknown analyte in the resulting mixture, it is possible to back-calculate the amount of the analyte present in the sample. At the bottom of the figure the example of iron isotopes is shown. A spike solution whose isotope ratio and concentration are known, is added to a sample with an unknown concentration of the natural

element (iron in this case). Isotope ratio of the mixture is detected and hence, the origin concentration of the original sample can be calculated.

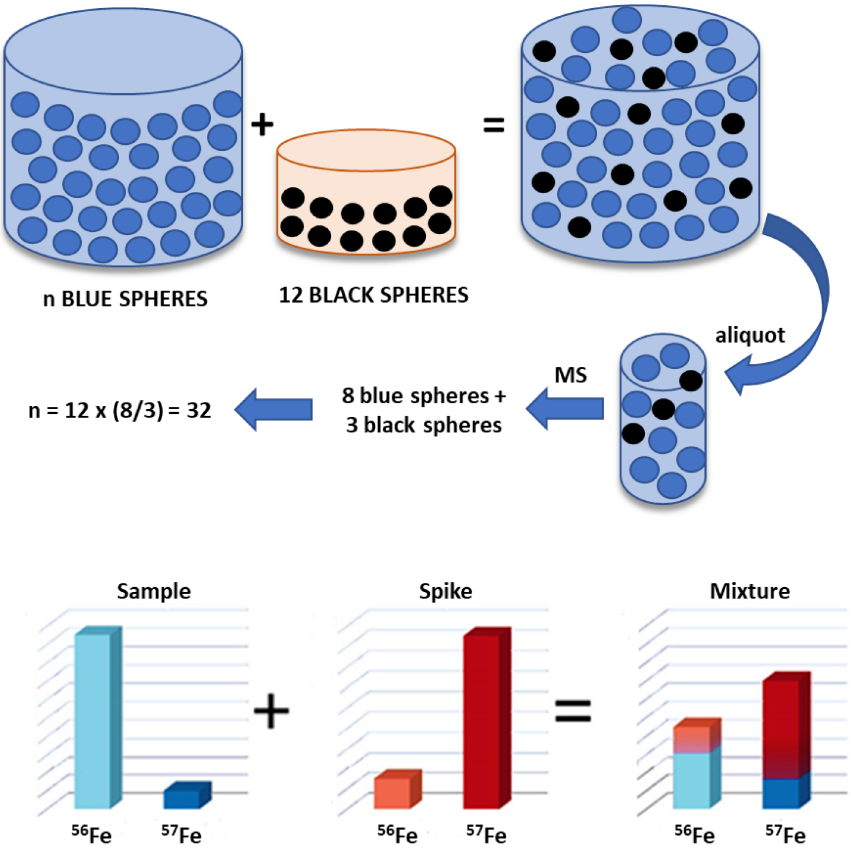


***Figure 10.The principle of isotope dilution and the example of iron.***

A general prerequisite to apply IDA is that the analyte contains at least two natural (stable) isotopes to be detected free from interfering species. However, IDA can also be used for mono-isotopic elements if a radioactive isotope with a long half-life is available.

The main advantage of this method is that the matrix affects all the isotopes of an element at the same level. Therefore, the isotope ratio remains constant. In comparison to other quantification methods, such as the external calibration or standard additions, all matrix effects are compensated by IDA and thus, it is also known as the ideal internal standard method.

There are two different ways for adding the spike that can be conducted by HPLC-ICP-MS: *species-specific mode*, by adding the spike pre-column in the same chemical form as the analyte in the sample. After mixing, an extraction or separation step is needed, followed by the consequently ionization and detection in the ICP-MS. The advantage of this mode is that all sample losses are compensated during the separation because only isotope ratios are used and so are

independent from corresponding intensities. However, this variant has some limited applications, e.g. complex biomolecules as peptides or proteins are not available for this quantification methodology, as they require more laborious and difficult preparation of the isotopically enriched homologues.

The second mode is called *species-unspecific* or *post-column*, and here the spike can be added in any available chemical form, even different from the analyte form. In general, it is introduced at the exit of the column (post-column), once the chromatographic separation has taken place. In this case, analyte losses during the sample preparation and separation are not compensated. Here, it is crucial that the mass flow of the spike is well characterized in terms of concentration and amount of solvent delivered from the pump. Moreover, the spike solution must be pumped continuously and mixed with the mobile phase coming from the chromatographic column.

The concentration of the spike can be determined by the reversed IDA method: a known amount of the element with natural isotopic abundances is added to the spike solution. The concentration of the spike is then calculated according to equation 1:

$$C_{spike} = C_{sample} * \frac{m_{sample}}{m_{spike}} * \frac{M_{spike}}{M_{nat}} * \frac{A^a_{nat}}{A^b_{spike}} * \frac{1 - R_m * R_{nat}}{R_m - R_{spike}} \qquad \text{(Eq. 1)}$$

where:

$C_{spike} = Concentration\ of\ the\ spike$

$C_{sample} = Concentration\ of\ the\ sample$

$m_{sample} = Sample\ added\ to\ the\ sample$

$m_{spike} = Spike\ added\ to\ the\ sample$

$M_{spike} = Atomic\ mass\ of\ the\ spike$

$M_{nat} = Atomic\ mass\ of\ the\ natural\ element$

$A^a_{nat} = Abundance\ of\ the\ most\ abundant\ isotope\ a\ in\ the\ sample$

$A^b_{spike} = Abundance\ of\ the\ enriched\ isotope\ b\ in\ the\ spike$

$R_m = Isotope\ ratio\ (a/b)\ in\ the\ sample$

$R_{nat} = Natural\ isotope\ ratio\ (b/a)$

$R_{spike} = Isotope\ ratio\ (a/b)\ of\ the\ spike$

Once the spike is characterized, the concentration of an element in a given sample can be calculated by equation 2 after mixing it with a known amount of the previous characterized spike:

$$C_{sample} = C_{spike} * \frac{m_{spike}}{m_{sample}} * \frac{M_{nat}}{M_{spike}} * \frac{A^b_{spike}}{A^a_{nat}} * \frac{R_m - R_{spike}}{1 - R_m * R_{nat}} \qquad \text{(Eq. 2)}$$

For species-specific IDA, the spike is added to the sample during sample preparation. After chromatographic separation of the analyte and its co-eluting homologue from interfering species, the detected peak areas of both isotopes were integrated to calculate the isotope ratio of the mixture. Concentration of the analyte can be then calculated by applying equation 2.

For species-unspecific IDA the experimental procedure has to be modified: the inorganic tracer was mixed with the mobile phase at the exit of the chromatographic column as previously described in section *1.2.2.4*. To examine the absolute amount of the injected analyte, the resulting chromatogram must be converted into a so-called mass flow chromatogram and the following equation 3 is applied:

$$Mf_{sample} = C_{spike} * d_{spike} * f_{spike} * \frac{M_{nat}}{M_{spike}} * \frac{A^b_{spike}}{A^a_{nat}} * \frac{R_m - R_{spike}}{1 - R_m * R_{nat}} \qquad \text{(Eq. 3)}$$

where:

$Mf_{sample} = Mass\ flow\ of\ the\ sample$

$d_{spike} = Density\ of\ the\ spike$

$f_{spike} = Flow\ rate\ spike\ pump\ (weight\ per\ time)$

As can be seen in equation 3, the intensities chromatogram can be converted into mass flow (ng $min^{-1}$) chromatogram with the spike information (isotope ratio, flow rate, concentration) and the chromatographic data obtained. By integration of the peaks in the mass flow chromatograms, the absolute amount of the analyte that is presented can be then calculated.

***Isotope pattern deconvolution for the analysis of clinical parameters involved in iron metabolism***

The Isotope pattern deconvolution (IPD) is a mathematical tool which allows the calculation of individual contributions of every isotope of the analyte in the mixture with a different isotope pattern.

In this work, transferrin sialoforms separation by anion exchange chromatography needs the previous saturation with iron of the transferrin. Moreover, when the saturation is produced with natural iron, the transferrin determination by IDA allows the calculation of clinical parameters (TIBC and transferrin total concentration) in human serum samples. Similarly, transferrin saturation can be carried out by a tracer ($^{57}Fe$). In this case, there will be a percentage of natural

iron (the one containing originally in the serum) and a percentage of enriched isotopic iron (the one which is added for the complete saturation).

IPD application to the obtained data from IDA (monitoring $^{56}Fe$ and $^{57}Fe$ isotopes) in serum samples, allows the determination of the naturally present iron level (endogenous iron) and the incorporated iron level (exogenous iron) in each sialoform from the transferrin.

The procedure consists on the addition of a known amount of the spike ($^{57}Fe$) to the sample (serum) containing natural iron. There will be two iron isotopic profiles in the mixture (natural and spike abundances). The iron total amount in the sample can be splitted in two contributions:

$$N_{sample}^{Fe} = N_{nat}^{Fe} + N_{spike}^{Fe} \qquad \text{(Eq. 4)}$$

where:

$N_{sample}^{Fe} = total\ iron\ (mol)\ found\ in\ the\ sample$

$N_{nat}^{Fe} = natural\ iron\ present\ in\ the\ sample\ (endogenous\ form)$

$N_{spike}^{Fe} = iron\ from\ the\ tracer\ that\ is\ present\ in\ the\ sample\ after\ spike\ addition$

It is possible to obtain an individual mass balance for both iron isotopes (56 and 57) as it is shown in the following equations:

$$N_{sample}^{56} = N_{nat}^{56} + N_{spike}^{56} \qquad \text{(Eq. 5)}$$

$$N_{sample}^{57} = N_{nat}^{57} + N_{spike}^{57} \qquad \text{(Eq. 6)}$$

Both equations can be expressed as a linear combination of total amount (mol of iron) and original isotopic abundance of the natural iron and the spike present in the sample:

$$N_{sample}^{Fe} A_{sample}^{56} = N_{nat}^{Fe} A_{nat}^{56} + N_{spike}^{Fe} A_{spike}^{56} \qquad \text{(Eq. 7)}$$

where:

$$A_{sample}^{56} = Isotopic\ abundance\ of\ ^{56}Fe\ in\ the\ sample$$

$$A_{nat}^{56} = Natural\ isotopic\ abundance\ of\ ^{56}Fe$$

When equation 7 is divided by equation 4, the next expression is obtained:

$$A_{sample}^{56} = x_{nat} A_{nat}^{56} + x_{spike} A_{spike}^{56} \qquad \text{(Eq. 8)}$$

where:

$$x_{nat} = \frac{N_{nat}^{Fe}}{N_{nat}^{Fe}+N_{spike}^{Fe}} \qquad \text{(Eq. 9)}$$

$$x_{spike} = \frac{N_{spike}^{Fe}}{N_{nat}^{Fe}+N_{spike}^{Fe}} \qquad \text{(Eq. 10)}$$

being:

$$x_{nat} = iron\ molar\ fraction\ in\ the\ mixture\ (natural\ iron, endogenous\ fraction)$$

$$x_{spike} = iron\ molar\ fraction\ in\ the\ mixture\ (spike, exogenous\ fraction)$$

Similar to equation 8, referred to $^{56}$Fe isotope, equations for the rest of iron isotopes can be obtained and expressed in matrix notation as follows:

$$\begin{pmatrix} A_{sample}^{56} \\ A_{sample}^{57} \end{pmatrix} = \begin{pmatrix} A_{nat}^{56} & A_{spike}^{56} \\ A_{nat}^{57} & A_{spike}^{57} \end{pmatrix} \begin{pmatrix} x_{nat} \\ x_{spike} \end{pmatrix} \qquad \text{(Eq. 11)}$$

The matrix from the left refers to experimental isotopic abundances obtained for $^{56}$Fe and $^{57}$Fe in each chromatographic peak and are derived from isotopes intensities and the following equations:

$$A_{sample}^{56} = 1 - \left(\frac{R_m}{1+R_m}\right) \qquad \text{(Eq. 12)}$$

$$A_{sample}^{57} = \left(\frac{R_m}{1+R_m}\right) \qquad \text{(Eq. 13)}$$

where:

$$R_m = Isotope\ ratio\ 57/56\ in\ each\ chromatogram\ point$$

The second matrix is composed by two columns containing the isotopic abundance of natural iron (left column) and iron in the spike (right column). In this specific case:

$$\begin{matrix} 56 \\ 57 \end{matrix} \begin{pmatrix} 0.91754 & 0.04427 \\ 0.02119 & 0.95055 \end{pmatrix} \qquad \text{(Eq. 14)}$$

The $^{56}$Fe and $^{57}$Fe intensities are related to isotopic abundances of natural iron and spike by the $x_{spike}$ and $x_{nat}$ coefficients. These values are calculated by least squares by using the LINEST function in Excel. Therefore, $x_{spike}$ and $x_{nat}$ express the contribution of exogenous and endogenous iron for each sialoform in the transferrin and from these data, different parameters of clinical interest could be extracted such as:

- Transferrin saturation: $x_{nat}$ or endogenous iron represents the transferrin saturation percentage in each sialoform and considering the contribution of each sialoform, global saturation percentage can be obtained.

- Serum iron: by multiplying the $x_{nat}$ for the TIBC, serum iron in each sialoform can be obtained. The sum of all sialoforms results in the total natural iron present in serum.
- Unsaturated Binding Capacity (UIBC): by multiplying $x_{spike}$ for the TIBC, unbound iron in each sialoform can be obtained and, again, the sum of all sialoforms results in the total unbound iron. This parameter would be also extracted by this expression:

$$UIBC = TIBC - Serum\ iron \qquad \text{(Eq. 15)}$$

# 2 OBJECTIVES

# 2 OBJECTIVES

The overall goal of the thesis was based on the *development of analytical methods based on mass spectrometry to quantitatively study the uptake and biological interactions of metallic nanoparticles with cells and animal tissues*. Considering that, this work was focused on **iron nanoparticles** in particular**,** because of the nature of the iron as an essential element in living organisms and its several applications in biomedical sciences. Moreover, the increasing interest on nanochemistry and the interaction of new nanomaterials within their special properties with biological cells make this goal even more challengeable, trying to clarify if there are harmful effects or establishing metabolic pathways of these nanostructures in human body.

In this framework, the **first objective** was to fully characterize the commercial preparation for intravenous treatment of anaemia, **Venofer®**, in terms of particle size and shape (HR-TEM, DLS, UV-vis) and accomplish quantitative studies on the iron bioavailability from these NPs in serum and blood by using isotope dilution and ICP-MS. The interaction of iron with different proteins in serum samples incubated with the commercial preparation was studied using UV-vis and ICP-MS detection after previous chromatographic separation.

The **second objective** was focused on the searching of a suitable synthesis of non-aggregated iron oxide nanoparticles potentially used as oral supplements for the treatment of anaemia. In this way, a synthesis based on the precipitation of $FeCl_3$ salt in basic medium and the use of sodium tartrate and adipic acid as coating agents was carried out, mimicking the mineral core located inside the ferritin. Resultant iron nanoparticles were characterized using different techniques (HR-TEM, DLS, EDX, UV-vis, SAXS, WAXS). Acid lability studies were conducted to assess nanoparticles stability in simulated gastric conditions.

The **third objective** here proposed was the development of *in vitro* studies concerning the uptake, subcellular location, and toxicity after incubation of different cell lines (THP-1, macrophages, HT-29, and Caco-2) with these self-synthesized FeNPs.

In order to investigate nanoparticles structure and behaviour once they enter the cells, a **fourth objective** based on the speciation and quantification of nanoparticles and ionic species of iron based on a reversed phase high performance liquid chromatography was optimized and applied to Caco-2 cell samples. Quantification approach was tackled by ICP-MS and the application of an online post column isotope dilution analysis with $^{57}Fe$ as isotopically enriched standard.

The **fifth objective** was related to the *in vivo* studies. For this purpose, small intestine perfusion studies were carried out to determine the iron absorption degree in different regions throughout the small intestine, as well as the fate of these FeNPs after intestinal uptake by analysing other tissues involved in iron metabolism such as liver, kidney, spleen, or blood.

# 3 EXPERIMENTAL SECTION

# 3 EXPERIMENTAL SECTION

## 3.1. Reagents and solutions

All working standard solutions were prepared using 18 MΩ $cm^{-1}$ deionized water obtained from a Milli-Q system (Millipore, Bedford, MA, USA).

Venofer® was kindly provided by the Hematology Group of the Hospital Central Universitario de Asturias (Oviedo, Spain) in the form of an aqueous complex of polynuclear iron (III)-hydroxide in sucrose containing 20 mg elemental iron per mL. Upon reception, the content of the vial (5 mL) was separated into aliquots of 1 mL and stored at -4 $^{o}$C until further use. Successive dilutions of the parenteral solution were conducted in 0.9 % sodium chloride NaCl, as stated by the manufacturer.

Serum and blood samples from controls were provided by the Hospital Central of Asturias, Laboratory of Biochemical Analysis (Oviedo, Spain). All blood samples were collected by venous puncture using BD Vacutainer® (Franklin Lakes, NJ, USA) containing gel for serum separation. Samples were anonymous and collected in accordance with protocols approved by the relevant institutional review boards and with the Declaration of Helsinki. Serum was separated by centrifugation (3000 g, 20 min). Samples were then stored in 1 mL aliquots in the fridge until corresponding analysis. In the case of blood samples, they are stored in tubes containing Ethylenediaminetetraacetic acid (EDTA) as anticoagulant agent.

The protein standards used were cyanocobalamin (B12), α-lactalbumin from bovine milk, albumin from human serum, human apo-transferrin and ferritin from equine spleen and were all from Sigma-Aldrich (St. Louis, MO, USA).

All ICP standards (iron 1000 mg $L^{-1}$, germanium 1000 mg $L^{-1}$ from Merck), tuning solutions and elemental tracer were diluted with 0.1 % nitric acid (Panreac). The nitric acid was previously purified using a quartz sub-boiling distillation in a fume hood. Isotopically enriched elemental iron with relative abundances 0.043 % $^{54}$Fe, 4.96 % $^{56}$Fe, 94.52 % $^{57}$Fe, 0.47 % $^{58}$Fe was obtained from Cambridge Isotope Laboratories, Inc. (MA, USA).

The mobile phases for anion exchange separation of serum proteins contained:

- 50 mmol $L^{-1}$ TRIS from Sigma-Aldrich (St. Louis, MO, USA) adjusted to pH 7.4 using acetic acid from Merck (Darmstadt, Germany),
- 50 mmol $L^{-1}$ TRIS at pH 7.4 and 1.5 mol $L^{-1}$ ammonium acetate.

For the separation of transferrin sialoforms the mobile phases contained:

- 25 mmol $L^{-1}$ TRIS from Sigma-Aldrich adjusted to pH 6.5 using acetic acid,
- 25 mmol $L^{-1}$ TRIS at pH 6.5 and 250 mmol $L^{-1}$ ammonium acetate.

Mobile phases were degasified with helium prior to use them.

For cleaning and conditioning the chromatography columns, sodium chloride, sodium hydroxide, EDTA solutions from Sigma, as well as ethanol, acetic acid and acetonitrile from Merck, were employed.

For iron nanoparticles preparation, iron(III)chloride hexahydrate, sodium tartrate, adipic acid, sodium chloride, sodium hydroxide, and ammonium acetate from Sigma were employed.

For the cell culture experiments:

- Minimum Essential Medium (MEM, PAA Laboratories, Yeovil, UK) supplemented with 10 % fetal bovine serum (FBS "Gold", PAA Laboratories), 1 % penicillin/streptomycin and 1 % fungizone (Invitrogen, Paisley, UK) as well as Phosphate Buffer Saline (PBS, PAA Laboratories, Yeovil, UK) were used for Caco-2 and HT-29 cell lines.
- In the case of THP-1 Monocytes and macrophages (grown from THP-1 by PMA addition: 100 µM Phorobol-12-myristat-13-acetate) the culture medium was RPMI supplemented with BSA 10 %, Sodium pyruvate, penicillin/streptomycin and HEPES.

High purity nitric acid (subboiling distilled acid) and hydrogen peroxide 30 % (Merck) were used for acid digestion of biological samples.

Concerning the nanoparticle extraction procedure, a protease inhibitor cocktail (Sigma-Aldrich) and a sucrose solution (Sigma) were used.

The mobile phase for the speciation of iron nanoparticles contained:

- 10 mmol $L^{-1}$ Sodium Dodecyl Sulfate (Sigma) and 10 mmol $L^{-1}$ ammonium acetate at pH 6.8.

In acid lability assays, hydrochloric acid 37 % from Merck was used to set the medium pH.

For the sample preparation for TEM images, tissues had to be previously fixated using glutaraldehyde and formaldehyde in 0.05 M sodium cacodylate buffer, and post-fixed with osmium tetroxide and potassium ferrocyanide in Milli-Q water.

Cell viability assays were conducted using WST-1 kit assay and MTT assay (Roche, Sigma), both for evaluating cell proliferation. Oxidative stress damage was assessed by using a ROS Assay kit (Bioquochem, Spain), based on 2'-7'dichlorofluorescin diacetate (DCFH-DA) reagent. Tert-butyl hydroperoxide (TBHP) was employed as positive control.

For animal intestinal perfusion experiments, a sodium thiopental solution 0.5 % (m/V, Tiobarbital®, BBraun Vetcare, Spain) was used as anaesthetic. Moreover, Tyrode solution was prepared containing 8.0 g $L^{-1}$ NaCl, 0.2 g $L^{-1}$ KCl, 0.2 g $L^{-1}$ $CaCl_2$ anhydrous, 0.1 g $L^{-1}$ $MgCl_2$ anhydrous, 0.05 g $L^{-1}$ $NaH_2PO_4 \cdot H_2O$ and 1 g $L^{-1}$ glucose at pH 7.

Argon, nitrogen, helium and hydrogen gases (99.999% of purity) were supplied by Air Liquide (Madrid, Spain).

## 3.2. Instrumentation

### 3.2.1. Inductively coupled plasma mass spectrometry

Four different ICP-MS instruments have been used throughout this work. The Agilent 7700x, the Agilent 7500 CE and the iCAP TQ ICP-MS and Element XR from Thermo Scientific. The operational parameters which have been applied for analysis are summarized in this section. All instruments have been tuned prior analysis with a tune solution containing several elements with a concentration of 10 ng $g^{-1}$ to calibrate the functional conditions of the mass spectrometer. Here, flow rates between 0.5 to 1 mL $min^{-1}$ have been applied by a peristaltic pump. Subsequently, the torch position, gas flows, lenses and other important instrumental parameters were carefully optimized by analysing a tuning solution containing the elements to be determined to ensure optimal signal to noise ratios for the detection of the analyte.

#### *3.2.1.1. Agilent 7500 CE*

The Agilent 7500 CE (Agilent Technologies, Tokyo, Japan) is equipped with a quadrupole as mass filter. In addition, this mass spectrometric device contains an octapole reaction system (ICP-ORS-MS) which serves as collision/reaction cell using hydrogen or helium as collision gas to remove polyatomic interferences. When it is not used as detector in chromatography, sample is aspirated by a peristaltic pump and nebulized by a concentric nebulizer (Meinhard type). A sample solution mist forms and passes through a double- pass spray chamber where the larger sample droplets are removed by collision with the spray chamber wall. To prevent the spray

chamber from filling up with liquid, the peristaltic pump drain channel constantly removes excess sample solution. The spray chamber is cooled by a thermoelectric device, the Peltier cooler, which enables the temperature inside the chamber to be precisely controlled and stable at 2 °C. Cooling the sample aerosol also removes some of the water from the sample, reducing the level of polyatomic oxide species formed, which in turn reduces the interference on certain analytes. The fine sample aerosol that exits the spray chamber passes directly into the injector tube of the horizontally mounted ICP torch. The ICP torch (Fassel type) is comprised of three concentric quartz tubes through which streams of argon pass. These three gas streams are referred to as the plasma gas, auxiliary gas and nebulizer (carrier) gas. After the analyte ions are formed, they are extracted into the first vacuum stage through a hole in the front plate of the vacuum chamber referred to as the sampling cone. Ions pass through the sampling cone into the interface, which is an expansion region evacuated by a rotary pump. The ions then pass through a second orifice called the skimmer cone, which acts as a differential aperture between the interface and intermediate vacuum stage. Both are made of nickel and have a diameter size of 1 mm and 0.4 mm, respectively.

Between the ion lens assembly and the quadrupole mass filter is located the octapole reaction system. It is an octapole ion guide contained within a stainless-steel vessel and pressurized with a gas, most often He or $H_2$. With the aim of removing the Ar polyatomic interferences that affect the four iron isotopes, $H_2$ was used as reaction gas. The mass analyser is a quadrupole with a following secondary electron multiplier detector that operates in one of two modes (counting and analog) depending on the sample concentrations. In Figure 11 the scheme of the instrument is shown, and main parts are included.

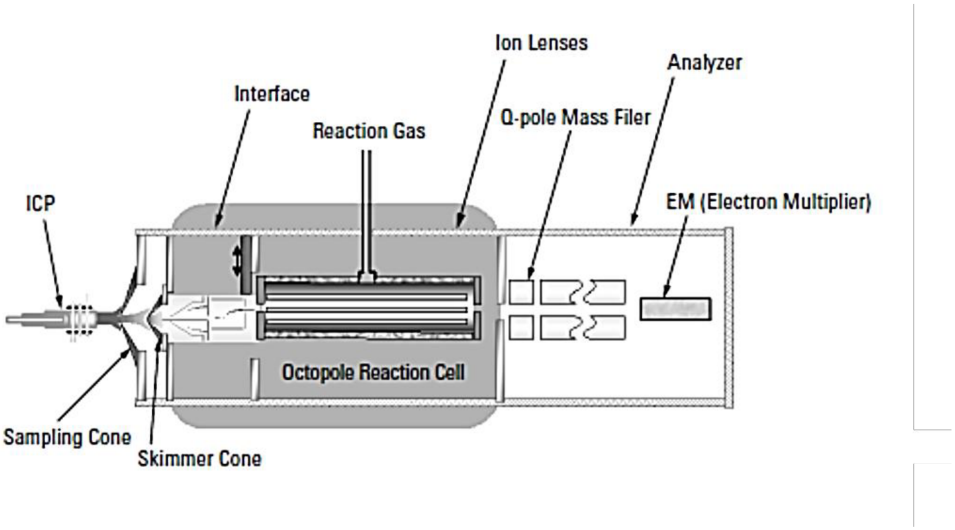


*Figure 11. ICP-ORS-MS Agilent 7500 CE (source: Agilent Technologies Hardware Manual).*

Tune solution containing Li, Co, Y, Tl and Ce 10 ng $g^{-1}$ in 1 % nitric acid was used with and without reaction gas to get the highest sensitivity and check the instrument status.

Important instrument parameters are summarized in Table 10.

**Table 10. ICP-MS parameters used in Agilent 7500 CE.**

| Instrument | Agilent 7500c |
|---|---|
| **RF Power** | 1500 W |
| **Sampling Depth** | 8 mm |
| **Carrier gas flow rate** | 1.15 L $min^{-1}$ |
| **Coolant plasma gas flow rate** | 15 L $min^{-1}$ |
| **Reaction/collision $H_2$ gas flow** | 3.5 mL $min^{-1}$ |
| **Octapole bias** | -18 V |
| **QP bias** | -16 V |
| **Nebulizer** | Meinhard Type |
| **Spray chamber** | Double pass, Peltier cooled (2 °C) |
| **m/z monitored** | 54, 56, 57 |
| **Dwell time** | 0.1 s |

#### *3.2.1.2. Agilent 7700x*

As the above-described instrument, the Agilent 7700x (Agilent Technologies, Tokyo, Japan) also contains a quadrupole as mass filter as well as an octapole reaction system (ICP-ORS-MS) which serves as collision/reaction cell using helium as collision gas to remove polyatomic interferences. The most significant improvements in comparison to the previous model are:

- A new generation of octapole reaction system that includes longer and narrower rods and higher cell pressure and frequency. This allows a more reliable performance in helium mode.
- High Matrix Introduction kit that enables high dissolved solids samples to be run directly with minimal matrix deposition in the interface cones.
- A Shield Torch System that provides effective plasma grounding.

Selected parameters used in the instrument for the bioavailability studies of Venofer® are compiled in Table 11.

**Table 11. Instrument parameters used in Agilent 7700x.**

| Instrument | Agilent 7700x |
|---|---|
| **RF Power** | 1500 W |
| **Carrier gas flow rate** | 0.87 L $min^{-1}$ |
| **Coolant plasma gas flow rate** | 15.5 L $min^{-1}$ |
| **Reaction/collision He gas flow** | 2.5 mL $min^{-1}$ |
| **Octapole bias** | -18 V |
| **QP bias** | -15 V |
| **Nebulizer** | Meinhard type |
| **Spray chamber** | Double pass, Peltier cooled Scott-type (2 $^oC$) |
| **m/z monitored** | 54, 56, 57 |
| **Dwell time** | 0.1 s |

#### *3.2.1.3. iCAP TQ Thermo Scientific*

The iCAP -TQ-ICP-MS from Thermo Scientific (Bremen, Germany) was used for the total iron quantification studies in nanoparticle aqueous suspensions as well as cells and animal tissues samples. It is equipped with a compact, low pulsation, four-channel peristaltic pump with inner rollers to minimize signal disturbances. A Peltier cooled cyclonic spray chamber filters out larger aerosol droplets and improve plasma stability. A push-in, demountable single piece quartz torch is used, and nickel cones consisted on sampler and skimmer of 1.1 mm and 0.5 mm diameter orifice, respectively, are optimized for reduced matrix deposition and maintenance. Moreover, the High Sensitivity Interface provides optimal signal to noise ratio for ultratrace analysis and advanced applications. One of the special features of this instrument is the 90$^o$ cylindrical ion lens at a single fixed voltage that provide high ion transmission across the entire mass range. Mass analyser system is composed by three sequential quadrupoles:

- Q1 Quadrupole: High frequency quadrupole mass analyser with pre and post filter for isolation of analyte ions and filter out unwanted ions.
- Q2 Collision/Reaction Cell (CRC): Pressurized with reactive gas to selectively generate reaction products. Four gas specific mass flow controllers deliver $H_2$, $NH_3$, $O_2$ and He according to the analyte requirements. In this case, different flows of $H_2$ were used and optimized prior analysis.
- Q3 Quadrupole: It isolates ions required for measurement with a manual definable mass resolution.

Ion detection system is based on a dual mode discrete dynode electron multiplier and allows simultaneous counting/analog operating mode. The experimental instrument set up is shown in Figure 12.

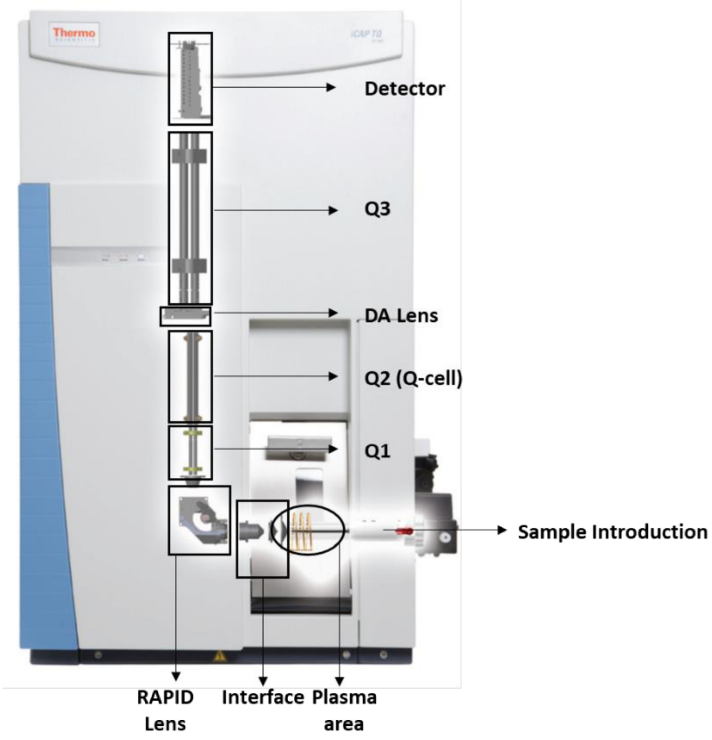


*Figure 12. iCAP-TQ-ICP-MS (source: Thermo Scientific Production Specifications).*

Instrument autotune was daily performed (Interface and Advanced $H_2$ mode) in order to set optimal parameters before the analysis. Final instrument settings are summarized in Table 12.

**Table 12. Instrument parameter set for the analysis in iCAP -TQ-ICP-MS Thermo Scientific.**

| Instrument | iCAP -TQ-ICP-MS Thermo Scientific |
|---|---|
| **RF Power** | 1550 W |
| **Carrier gas flow rate** | 0.80 L $min^{-1}$ |
| **Coolant plasma gas flow rate** | 14 L $min^{-1}$ |
| **Reaction/collision He gas flow** | 7.8 mL $min^{-1}$ |
| **Pole bias** | -11.83 V |
| **CCT bias** | -6.20 V |
| **Nebulizer** | Cyclonic Meinhard type |
| **Nebulizer gas flow** | 1.07 L $min^{-1}$ |
| **Spray chamber** | Double pass, Peltier cooled Scott-type (2 °C) |
| **m/z monitored** | $^{56}Fe$, $^{57}Fe$, $^{72}Ge$, $^{74}Ge$ |

#### *3.2.1.4. Thermo Element XR*

The Thermo Element XR from Thermo Scientific (Bremen, Germany) is a mass spectrometric device based on double-focusing sector field which was used in medium resolution for monitoring iron. The ICP-MS Element XR was synchronized with the laser ablation unit (NWR213 from ESI, *Fremont, USA*) in external triggering mode and daily tuned for maximum ion intensity and good signal stability (RSD > 5 %), keeping the oxide ratio (ThO/Th) below 1% during ablation of a glass slide. Helium was used as carrier gas and argon was added before reaching the ICP torch using a y-piece.

Typical instrumental settings which have been applied are listed in Table 13.

**Table 13. Element XR operating parameters.**

| **Instrument** | **Thermo Element XR** |
|---|---|
| **RF power / W** | 1350 |
| **Guard electrode** | Platinum, active |
| **Ar cooling gas flow rate / L min$^{-1}$** | 16 |
| **Ar auxiliary gas flow rate / L min$^{-1}$** | 1.0 |
| **Ar sample gas flow rate / L min$^{-1}$** | 0.6 |
| **Sample and skimmer cone** | Ni |
| **Mass resolution** | Medium (R = 4000) |
| **Scan optimization** | Speed |
| **Isotopes monitored** | $^{56}$Fe, $^{57}$Fe |
| **Magnet settling time / s** | 0.001 |
| **Runs x pass** | 480 – 880 x 1 (depending on the length of the line) |
| **Detection mode** | Both isotopes with SEM (triple) |
| **Sample time / s** | 0.002 |
| **Samples per peak** | 20 |
| **Segment duration per isotope / s** | 0.012 |
| **Mass window per isotope / %** | 30 |
| **Search window / %** | 60 |
| **Integration window / %** | 30 |
| **Scan type** | E-scan |

### 3.2.2. High performance liquid chromatography

#### *3.2.2.1. HPLC systems*

For chromatographic experiments the following instrumentation was used:

- HPLC system based on high pressure dual-piston pump LC-20AD from Shimadzu Corporation, Kyoto, Japan. Sample injection was conducted with a dual mode injection valve from Rheodyne, model 9125 (Cotati, California, USA), fitted with a 20, 50 and 100 µL PEEK injection loop (Up-church Scientific, Oak Harbor, Washington, USA).
- Chromatographic analysis applying UV-vis detection was accomplished with a conventional Agilent 1100 series quaternary HPLC pump (Agilent, Waldbronn, Germany) that is composed by a vacuum degasser, autosampler, a thermostatted column compartment (TCC) which is a Peltier-based design offering stable operation at ambient, sub-ambient and above-ambient temperatures, and a diode array detector giving outstanding sensitivity over the entire wavelength range (both UV and visible). Its features include deuterium and tungsten lamps that ensure the highest light output, from 190 to 950 nm with a whopping 1024 diodes and a programmable slit to optimize wavelength resolution.
- Agilent 1200 series HPLC pump (Agilent, Waldbronn, Germany) similar to the previous Agilent series described, was used for collecting fractions at the exit of the chromatographic column.

#### *3.2.2.2. Chromatographic columns and related parameters*

The chromatographic columns used for the different separation purposes were summarized in Table 14:

**Table 14. HPLC columns applied.**

| Column | Bed vol. (mL) | Bed size (mm) | Particle size (µm) | Flow rate (mL $min^{-1}$) |
|---|---|---|---|---|
| **Superdex 200 10/300 GL (GE Healthcare)** | 24 | 10 x 300 | 13 | 0.6 |
| **Mono Q 5/50 GL (GE Healthcare)** | 1 | 5 x 50 | 10 | 1 |
| **Nucleosil 1000-7 C18 (Macherey-Nagel)** | 4.15 | 4.6 x 250 | 7 | 0.5 |

For the chromatographic separation of Venofer® via size exclusion mechanism, a Superdex 200 10/300 GL column from GE Healthcare was used. This column has an upper exclusion limit

of 600 kDa. 50 mM ammonium acetate (pH 7.4) was used as mobile phase, applying a flow rate of 0.6 mL·min$^{-1}$ and an injection volume of 100 µL.

For the transferrin saturation, a Mono Q 5/50 GL anion exchange column (strong cation) from GE Healthcare Life Sciences was employed, applying gradient elution detailed in Table 15. Mobile phase A was composed of 25 mM Tris acetic acid (pH 6), and 25 mM Tris acetic acid and 250 mM ammonium acetate (pH 6) was mobile phase B composition. A flow rate of 1 mL min$^{-1}$ and an injection volume of 100 µL were used for these experiments.

**Table 15. Gradient employed for transferrin sialoforms separation.**

| Time (min) | A concentration (%) | B concentration (%) |
|---|---|---|
| **0** | 100 | 0 |
| **45** | 25 | 75 |
| **46** | 0 | 100 |
| **50** | 0 | 100 |
| **51** | 100 | 0 |

In the speciation of serum iron-binding proteins, the same anion exchange column (Mono Q 5/50 GL) was utilised with different conditions. Gradient elution was also used and collected in Table 16. Mobile phase A was composed on 50 mM Tris acetic acid (pH 7.4) while mobile phase B composition was based on the mixture of mobile phase A and 0.75 M ammonium acetate (pH 7.4). A flow rate of 1 mL min$^{-1}$ and an injection volume of 50 µL were employed in this case.

**Table 16. Gradient used for serum proteins separation**

| Time (min) | A concentration (%) | B concentration (%) |
|---|---|---|
| **0** | 100 | 0 |
| **30** | 0 | 100 |
| **31** | 100 | 0 |

For the speciation of nanoparticles and soluble species of iron, a $C_{18}$ reversed-phase column with a pore size of 1000 Å was used (Nucleosil 1000-7 C18, Macherey-Nagel). Mobile phase was composed of 10 mM ammonium acetate modified with 10 mM SDS (pH 6.8). Here, flow rate of 0.5 mL min$^{-1}$ and an injection volume of 20 µL were employed.

### *3.2.2.3. Hyphenation of HPLC to ICP-MS*

Hyphenated online systems for speciation studies are well established in elemental speciation and provide highly reproducible results in much less time than traditional off-line methodologies. Moreover, these hyphenated techniques allow a fast and direct application of on line isotope dilution, improving significantly the metallic speciation accuracy.

HPLC hyphenation to ICP-MS is quite simple due to the compatibility between chromatographic flows (usually around 1 mL $min^{-1}$) and most conventional nebulizers used for ICP-MS. From a technical point of view, it consists on coupling the exit of the column to the nebulizer by using PEEK tubing with reduced inner diameters (approximately 50 and 76 µm, 0.03 and 0.04 in., respectively) and reduced length in order to avoid death volumes and chromatographic peak broadening.

In this work, the following hyphenation procedures were accomplished:

- Size exclusion HPLC-ICP-MS for determination of Venofer® molecular weight.
- Anion exchange HPLC-ICP-MS for the separation of transferrin sialoforms and the on-line iron bounded detection in serum samples.
- Anion exchange HPLC-ICP-MS for the separation and detection of other serum iron-binding proteins.
- Reversed phase HPLC-ICP-MS for the speciation of nanoparticles and ionic species of iron in aqueous solutions and cell samples.

### *3.2.2.4. Experimental set-up for post-column IDA*

To carry out the iron quantification by on-line IDA, the eluent was mixed at the exit of the column at a continuous flow rate of 0.1 mL $min^{-1}$ with the spike solution of $^{57}Fe$ by using an auxiliary peristaltic pump. A T-piece (Upchurch Scientific, Oak Harbor, Washington, USA) was installed after the column to allow the mixing of both solutions and consequently nebulization at the same time in the plasma. In order to establish the exact spike flow rate, a calibration before and after analysis was carried out every measurement day. The $^{57}Fe$ tracer was solubilized first in ultrapure water and then 0.1 % $HNO_3$, reaching the most stability signal in the latter. In Figure 13, a scheme of the experimental set-up is shown.

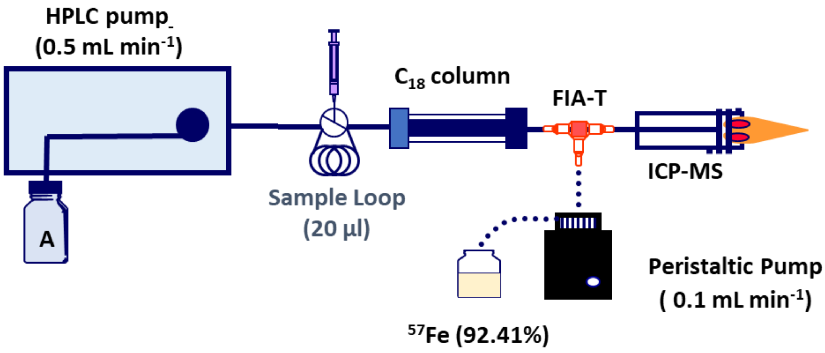


*Figure 13. Experimental set-up for post-column IDA.*

### 3.2.3. Laser ablation system

A NWR213 (ESI, USA) is a high performance Nd:YAG deep UV (213 nm) laser ablation system. This system is equipped with a two-volume ablation chamber was coupled to an ICP sector field mass spectrometer (Element XR, Thermo Fisher Scientific, Bremen, Germany), previously mentioned in *section 3.2.1.4.* Important parameters are collected in Table 17.

**Table 17. NWR213 operating conditions.**

| Instrument | NWR213 Laser Ablation System |
|---|---|
| **Wavelength / nm** | 213 |
| **Laser ablation method** | Line scanning |
| **He carrier gas flow rate/ L min$^{-1}$** | 1.0 |
| **Laser warm up / s** | 10 |
| **Wash out / s** | 25 |
| **Spot size / µm** | 15 |
| **Scan rate / µm s$^{-1}$** | 15 |
| **Repetition rate / Hz** | 10 |
| **Fluence / J cm$^{-2}$** | 0.5 |
| **Line distance / µm** | 12 |

### 3.2.4. Miscellaneous

For the measurement of the absorbance spectra in different iron nanoparticle solutions, a Genesys 10 S UV-Vis from Thermo Fischer Scientific (Wi, USA) was used. A TECAN GENios microplate reader (Tecan, Switzerland) was used for measuring the absorbance in the cell viability assays. Fluorescence of the ROS assays was measured using a microplate reader Infinitive 200 (Tecan, Switzerland). Cell counting was carried out with a CASY® Cell Counter + Analyzer Model TT from Roche Innovatis AG. Lyophilization of animal tissues was achieved by using a LyoLab 3000 freeze-dryer from Heto (Alleød, Denmark). Digestion of animal samples was carried out using a microwave system Ethos 1 from Milestone (Sorisole, Italy). For centrifugation and ultrafiltration, a Heraeus Biofuge Stratos from Kendro (Osterode, Germany) was used. The centrifuge was equipped with a 35° fixed angle rotor.

## 3.3. Data acquisition and treatment

In this work, different types of software have been applied for data treatment. The most relevant ones are here summarized:

- The Agilent 1100 series with UV-vis detection was controlled by HP Chemstation.
- Calculations for IDA-based quantitative analysis was conducted by Excel and OriginPro 8.
- Agilent 7500CE and 7700x ICP-MS were controlled by MassHunter Workstation software.
- iCAP TQ-ICP-MS from Thermo Scientific was controlled by Qtegra™ version 2.8.2944.159.
- Chromatographic data treatment was achieved by Excel in combination with OriginPro 8.
- For the images processing from HR-TEM, ImageJ version 1.43u was used.
- DLS measurements files were processed using Malvern Zetasizer Software 7.11.

## 3.4. Experimental procedures

### 3.4.1. Characterization of iron-sucrose formulations: Venofer®

Commercial preparation, Venofer®, was thoroughly characterized in terms of particle size and by different hyphenated techniques such as SEC-UV-vis and SEC-ICP-MS in order to determine the molecular weight of the complex and evaluate the possible presence of other iron containing species in the suspension. For this purpose, several experiments were carried out:

- HR-TEM measurements were done in a JEOL-JEM 2100F (Tokyo, Japan) transmission electron microscope with TEM operation voltage at 200 kV to image iron NPs suspensions deposited on Cu grids. The instrument permits also to obtain the elemental composition of the sample. Images were then analysed and treated with software ImageJ to obtain particle diameter average and check nanoparticle shape and aggregation.
- Dynamic Light Scattering technique was applied to have an idea of the Polydispersity Index, as well as the hydrodynamic volume of the sample in solution using a Malvern Zetasizer Nano ZS (Malvern Instruments Limited, Worcestershire, UK) with a detection angle of 173°. All measurements were taken at a temperature of 25 ºC. Three replicates on each sample were taken to assess the repeatability of the measurements. The Nano S uses a 4 mW He–Ne laser operating at a wavelength of 633 nm.
- A UV-vis spectrum was also obtained to evaluate the energy band gap of the semiconductor Fe-based nanomaterial. The optical absorbance measurement was carried out at room conditions on a Genesys 10S UV/Vis spectrophotometer (Thermo Scientific, USA).
- Size Exclusion Chromatography coupled to UV-vis and ICP-MS detection were conducted as a way to detect its molecular weight (prior calibration of the chromatographic column with protein standards) as well as to identify the iron in the nanostructure. Chromatographic separation was performed with a Superdex-200 (range of size exclusion: 10-600 kDa, GE Healthcare Bio-Sciences Uppsala, Sweden) using a mobile phase of ammonium acetate (50 mM, pH 7.4). The HPLC system used consisted of a dual piston HPLC pump (Shimazdu LC-20AD, Shimazdu corporation, Kyoto, Japan) and was equipped with a sampler injection valve, Rheodyne, Model 9125 (Cotati, CA, USA) fitted with a 100 µL loop. Chromatograms

were obtained using a diode array detector (model 1100, Agilent Technologies, Waldbron, Germany). ICP-MS experiments were conducted on an Agilent 7700x ICP-MS (Agilent Technologies, Santa Clara, CA).

### 3.4.2. Incubation of serum and blood samples with Venofer®

For this study, pooled serum and whole blood samples from anonymous patients from the Hospital Universitario Central de Asturias (HUCA) have been used. Samples were collected in accordance with protocols approved by the relevant institutional review boards (HUCA) and with the Declaration of Helsinki. For experiments with serum, the samples were taken in 5 mL vacutainer tubes (Greiner Bio-one, Madrid, Spain) for trace elements and the serum was obtained by immediate centrifugation. Serum samples were pooled to obtain a large sample volume and divided into different aliquots of 2 mL (for incubation with Venofer®). In the case of whole blood, the samples were taken in heparin containing tubes to avoid coagulation and, similarly to serum, separated into aliquots for further incubation with Venofer®.

The posology of Venofer® depends on a number of parameters including body weight, haemoglobin level, etc. [220]. To conduct the in vitro experiment, the doses were calculated according with the manufacturer recommendation of 7 mg iron per kg body weight. Assuming an average weight of 70 kg, this corresponds to about 500 mg iron. Since the experiments are conducted in 2 mL of serum and considering that the doses are estimated for 5 L of blood (average value per individual), an adequate dilution of the preparation in 0.9 % NaCl was done to achieve a final concentration of approximately 100 µg iron per mL serum. Then, the serum and whole blood samples were maintained at room temperature (21 ± 2 $^{o}$C) and continuously shaking for 1, 3.5, and 7 hours respectively, since the elimination half-life of Venofer® is about 5–6 hours [221]. Then, the samples were centrifuged and filtered through 0.45 µm to remove the remaining nanoparticulate material and obtain the solubilized iron from the particles.

*Total iron determination in serum and blood samples*

Blood and serum samples were diluted in 0.1 % $HNO_3$ and spiked with isotopically enriched $^{57}Fe$ (Cambridge Isotope Laboratories) of known concentration. By using the isotope dilution calculations (Eq. 2), the concentration of Fe in the samples and the bioavailable Fe by comparing the concentration before and after incubation were obtained. Samples were measured by Agilent 7700x ICP-MS and important parameters are collected in Table 11.

### 3.4.3. Evaluation of the quantitative association of released Fe to transferrin sialoforms

#### *3.4.3.1. Iron Transferrin saturation*

Chromatographic separation of different isomers of Tf (sialoforms) methods are based on their different charge according to their different isoelectric points and therefore, the separation depends on the sialic acids content and the potential iron content.

Thus, a first step before separation of the sialoforms is the complete saturation of Tf with iron, so that every sialoform contains the same amount of the metal. Once the Tf is fully saturated, charge contribution comes exclusively from sialic acids and, therefore, different isoforms (sialoforms) can be separated considering the number of sialic acids [222].

For iron saturation of human serum transferrin, 0.5 mL of the serum sample was diluted (1+1) in 25 mM Tris-acetic acid buffer and then incubated with 25 µL of a 10 mM Fe solution (as $FeCl_3$) and 25 µL of a 500 mM sodium bicarbonate solution, as synergistic anion, for 30 min at room temperature. The samples previously saturated with iron were subsequently filtered through 0.22 µm syringe filters before injecting in the HPLC system (100 µL). The Tf isoforms were separated by means of a linear gradient of ammonium acetate (0-250 mM in 45 min) buffered by 25 mM Tris-acetic acid (pH 6.5) solution.

Previous studies in our research group [140, 223] established the optimum methodology to separate Tf sialoforms with the highest resolution. It is based on an anion exchange chromatography (Mono Q 5/50 GL) using a linear gradient of 250 mM ammonium acetate from 0 to 75 % in 45 min at pH 6, as it was here described.

#### *3.4.3.2. Optimization of Transferrin sialoforms separation*

The main parameter to be optimized in the Tf sialoforms separation is the eluting pH due to proximity between the isoelectric points of every sialoform in the human serum protein. pI of the most abundant sialoform ($S_4$) is 5.4, while the rest of the sialoforms have pI values of 5.9, 5.8 and 5.7 ($S_0$, $S_1$ and $S_2$, respectively). In a lesser abundance are the other sialoforms ($S_3$, $S_5$ and $S_6$) with pIs of 5.6, 5.2 and 5.0, respectively.

### 3.4.4. Iron association to other binding proteins

Relating to the chromatographic separation of the Fe binding serum proteins, a strategy already reported was followed [224]. An HPLC system containing a dual-piston liquid chromatographic pump (Shimadzu LC-20AD, Shimadzu Corporation, Kyoto, Japan) and a sample injection valve from Rheodyne, fitted with a 50 µL injection loop, was used. The used column for the separation was an anion exchange Mono Q 5/50 GL (50 x 5 mm id, Pharmacia, Amersham Bioscience, Sweden). The mobile phase flow was 1 mL $min^{-1}$ and the absorbance of the proteins was monitored at 280 nm using a Diode Array Detector (DAD) detector (model 1100, Agilent Technologies, Waldbronn, Germany). For the ICP-MS detection the Agilent 7700x (Agilent Technologies, Santa Clara, CA) was used.

### 3.4.5. Iron nanoparticles

Several approaches for iron nanoparticles syntheses were tried, all based in the co-precipitation of $FeCl_3$ and $FeCl_2$ or $FeSO_4$ in presence of a coating agent (dextran or sucrose) in aqueous alkaline solution under inert atmosphere (Argon or Nitrogen atmosphere). First, dextran-coated iron nanoparticles were assayed using dextran previously reduced (with $NaBH_4$) [225] or non-reduced dextran [226]. Other approaches were tried for dextran iron oxide nanoparticles synthesis not using inert atmosphere [227], again with reduced and non-reduced dextran. The use of an enriched urea medium for precipitation was also tried in order to achieve more homogenous precipitation [228].

Trying to mimic the starting composition of the commercial preparation (Venofer®) and looking at the best results obtained until that moment in terms of monodispersity and non-aggregation/agglomeration of nanoparticles, a sucrose-coated iron nanoparticles synthesis was carried out following previous reference using dextran [225] properly modified and adapted to the use of sucrose but keeping the stoichiometry from the reported protocol.

For a suitable and reproducible synthesis of non-aggregated iron oxide nanoparticles, a synthesis based on the precipitation of $FeCl_3$ salt in basic medium and the use of sodium tartrate and adipic acid as coating agents was carried out and the resultant iron nanoparticles were characterized using different techniques.

### 3.4.5.1. Synthesis and purification procedure of FeNPs studied

A protocol inspired by previous studies developed by Powell et al. [71] consisting on the precipitation of $Fe^{3+}$ in presence of highly basic medium (5 M NaOH solution) was carried out. For this purpose, an acidic stock solution of iron(III)chloride (27 mM, pH < 2, to ensure the Fe is totally solubilized) was added to a solution containing the ligands (sodium tartrate 100 mM, adipic acid 100 mM, molar ratio established as 1:1:2, Tartrate: Adipate: Fe) previously solubilized in 0.9 % KCl solution, so the ionic strength of the medium can help to control the size and shape of the nanoparticles. All the mixture is stirred continuously at room temperature in the presence of a buffer (ammonium acetate 50 mM pH 4). Then, the initial pH is increased by drop-wise

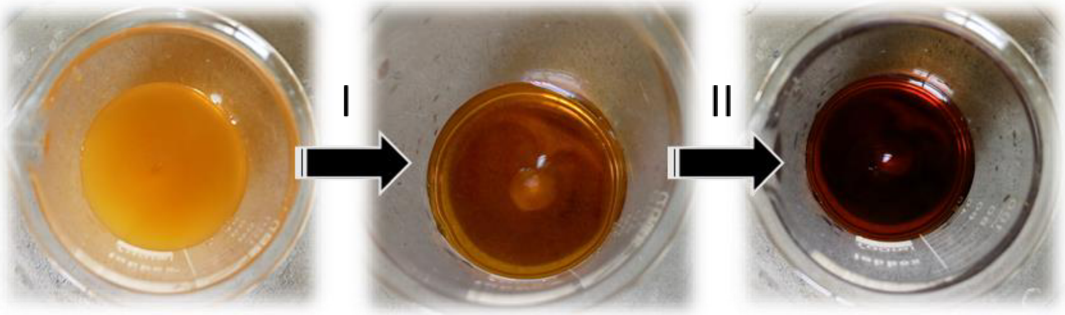


***Figure 14. Synthesis of FeNPs and gradual change in color during the process. I. Addition of ammonium acetate buffer (pH 4.1); II. Dropwise addition of NaOH 5 M and progressive increasing of pH.***

addition of the NaOH solution previously prepared until reaching a final pH value in the range of 8-9. This step is easily followed by the change in colors that takes place during the basic solution incorporation. When the mixture turns dark brown/blackish, synthesis of FeNPs has finished and purification steps are followed to separate the microparticulate and soluble fraction from the nanoparticulate one. In Figure 14 the gradual color change during the whole process is displayed.

Purification procedure is based on centrifugation and ultrafiltration steps. Firstly, suspension is centrifuged (10000 g x 5 min) so, the supernatant is collected and precipitate (if present) containing the bigger iron particles is discarded. Then, the collected brownish suspension is ultrafiltrated (Amicon 3000 Da Ultra-15 MWCO centrifugal filter units, Millipore) at 10000 g during 5 min, and the soluble iron which passes through the filter, is discarded, while the upper part of the filter is washed with milli Q water and collected for further analysis.

#### 3.4.5.1.1. Synthesis of isotopically enriched $^{57}$FeNPs

Once the FeNPs synthetic route was selected, the next goal was focused on the synthesis of isotopically labelled $^{57}$Fe-oxide nanoparticles that allow to trace the Fe release into different

tissues more easily by mass spectrometry. The protocol followed for the FeNPs was slightly modified. As the stable iron isotope $^{57}Fe$ (95.53 %) was purchased in elemental form (Cambridge Isotope Laboratories, Inc., MA, USA), aqueous solutions of the tracer were prepared by dissolving the metal in a mixture of $HCl:H_2O_2$ (8:1) at 60 $^{o}C$, in order to obtain similar Fe(III)chloride precursor to the one used in the original FeNPs synthesis. Then, same steps as described in previous section were followed. Resulting nanoparticles were further characterized using HR-TEM (JEOL JEM-2100F, Tokyo, Japan) and analysed to obtain particle diameter average and check nanoparticle shape and aggregation. Iron content was measured, and nanoparticle and soluble fractions were also quantified by ICP-MS (Agilent 7700x ICPMS, Agilent Technologies, Santa Clara, CA), using $H_2$ as reaction gas to remove polyatomic interferences.

#### *3.4.5.1.2. Synthesis of Holmium-doped FeNPs*

To employ more suitable nanoparticles to be detected in complex matrixes by ICP-MS, an alternative to isotopically enriched $^{57}FeNPs$ was developed. In this case, FeNPs were synthesized following the same protocol as previously detailed but including 1 % of Holmium in the procedure. In brief, calculations were accordingly made so 1 % of the total amount of Fe(III)chloride employed in the original procedure was replaced by 1 % Holmium (Holmium(III)chloride, abcr, Karlsruhe, Germany). Precipitation and purification procedure remained without modifications. Characterization by DLS (Malvern Zetasizer Nano ZS, Malvern Instruments Limited, Worcestershire, UK) and UV-vis absorbance (Genesys 10S UV-vis, Thermo Scientific, USA) was specifically performed.

### *3.4.5.2. Acid lability assays*

As a potential use of these FeNPs on the oral treatment of anaemia, their possible behaviour facing the gastrointestinal barrier is a matter of interest. In this environment, pH range goes from 1.0-2.5 in the stomach to 6.6-7.5 in the proximal end to the ileum of the small intestine [229]. Thus, the stability of the synthesized FeNPs was checked by performing acid lability assays based on the work of Pereira et al. [55]. The freshly prepared FeNPs were suspended in 0.15 M NaCl to an iron concentration of 2 mM and incubated for 95 minutes at room temperature. The pH was set at 3.0 with 1 M NaOH and 1 M HCl. Samples were collected at different times (0, 5, 10, 15, 35, 55 and 95 minutes). To assess the fractionation of the iron into percentages of microparticulate, nanoparticulate, and soluble iron during the process, centrifugation and ultrafiltration steps were applied. NPs suspensions were first centrifuged (10000 g x 5 min) and the sediment (if present) was considered as the microparticulate fraction. In order to isolate the soluble iron and to distinguish it from the nanoparticulate form, the supernatant from the

previous centrifugation was ultrafiltered (10000 g x 10 min, Mr cut off: 3000 Da, Amicon Ultra Centrifugal Filters, EMD Millipore, Darmstadt, Germany). The total iron was determined by ICP-MS and microparticulate, nanoparticulate and soluble fractions were expressed as percentage in relation to total iron content as described elsewhere [55].

### 3.4.6. *In vitro* studies

With the aim of clarifying FeNPs behaviour in cellular media, several experiments were carried out to determine the level of iron uptake, distribution and toxicity in different cell lines such as THP-1 monocytes, macrophages, Caco-2 and HT-29.

#### *3.4.6.1. Cell culture*

THP-1 cells, a pro-monocytic cell line, were cultured in RPMI 1640 (Life Technologies, Grand Island, NY) supplemented with 10 % fetal bovine serum (Gemini Bio-Products, West Sacramento, CA), 10 mM Hepes, 0.1 mM MEM non-essential amino acids, 1 mM sodium pyruvate, and 100 nM penicillin/streptomycin (Life Technologies) and incubated at 37 ºC in an atmosphere of 5 % $CO_2$ and 95 % air at a relative humidity of approximately 95 %. Medium was changed every 2-3 days and, approximately, once a week, cells were centrifuged for splitting and re-suspended in fresh medium at a lower concentration to keep growing.

THP-1 cells were differentiated with 100 µM PMA (phorbol 12-myristate 13-acetate; Sigma-Aldrich, St. Louis, MO) and incubated during 48 h to allow complete differentiation into macrophages. PMA treatment induces a terminal differentiation: cells no longer divide, they adhere, metabolise more slowly and take on an appearance of a real macrophage.

HT-29 and Caco-2 cells were grown at 37 ºC in an atmosphere of 5 % $CO_2$ and 95 % air at a relative humidity of approximately 95 %. Cells were maintained in T-75 flasks using Minimum Essential Medium (MEM, PAA Laboratories, Yeovil, UK) supplemented with 10 % foetal bovine serum (FBS "Gold", PAA Laboratories), 1 % penicillin/streptomycin and 1% fungizone (Invitrogen, Paisley, UK). The growth medium was changed every 2-3 days. Upon reaching confluence, cells were treated with trypsin–EDTA solution (Sigma, St Louis, MO, USA) and split 1/10 to allow for continuous growth.

#### *3.4.6.2. Cellular uptake studies*

HT-29 and Caco-2 cells were grown on 6-well plates and incubated with four different concentrations of FeNPs (0, 0.5, 1 and 2 mM) and $FeSO_4$ (0, 0.25, 0.5 and 1 mM) during 48 h. For

each experiment, every condition was investigated in triplicate wells. After washing with Phosphate Buffered Saline (PBS), cell pellets were collected for the quantification of total iron by ICP-MS.

#### *3.4.6.3. Total iron quantification in cell samples*

For this goal, cell pellets were lysed using an acid digestion protocol consisted on the addition of 0.5 mL sub-boiling $HNO_3$ and 0.5 mL $H_2O_2$ 30 % and incubation at 70 $^oC$ for 4 hours. Total iron quantification was measured by collision cell ICP-MS ($H_2$ mode, iCAP™ TQ ICP-MS, Thermo Fisher Scientific). Calibration curves were prepared following the germanium addition technique as an internal standard, using stock solutions of 1000 mg $L^{-1}$ (Merck). The mean of five separate replicates was used for determination of iron concentration. Obtained values were expressed as pg Fe $cell^{-1}$.

#### *3.4.6.4. Nanoparticle extraction protocol*

In order to separate particle-bound from unbound cell proteins prior to HPLC speciation, an extraction protocol was carried out following Iglesias et al. publication [160]. In brief, cell samples were mixed with a protease inhibitor cocktail (Sigma-Aldrich) and centrifuged 10000 g for 5 min at 4 $^oC$ with the aim of isolating nanoparticles content in the supernatant from cell debris precipitated. Then, purification is achieved by high concentrated sucrose solution (0.7 M, Sigma-Aldrich), Phosphate Buffered Saline and centrifugation steps for 30 min at 18000 g keeping always the temperature constant to 4 $^oC$. Extracts were stored in the fridge until injection on the chromatographic system.

#### *3.4.6.5. Sample preparation for LA-ICP-MS measurements*

For LA-ICP-MS experiments, Caco-2 cells were grown on sterile coverslips (Thermo Fisher Scientific, Waltham, USA) in an 8-well plate. 4 wells were used as control and the rest were incubated with 500 µL of iron nanoparticle suspension (0.7 mM FeNPs) in standard cell culture medium. After an exposure time of 48 h, Caco-2 cells were washed thoroughly with phosphate buffered saline (PBS), immediately fixed with 4 % para-formaldehyde in PBS, and dehydrated in a graded series of ethanol for LA-ICP-MS analysis.

#### *3.4.6.6. Viability assays*

To evaluate the potential cytotoxicity induced by the FeNPs, a WST-Assay (Roche Diagnostics, Mannheim, Germany) was carried out in THP-1 monocytes and macrophages. This is a colorimetric assay based on the use of tetrazolium salts, that are cleaved to a soluble

formazan by a complex cellular mechanism that occurs primarily at the cell surface. This bioreduction is largely dependent on the glycolytic production of NAD(P)H in viable cells (Figure 15.A). Therefore, the amount of formazan dye formed directly correlates to the number of metabolically active cells in the culture.

Cells grown in a 96-well flat bottom plate, are incubated with the WST-1 reagent for 2 h in a humidified atmosphere (37 $^{o}$C, 5 % $CO_2$, 87 % humidity). After this incubation period, the formazan dye formed is quantified with a scanning multiwell spectrophotometer. The measured absorbance at appropriate wavelength directly correlates to the number of viable cells (the wavelength for measuring the absorbance of formazan product is between 420-480 nm with a maximum absorption at about 450 nm). For best results, the following protocol was carried out:

- THP-1 Monocytes and macrophages, grown from THP-1 by PMA addition and 24 h incubation, were seeded at a density of 1 $10^4$ cells/well (measured by CASY® MODEL TT cell counter + analyser, Roche INNOVATIS AG, Germany) in 96-well plates (100 µL/well). (culture medium: RPMI + BSA 10 % (50 mL), + Sodium pyruvate (5 mL), + penycillamine/streptomicine (5 mL), + HEPES (5 mL).
- Cells were then treated with different concentrations of FeNPs (0-4.5 mM).
- After 24 h incubation, the cell proliferation reagent WST-1 for viability/cytotoxicity studies was used (10 µL/well, 1:10 final dilution, including a medium control; 2 h incubation).
- Solutions from each well are collected in Eppendorfs for centrifugation (13000 rpm x 15 min) and supernatant is transferred to a new 96-well plate to be measured in a TECAN GENios microplate reader (TECAN, Switzerland) at 450 nm.

Similarly, a MTT-assay was conducted in Caco-2 and HT-29. The MTT assay involves the conversion of the water soluble MTT (3-(4,5-dimethylthiazol-2-yl)-2,5-diphenyltetrazolium bromide) to an insoluble formazan. The formazan is then solubilized, and the concentration determined by absorbance at 570 nm (Figure 15.B). Cells grown in a 96-well flat bottom plate are incubated with different concentrations of FeNPs (0 to 4 mM, in triplicate wells) for 48 h. The MTT reagent is added and incubated for 2 h in a humidified atmosphere (37 $^{o}$C, 5 % $CO_2$, 95 % humidity). After this incubation period, the formazan dye formed is quantified with a

scanning multiwell spectrophotometer. The measured absorbance at the appropriate wavelength of 570 nm directly correlates to the number of viable cells.

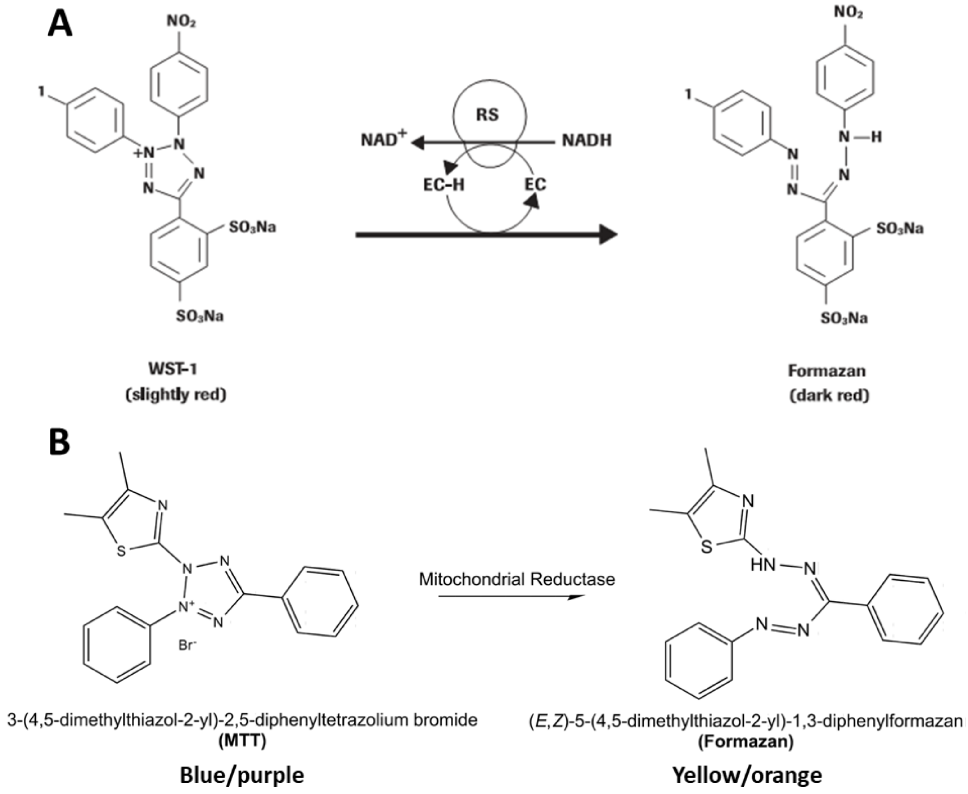


***Figure 15. A. Cleavage of the tetrazolium salt WST-1 (4-[3-(4-Iodophenyl)-2-(4-nitrophenyl)-2H-5-tetrazolio]-1,3-benzene disulfonate) to formazan. (EC = electron coupling reagent RS = mitochondrial succinate-tetrazolium-reductase system). B. Transformation of the MTT reagent into Formazan by mitochondrial reductase action.***

### *3.4.6.7. Oxidative stress assay*

To evaluate the oxidative damage caused by FeNPs, Caco-2 cells were seeded at a density of $25x10^3$ cells/well in a 96-well plate and incubated overnight to allow them to grow. The cells were incubated with FeNPs and $FeSO_4$ at 0.25 mM for 24 hours. ROS Assay kit (Bioquochem, Spain), uses 2'-7'dichlorofluorescin diacetate (DCFH-DA), a cell permeant reagent fluorogenic dye that measures hydroxyl, peroxyl and other ROS activity in the cell. After cell uptake, DCFH-DA is deacetylated by cellular esterases to a non-fluorescent compound, which is later oxidized by ROS into 2'-7'dichlorofluorescein (DCF). In Figure 16, the reaction mechanism is shown. DCF is a fluorescent compound with a maximum excitation and emission spectra of 485 nm and 535 nm, respectively. Fluorescence was measured using a microplate reader (Infinitive 200, Tecan,

Zürich, Switzerland). Tert-butyl hydroperoxide (TBHP) was employed as positive control. Results from both iron species ($FeSO_4$ and FeNPs) were corrected considering cell uptake studies.

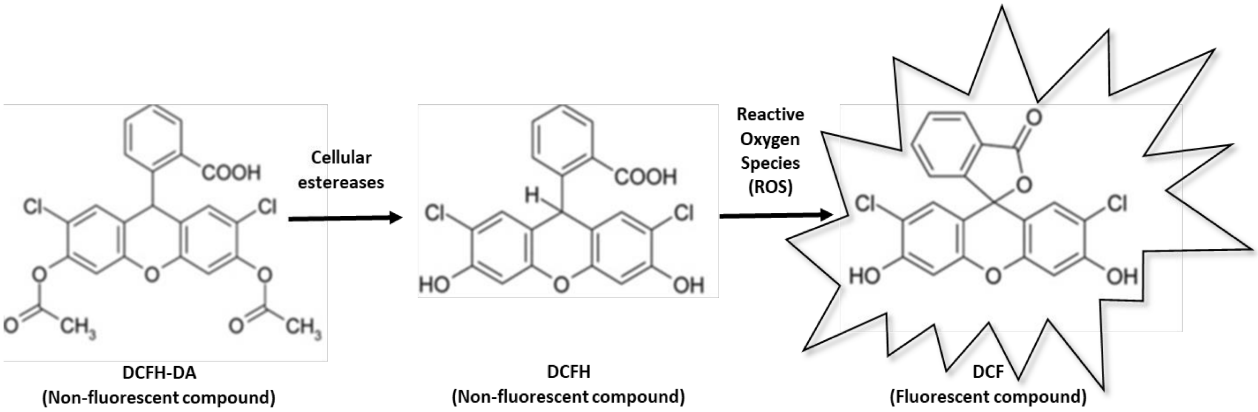


***Figure 16. ROS Assay principle.***

### 3.4.7. *In vivo* studies

*In vitro* studies provide valuable results as a first approach to understand the changes that nanodrugs can suffer and the bioavailability of the element in such biological media but cannot be compared to the reliable results, closer to real conditions that *in vivo* experiments can provide. In this work, small intestine perfusion experiments were carried out in rats as complementary approach to the *in vitro* experiments. Not only the absorption degree of the whole intestine can be determined from this experiment, but also the different distribution and accumulation of iron throughout the three regions of the small intestine (duodenum, jejunum and ileum) and the possible fate of the FeNPs after intestinal absorption.

#### *3.4.7.1. Small intestine perfusion in rats*

The study was conducted in male Wistar rats weighing 182 ± 6 g (Charles River Laboratories, L'Arbresle, France) randomly divided into two groups: (a) four rats for the study of a control group and (b) four rats for the study of the absorption of FeNPs. The rat intestinal perfusion procedure was conducted following a method described in previous publications [230]. Twenty-four hour fasted rats were initially anaesthetized (1 ml/100 g of body weight, intraperitoneally solution of sodium thiopental 0.5 % (m/V), Tiobarbital®, BBraun Vetcare, Spain) and kept under continuous anaesthesia during the entire perfusion. Then, after opening the abdominal cavity, the small intestine was exposed, and an incision was made first at the pyloric sphincter and then at the ileocecal valve, and a catheter was inserted into the lumen via the incisions. After, the intestine contents were flushed by pumping of isotonic saline solution (37 °C), the small intestine was continuously perfused with 20 mL of FeNP solution (35.6 ± 0.6 mg $L^{-1}$ FeNPs in Tyrode

solution) at a rate of 0.19 mL $min^{-1}$ at 37 °C using a peristaltic pump for 100 minutes. Composition of the perfusion solution was as follows: 8.0 g $L^{-1}$ NaCl, 0.2 g $L^{-1}$ KCl, 0.2 g $L^{-1}$ $CaCl_2$ anhydrous, 0.1 g $L^{-1}$ $MgCl_2$ anhydrous, 0.05 g $L^{-1}$ $NaH_2PO_4 \cdot H_2O$ and 1 g $L^{-1}$ glucose (pH 7). The experiment was performed in a thermoregulated chamber. After perfusion, solutions at the exit of the small intestine were collected, intestine was extracted, and its length and width were registered. Then, fractions of duodenum, jejunum and ileum were collected, as well as fractions of liver and kidney. Additionally, aliquots of blood were drawn from the aorta by a heparinized syringe. All samples were frozen at −80 °C until further analysis.

All experiments were undertaken according to Directional Guides Related to Animal Housing and Care (European Community Council, 2010), and the Animal Experimentation Ethics Committee of the University of Granada approved all procedures.

#### *3.4.7.2. Total iron quantification in animal tissues*

Tissue samples were freeze-dried and digested using a microwave oven (Ethos 1, Milestone S.r.l., Italy). In brief, approximately 0.1 g of each lyophilized sample was placed into a polytetrafluoroethylene digestion vessel. Then, 5 mL of sub-boiling nitric acid (30 %) and 3 mL of Suprapur hydrogen peroxide (30 %) were added and digestion program was applied [231]. All the plastic containers used in the analysis were previously cleaned with high purity nitric acid and ultra-pure water. Digestion and cleaning conditions selected are collected in Table 18. At the end of the digestion, the resulting solutions were made up to 50 mL with ultrapure water for further ICP-MS analysis.

**Table 18. Microwave oven digestion programs for animal tissues and cleaning.**

| | Step | Power (W) | Time (min) | Temperature (°C) |
|---|---|---|---|---|
| **Sample digestion** | 1 | 1200 | 15 | 140 |
| | 2 | 1200 | 15 | 190 |
| | 3 | 1200 | 30 | 190 |
| **Cleaning** | 1 | 900 | 10 | 150 |
| | 2 | 900 | 10 | 150 |

Iron total quantification was measured by collision cell ICP-MS ($H_2$ mode, iCAP™ TQ ICP-MS, Thermo Fisher Scientific). Calibration curves were prepared following the germanium addition technique as an internal standard, using stock solutions of 1000 mg $L^{-1}$ (Merck). The mean of five

separate replicates was used for determination of iron concentration. Obtained values were expressed as mg Fe $kg^{-1}$ of dried sample.

#### *3.4.7.3. TEM images*

Cell cultures and other tissues samples (blood, spleen) were fixed with fresh primary fixative (1.5 % glutaraldehyde, 1.0 % formaldehyde in 0.05 M sodium cacodylate buffer, pH 7.4) and post-fixed with secondary fixative (1 % osmium tetroxide, 1 % potassium ferrocyanide in Milli Q water) followed by dehydration with ascending series of alcohol before embedding samples in epoxy resin. Ultra-thin sections were cut and doubly stained with uranyl acetate and lead citrate. A transmission electron microscope LIBRA 120 PLUS microscope at 120 kV (Carl Zeiss SMT., Oberkochen, Germany) was used to determine the distribution and uptake of FeNPs into cells.

# 4 RESULTS AND DISCUSSION

# 4 RESULTS AND DISCUSSION

When working with nanoparticles, especially in living organisms, it is important to check specific properties that affect enormously the nanoparticle structure. Agglomeration/aggregation, polydispersity index, solubilization grade and, consequently, degradation level into ionic species are features that need to be well-established before designing an experiment. The analytical techniques to face up these challenges must combine separation and quantification competences, using suitable detectors to overcome the limitation of extremely narrow size range between those species. In fact, the interactions of nanomedicines with their biological environment are complex issues that have to deal with the "a priori" controllable properties of the particles (size and shape, surface chemistry, pH stability) and the unhandled properties of the surrounding media once the nanoparticle penetrates the cell, such as the cellular uptake, the degree of protein adsorption, the bio-distribution pattern or the influence that this media play on the nanoparticle structure [117].

In the framework of this study, transmission electron microscopy as well as different spectroscopy techniques (spectrophotometry, light scattering, X-ray diffraction) especially, mass spectrometry, were used to provide valuable information about this kind of nanostructures and evaluate their interaction in different biological media.

Moreover, two different nanosystems based on iron preparations for the treatment of anaemia were evaluated. On the one hand, Venofer® is a commercial preparation available in the market for the intravenous treatment of severe anaemia based on iron-sucrose nanoparticles. There are several commercial preparations based on iron nanoparticles with different carbohydrate shells, which overcome anaemia's disease efficiently. But, although their use is approved by official organisms (as the FDA in USA, or the EMA in the EU), the mechanism of iron release that takes place in the human body needs further investigations. This work may serve as starting point to further investigate other iron preparations available in the pharmaceutical industry.

On the other hand, the most extended treatment for anaemia has always been the oral iron supplementation due to its inexpensive costs and the ease of administration. However, there are not products in the market including this type of nanostructures to enhance the effectiveness of the treatment, and thus, numerous side effects are associated nowadays to this oral treatment. Therefore, the need for the development of better iron preparations for the oral treatment of anaemia is clear and the use of nanodrugs play an important role not only in the increase of bioavailability, but also in the reduction of undesirable effects. In this sense, FeNPs

mimicking the iron mineral core of ferritin have been here synthesized and studies concerning physico-chemical characterization as well as *in vitro* and *in vivo* assessment of these nanomaterials have been carried out in order to provide new insights and contribute to the future launch of this type of oral iron supplements to the market.

## 4.1. Evaluation of iron bioavailability from Venofer® in biofluids

In this work, we have designed quantitative strategies for evaluation of iron solubilization levels and transportation among serum proteins from parenteral solutions using isotopically labelled iron ($^{57}$Fe) [232, 233]. This study uses Venofer® as model intravenous iron-formulation (currently in use). The first part of the study was focused on the complete characterization of this pharmaceutical preparation in terms of the different physico-chemical characteristics. Secondly, iron bioavailability studies were performed by incubation of the commercial preparation with human serum from healthy donors to establish direct iron solubilization levels and the interaction of the released iron with serum proteins. This was addressed by two different speciation experiments: first, since serum transferrin is the main iron transporter in this fluid, the level of transferrin saturation was evaluated in serum samples before and after incubation with Venofer® and additionally, the interaction with other serum proteins was also evaluated [234].

### 4.1.1. Characterization of iron-sucrose nanosuspension: Venofer®

Figure 17. shows how the nanoparticles appear in Venofer® solution by HR-TEM technique. The iron (III) hydroxide core of nanoparticles seems to be spherical, suspension is highly homogeneous, without any aggregation or agglomeration, and its respective particle size distribution is shown in the figure.

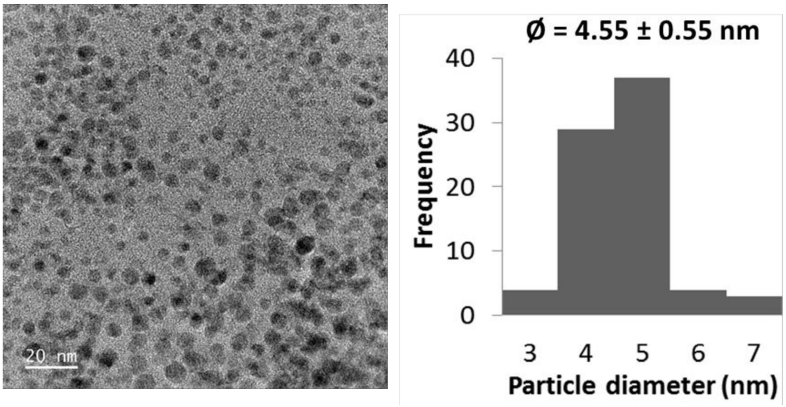


***Figure 17. HR-TEM image of a diluted aliquot of Venofer® and size histogram revealing an average size between 4 and 5 nm.***

EDX technique was also used to determine the chemical composition (Figure 18).

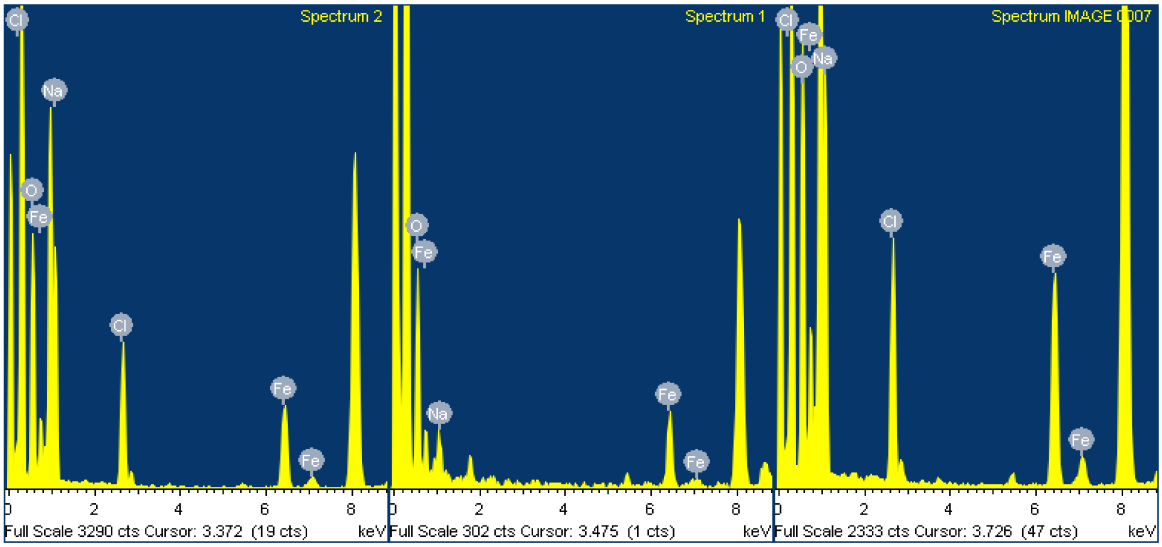


***Figure 18. EDX spectrum for the analysis of Venofer®, where its elemental composition is confirmed.***

The dispersion in size as well as the NPs hydrodynamic diameter (regarding the coating provided by the sucrose oligomers) were assessed by DLS for Venofer®. The observed results are plotted in Figure 19 revealing that the hydrodynamic diameter is around 15.1 ± 2.0 nm (with a polydispersity index of 0.19). This means that these suspensions fit the requirements for being injected intravenously (hydrodynamic diameter less than 150 nm) and that the sucrose coating corresponds to about 9-10 nm similar to the coating thickness reported for other oligosaccharides [235]. A second population around 150 nm of much lower abundance can be also detected, which could be ascribed to some partial aggregation of the preparation. Therefore, Venofer®, used as parenteral iron formulation, formed a nano-dispersed solution

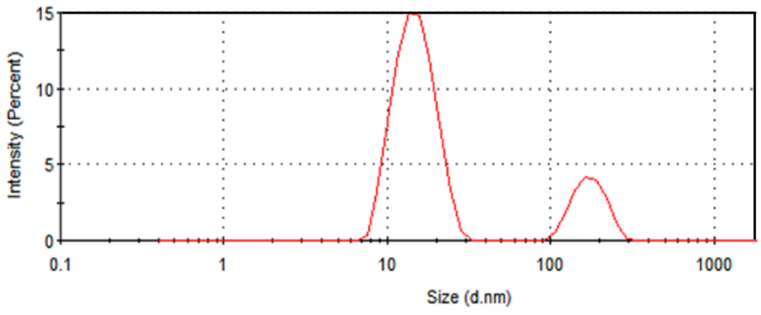


| Z-average (d. nm) | 15.11 ± 1.91 |
|---|---|
| PdI | 0.191 |

***Figure 19. DLS measurement of the hydrodynamic diameter of the Venofer® nanoparticles.***

rather than aggregates or agglomerates as commonly obtained upon titration of an acidic Fe(II)/Fe(III) solution with a base in the presence of sucrose.

A UV-vis spectrum was also obtained to evaluate the energy band gap of the semiconductor Fe-based nanomaterial. The optical absorbance measurement was carried out at room conditions and Figure 20 shows the absorption profile obtained for the Venofer® at two different dilutions of the stock solution revealing comparative results to previously published ones that exhibit two weak absorption bands at 470-500 nm and 300 nm, respectively [236]. The 470–500 nm band is attributed to the d–d transition of octahedral high spin $d^5$ Fe(III) while the 300-nm band shows that the iron is chelated to oxygen (providing an oxo-metal charge transfer absorption band).

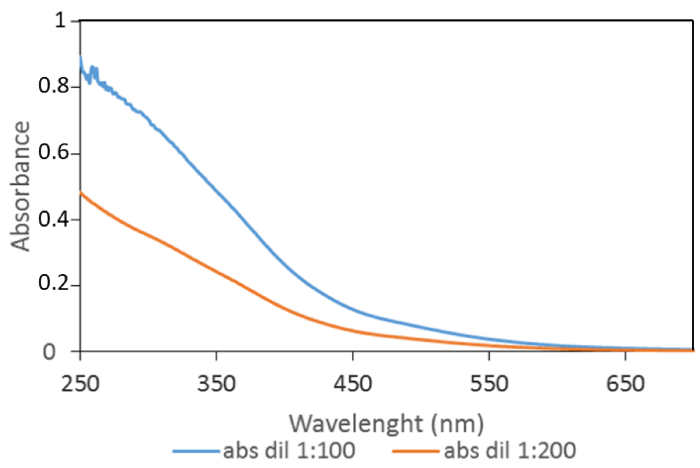


***Figure 20. UV-vis absorption spectra at two different dilutions (0.9 % NaCl) of the preparation 1:100 (blue trace) and 1:200 (orange trace).***

Final characterization of the commercial preparation was conducted by SEC-UV-vis (Figure 21.A, 21.B) and SEC-ICP-MS (Figure 21.C.) in order to evaluate the possible presence of other Fe containing species (e.g. free Fe) in the formulation. The obtained chromatograms can be seen in the following figures. In Figure 21.B, UV-vis detection shows a main peak centered at 30 minutes which can be wrongly attributed to the presence of iron. Figure 21.C., corresponding to ICP-MS detection and for two different dilutions of Venofer® (2 and 20 ppm of the drug) injected into the chromatographic column displays a main Fe containing peak that can be observed at about 26 minutes with a broad profile corresponding to approximately 21.5 kDa according to prior calibration of the chromatographic column (Figure 21.A). This value is below the range of the sizes provided by the manufacturer (34-60 kDa).

Considering that the nanoparticles have proved to be spherical by HR-TEM, the radius can be then directly extracted from these data. In this case, the calculated hydrodynamic diameter by SEC (~4 nm) turned out to be significantly lower than this provided by DLS measurements (15 nm) by a factor of four-fold approximately. Such differences between both techniques have

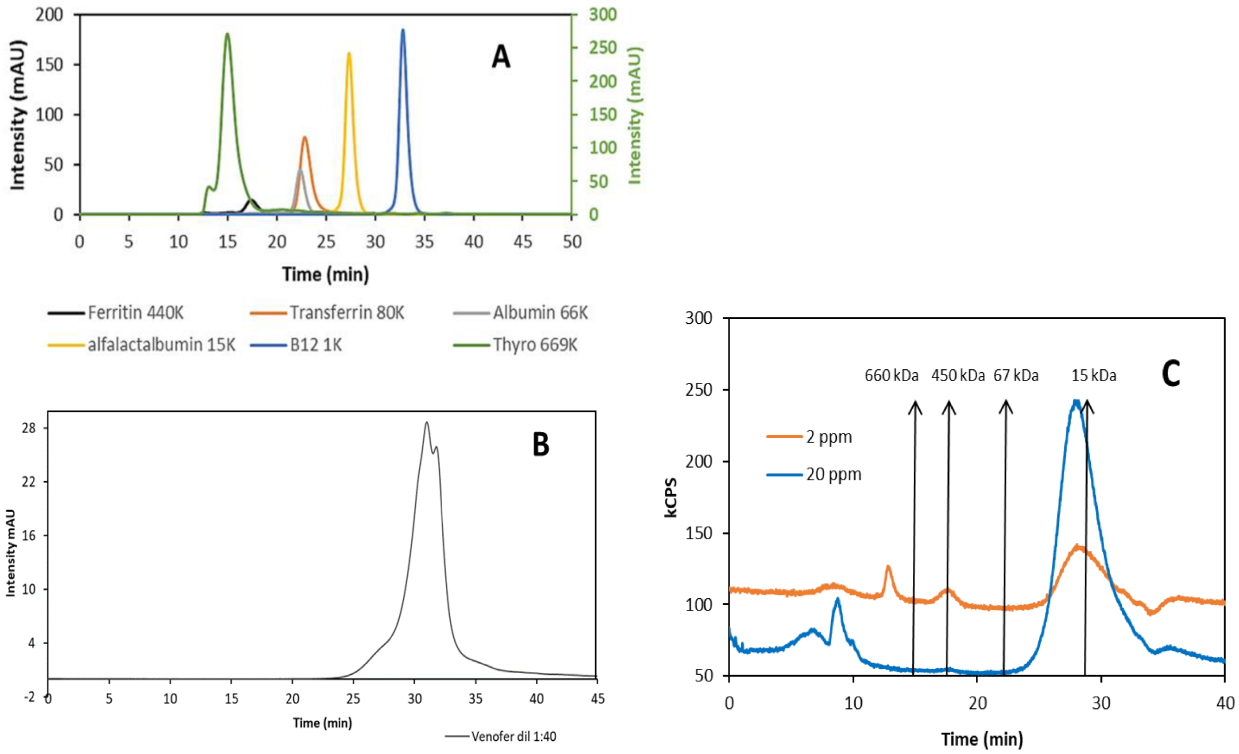


***Figure 21. Separation of Venofer® NPs by size exclusion chromatography. A. Previous column calibration with protein standards and UV-vis detection. B. SEC-UV-vis for the separation of Venofer® nanoparticles. C. SEC-ICP-MS for two different concentrations of Venofer®: 2 ppm Fe (orange trace) and 20 ppm Fe (blue trace).***

been also observed by other authors [237] and can be ascribed to unspecific interactions of the particles in the column. In any case, there was no signal ascribed to the presence of "free" iron in agreement with dialysis experiments [89].

### 4.1.2. *In vitro* solubilization experiments

To evaluate the direct bioavailability of iron from Venofer® NPs to biofluids, two different experiments were conducted. First, NPs were incubated with human serum and with whole blood, respectively, trying to mimic the solubilization conditions that might occur in real life applications. The incubation protocol and further analysis strategies used have been detailed in Section 3.4.2. In the case of whole blood, after incubation with Venofer®, blood samples were

centrifuged to separate cells from blood serum and the latter was then treated as described before for serum. Since the main pathway of most iron-oxide NPs used as intravenous supplements is the incorporation by RES for degradation of the oligosaccharide shell and liberation of the "active" iron, the present study tried to evaluate and compare such iron release in the presence (whole blood) and absence (blood serum) of the RES system.

Total iron quantification was conducted by Isotope Dilution Analysis (IDA), with the addition of a stable tracer ($^{57}Fe$) and application of the isotope dilution analysis equation as stated in Equation 2. The obtained results are compared for all the analyzed samples in Figure 22. The iron concentration found directly in the serum pool used for these incubation experiments turned to be around 1 µg $mL^{-1}$ which is in good agreement with the levels reported for this

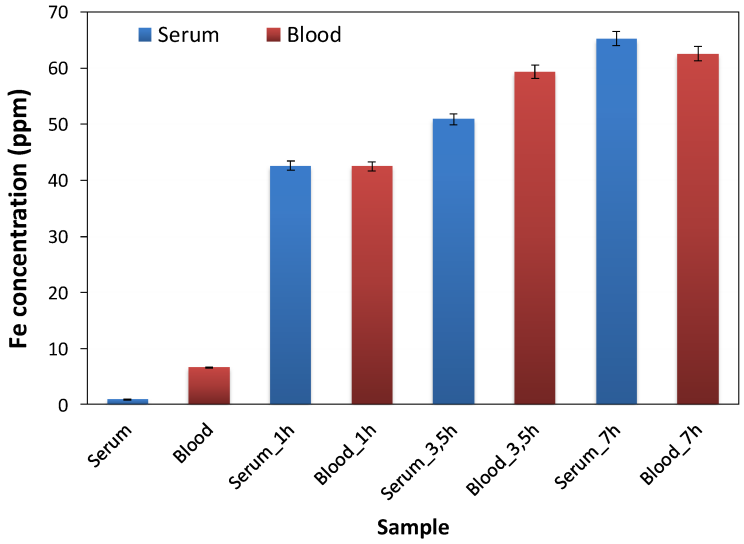


***Figure 22. Solubilization of Fe detected from Venofer® (100 ppm Fe) after incubation with serum (blue columns) and whole blood (red columns) respectively for 1, 3.5 and 7 hours. Measurement done by ICP-MS using isotope dilution analysis.***

element in serum samples [238]. Higher concentrations (about 4.5 µg $mL^{-1}$) were observed in the serum obtained from whole blood probably ascribed to hemolysis occurring during sample preparation. Regarding the incubation experiments, the obtained iron concentrations increase with the incubation time but were almost indistinguishable when comparing serum and whole blood. After one hour of incubation up to 42 % of the initial iron present in Venofer® is solubilized in both, serum and whole blood. Only a slight increase of total iron was observed after 3.5 h of incubation. Finally, up to 70 % of the initial iron present in the pharmaceutical preparation was found to be solubilized after 7 h (iron sucrose has a half-life in the organism of around 5-6 hours) [221].

Out of these experiments, it can be confirmed that a high concentration of iron is directly "dissolved" from the preparation in the presence of biological media (as they contain efficient complexing agents such as transferrin). Such results confirmed the semi-robust (kinetically) and moderately strong (thermodynamically) nature of the Venofer® formulation probably related to a weak interaction of the iron-oxide NPs with the sucrose molecules forming the coating surface. In addition, the level of iron release turned out to be time dependent. After 7 h, the solubilization level reaches 70 % of the initial iron concentration used for incubation in both, serum and whole blood. Therefore, little iron remains in the injected form after intravenous administration to the patients but as soluble iron (smaller iron nanoclusters or ions) that should be further evaluated for potential deposits in tissues etc.

### 4.1.3. Released iron incorporation into transferrin binding sites

#### *4.1.3.1. Separation of the transferrin sialoforms in serum by anion exchange chromatography*

Transferrin (Tf) contains two sites available for metals binding and in normal human serum are partially filled (~30 %) with iron atoms. The complete saturation of these metal binding sites is necessary to separate Tf sialoforms (forms with different oligosaccharide composition naturally present in serum) by anion exchange chromatography [234]. Thus, the serum blank as well as the Venofer® treated serum samples were further incubated with $^{57}Fe$ but, in this case, in the presence of $NaHCO_3$ (required as synergistic ion) for complete saturation of Tf.

Figure 23 shows the actual separation of the most abundant Tf sialoforms containing 2, 3, 4, and 5 sialic acids in a serum sample incubated with Venofer®. Figure 23.A shows the separation after 1, 3.5 and 7 h of incubation and the evolution of $^{56}Fe$ signal. The most abundant form of this glycoprotein is normally the S4 accounting for about 75 % of the total Tf (as can be identified in Figure 23 as the highest peak detected).

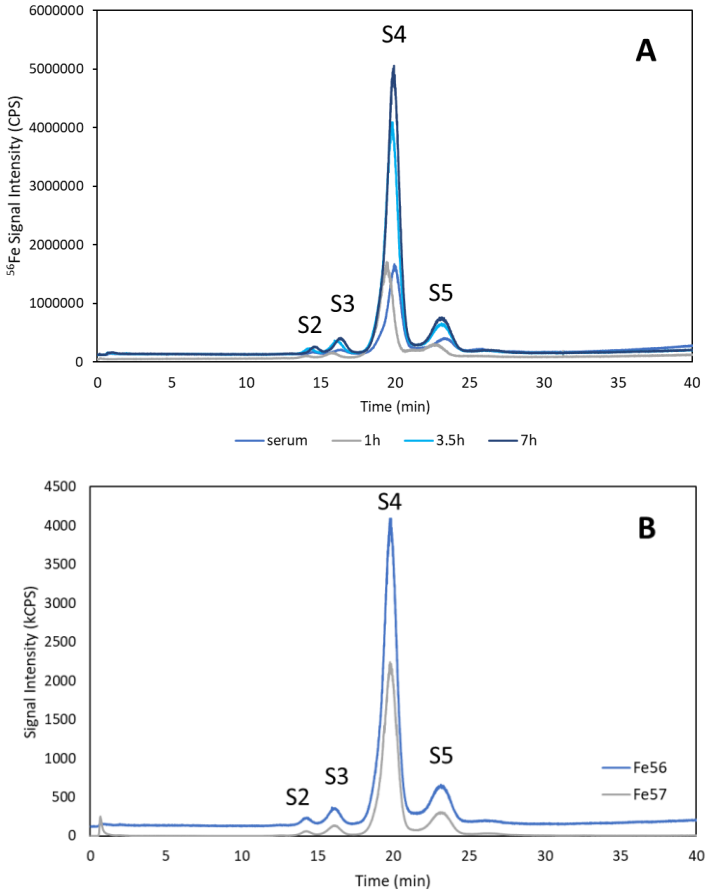


***Figure 23. Chromatograms corresponding to the separation of the sialoforms in serum by anion exchange chromatography (disialoTf-S2, trisialoTf-S3, tetrasialoTf-S4, pentasialoTf-S5) after saturation with $^{57}$Fe. A. After 1, 3.5 and 7h of incubation with Venofer® (monitorizing $^{56}$Fe signal). B. After 3.5h of incubation with Venofer® (monitorizing $^{56}$Fe and $^{57}$Fe signals).***

### *4.1.3.2. Quantitative analysis of the iron incorporated in the different sialoforms of transferrin by Isotope Pattern Deconvolution*

By using this treatment previous described and applying the so-called isotope pattern deconvolution (IPD), the contribution of endogenous and exogenous iron to the different Tf isoform can be obtained, as described elsewhere [239]. Thus, the level of natural iron will give an idea of the endogenous concentration of the metal or in other words, the level of transferrin saturation while the level of the $^{57}$Fe added for saturation will provide information on the unsaturated iron binding capacity (UIBC) of Tf [239]. The results are plotted in Figure 24 for the four sialoforms obtained (S2, S3, S4 and S5) and for the different assayed incubation times as an example. As can be seen, the same pattern was obtained for all the sialoforms.

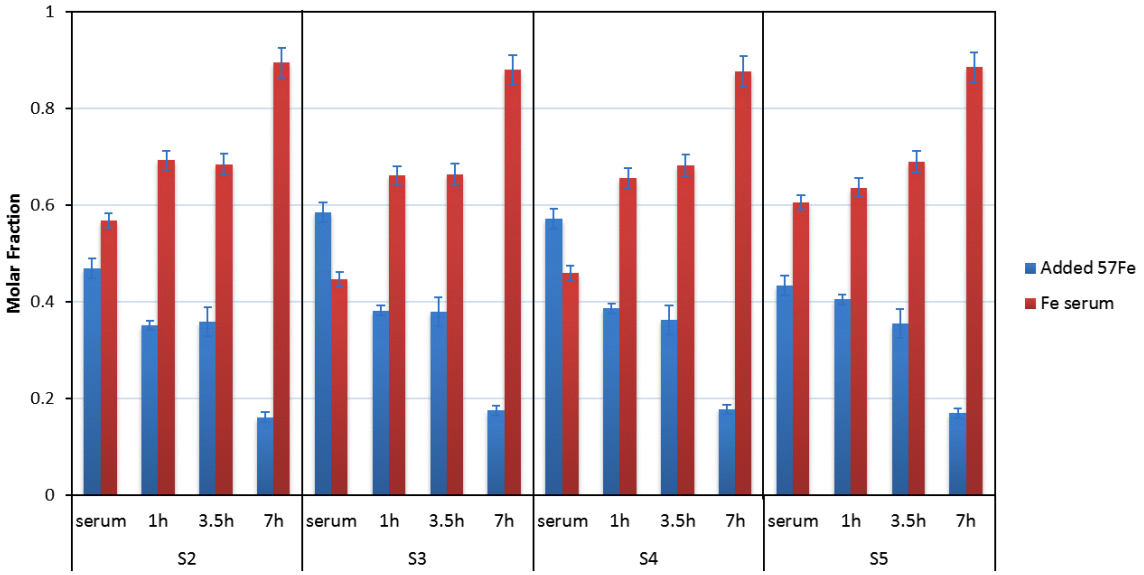


***Figure 24. Quantitative analysis of the iron incorporated in the disialoTf-S2, trisialoTf-S3, tetrasialoTf-S4 and pentasialoTf-S5 after incubation with Venofer® for 1, 3.5 and 7h (blue columns: iron required for complete saturation; red columns: iron incorporated into the corresponding sialoform).***

As expected, the longer the incubation time, the higher the incorporation of iron from Venofer® to transferrin sialoforms (red columns of Figure 24). However, according to our results, the complete iron saturation is not achieved even after 7 h of incubation, even if the incorporation of iron in Tf-binding sites reached almost 95 %. Similarly, the data of $^{57}Fe$ reveal the unsaturated ion binding capacity (UIBC) of the Tf that decreases dramatically upon exposure to Venofer® (blue columns of Figure 24). This is not surprising since serum samples with regular Tf levels (about 3 mg $mL^{-1}$) can bind up to 5 mg $L^{-1}$ of iron (Tf binding sites can accommodate two atoms of iron per molecule) and solubilized levels exceed this value. Therefore, other serum proteins or small molecular weight binders might be carrying the non-Tf bound solubilized iron from Venofer®.

### 4.1.4. Iron association to other serum proteins

Since the observed iron solubilization levels would definitely overload the iron-binding capabilities of Tf, other serum proteins could act as potential additional binders and transporters of iron in the blood of the exposed patients. In order to address this possibility, speciation experiments of other possible serum proteins were conducted in the incubated samples using UV-Vis and ICP-MS elemental detection without the addition of any external iron. Figure 25.A shows the HPLC-UV (280 nm) profile corresponding to the most abundant serum proteins

(immunoglobulin G, transferrin, albumin and ceruloplasmin) that can be separated using a previously published methodology [22]. Samples, before and after incubation with Venofer® (1, 3.5 and 7 h), were analysed in a comparative experiment. By comparing the two observed profiles of Figure 25.A, the only differences to be noted are those affecting the Tf, in which the double peak is converted in a single one upon incubation with Venofer®. Such changes correspond to the disappearance of the apo-form of Tf (normally present in serum and eluting mostly in the second peak) to originate the formation of the totally saturated form of the protein that come out at about 5.5 min with the different glycoforms together (but they cannot be well separated under this set of conditions).

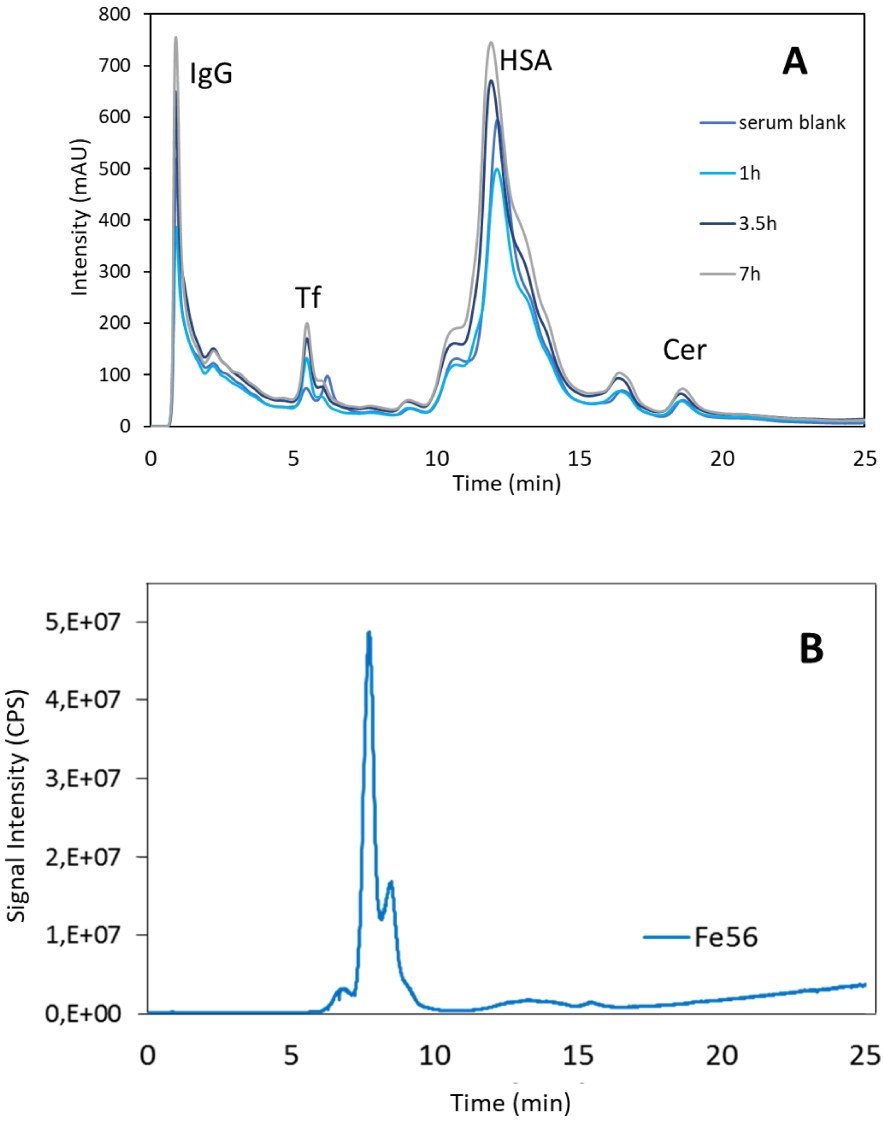


***Figure 25. Separation of the serum proteins by anion exchange chromatography after incubation with Venofer®. A. Detection by UV-vis at 280 nm, showing serum blank and serum after incubation for 1, 3.5 and 7h (Immunoglobin G: IgG, transferrin: Tf, human serum albumin: HSA and ceruloplasmin: Cer). B. Detection by ICP-MS after 1 h of incubation***

Regarding the ICP-MS trace (Figure 25.B), a main peak can be detected (at about 6.5 min) that corresponds to the iron associated to Tf (with slight delay in respect to the UV trace due to the interface between the LC and the ICP). Small iron traces seem to be present in the albumin peak additionally (see peak at about 13 min in Figure 25.B). In summary, the serum speciation results showed that albumin carries a low fraction of the solubilized iron. It is known that albumin can bind iron ions in a non-specific way in contrast to Tf [240]. Interestingly, an increase in the oxidative state of albumin (mainly referred to an increase in sulfenic (−SOH), sulfinic ($-SO_2H$) and sulfonic ($-SO_3H$) forms from oxidation of the only reduced cysteine present in albumin) has been documented upon intravenous iron administration in the form of nanoparticles in hemodialysis patients but also in experiments in vitro like those conducted here [241]. Moreover, small molecular weight iron complexes seem to be formed that elute (partially) when increasing the ionic strength of the mobile phase. Some of them might be also due to iron hydroxides that could, most likely, precipitate in the column due to the physiological pH of the mobile phase or much smaller nanoparticles remaining from the original product.

In summary, the parenteral iron formulation, Venofer®, liberates iron-ions in contact with the serum components, even in the absence of the RES system. This was confirmed by the saturation of the serum Tf binding sites after incubation of human serum with the pharmaceutical preparation whose analytical characterization did not show the presence of ultrafiltrable iron species. Other proteins present in serum, such as albumin, do not seem to carry much iron from the disrupted particles. Thus, upon injection in the patients, a fraction of NP is possibly disrupted into smaller size particles and ions that will circulate in the bloodstream.

The method here developed gives new insights for the monitoring of ions released from nanoparticles in body fluids and it can be considered as a competitive tool, especially in terms of accuracy and precision for the quantitative speciation of these iron species. Moreover, it can be considered as an appropriate alternative to study the iron pathway in other similar intravenous preparations for the treatment of anaemia.

## 4.2. *In vitro* studies on iron nanoparticles for the oral treatment of anaemia

### 4.2.1. Synthesis and purification of iron nanoparticles potentially used for the oral treatment of anaemia

Different approaches for the synthesis of iron oxide nanoparticles were carried out as it was previously mentioned in the Experimental Section.

Basically, there are two different methods for synthesizing iron oxide nanoparticles:

1) Co-precipitation of Fe(III) and Fe(II) species in presence of a coating agent in aqueous basic solution. The main advantage of this strategy is the large amount of nanomaterial that can be produced by a one-pot synthesis. However, it generally results in polydisperse samples and therefore, additional purification steps are required to separate smaller particles from the larger ones.
2) Sequential method based on the formation of the iron core, first, followed by the coating with a polysaccharide. Generally, this synthetic route leads to more homogeneous nanoparticles as the whole process takes place slowly and well controlled. However, it is more time consuming and there are more parameters that can affect the reproducibility.

Synthesized iron nanomaterials usually face a great limitation considering their strong tendency to agglomerate due to Van der Waal forces. Moreover, magnetite particles are easily air oxidized [242]. Thus, different variations were tried referring to inert atmosphere conditions and the use of different additives which can prevent or partially reduce agglomeration.

First attempts were based on the use of dextran as coating agent. Dextran is a polysaccharide which have a linear backbone of α-linked D-glucopyranosyl repeating units. It has many advantages such as its biocompatibility, biodegradability and transfection efficiency which makes it suitable for its application in biological systems. It is inexpensive, non-toxic and easily available, too [228]. Previous reduction of dextran with $NaBH_4$ was considered as an alternative to achieve a better control of the nanoparticle size. In those cases, a previous step of dextran reduction was performed 12 h at least, in advance. In that reaction, a polyol is formed which is thought to improve the stability of dextran-NP bond [243]. On the other hand, the use of nitrogen or argon during the synthesis process, not only prevents the oxidation of the magnetite, but also reduces the particle size.

The pH is also an important factor when precipitation takes place. Urea was used as an additive to the formation medium as it is known that it is decomposed in ammonia when heated over 80 $^{o}$C. The effect of ammonia added to the hydroxide ions coming from NaOH solution can help to increase pH gradually and homogenously, resulting in a more stable solution.

Ionic strength is also well established as an important parameter to control morphology and size when synthesizing metallic nanoparticles. NaCl and KCl enrichment medium was also tried as a possible variation which can improve resulting nanoparticles.

Final attempt was based on Powell et al. procedure [71] already detailed in Experimental Section. It basically consists in three steps:

1) Mixing of metal ions and ligands (tartrate and adipic acid in this case) at an initial pH value where all reagents are solubilized.
2) pH change by adding a basic solution (NaOH) so, a solid precipitate containing the nanoparticles is formed.
3) Separation and purification of the solid produced in the previous step.

This strategy can be performed in air conditions as there is no co-precipitation of $Fe^{2+}$ and $Fe^{3+}$. Only $FeCl_3$ is used as precursor reagent, so oxidation is not needed to prevent. Moreover, reaction occurs in one-pot, simplifying and accelerating considerably the nanoparticle production. Ferrihydrite core nanoparticles resulted from this protocol and structural information was checked by HR-TEM, DLS, UV-vis and X-ray diffraction techniques.

All approaches applied, as well as main limitations and considerations that justify the choice of the most suitable synthetic route were collected in Table 19.

**Table 19. Summary of the different synthesis approaches of iron oxide nanoparticles and their main considerations and limitations.**

| Approach | Atmosphere | Specification | Main drawbacks | References |
|---|---|---|---|---|
| **Dextran coated iron oxide NPs** | Nitrogen | -Reduced Dextran (by $NaBH_4$)<br>-Reflux conditions (T= 89 °C, 2 h) | -Low reproducibility<br>-Isolation from $O_2$ crucial<br>-Important loss of product during filtration steps for purification | [225] |
| **Dextran coated iron oxide NPs** | Nitrogen | -Non-reduced Dextran<br>-Ultrasonication Room temperature | | [226] |
| **Dextran coated iron oxide NPs** | Oxygen (Air) | -Reduced Dextran (by $NaBH_4$)<br>-Heating and stirring (T= 80 °C) | -Process in 2 steps: 1) Iron NPs precipitation; 2) Dextran coating step<br>-Low reproducibility | [227] |
| | | -Non-reduced Dextran<br>-Heating and stirring (T= 80 °C) | | |
| | | NaCl medium enrichment | | |
| **Dextran coated iron oxide NPs** | Nitrogen | -Urea medium enrichment<br>-Heating and stirring (T= 91 °C)<br>- Centrifugation and dialysis | -Time consuming purification step | [228] |
| | | -Urea medium enrichment<br>-Heating and stirring (T= 91 °C)<br>-No dialysis | -Important loss of product during washing steps due to solubilization | |
| **Sucrose coated iron oxide NPs** | Argon | -Heating and stirring (T= 89 °C, 3 h)<br>-Ultrasonication<br>-Ultrafiltration and dialysis | -Time consuming purification step | [225]**(adapted)** |
| **Tartrate-modified coated-iron oxide NPs** | Oxygen (Air) | -Stirring, room temperature<br>-KCl enrichment media<br>-Centrifugation and ultrafiltration | Synthesis of choice | [71] |

### 4.2.2. Characterization of synthesized iron nanoparticles

Optical and structural characterization of the synthesized nanoparticles was accomplished by using different techniques such as HR-TEM, EDX, UV-vis absorbance, DLS and SAXS/WAXS. Information about the chemical bonding, size, shape and chemical composition of the nanostructures was provided by these specific experiments.

#### *4.2.2.1. Dextran coated iron oxide NPs*

Dextran coated iron oxide NPs synthesized under $N_2$ atmosphere were first characterized by HR-TEM. Figure 26.A shows the image corresponding to the synthesis using non-reduced dextran. In this figure, nanoparticles appeared aggregated and polydisperse. It is difficult to detect the limits of the nanoparticle structure and even to define the shape. Figure 26.B shows nanoparticles using reduced dextran during the preparation. Although aggregation is still present, shape and size are better defined, and the level of polydispersity is significantly lower. However, when hydrodynamic volume is measured by DLS (Figure 26. C), a value over 500 nm is detected, which means a particularly large value in comparison to the core diameter. It suggests that the contribution of the shell as well as the associations that take place in aqueous solutions forming larger units are so considerable that it would not be a suitable structure for our purposes.

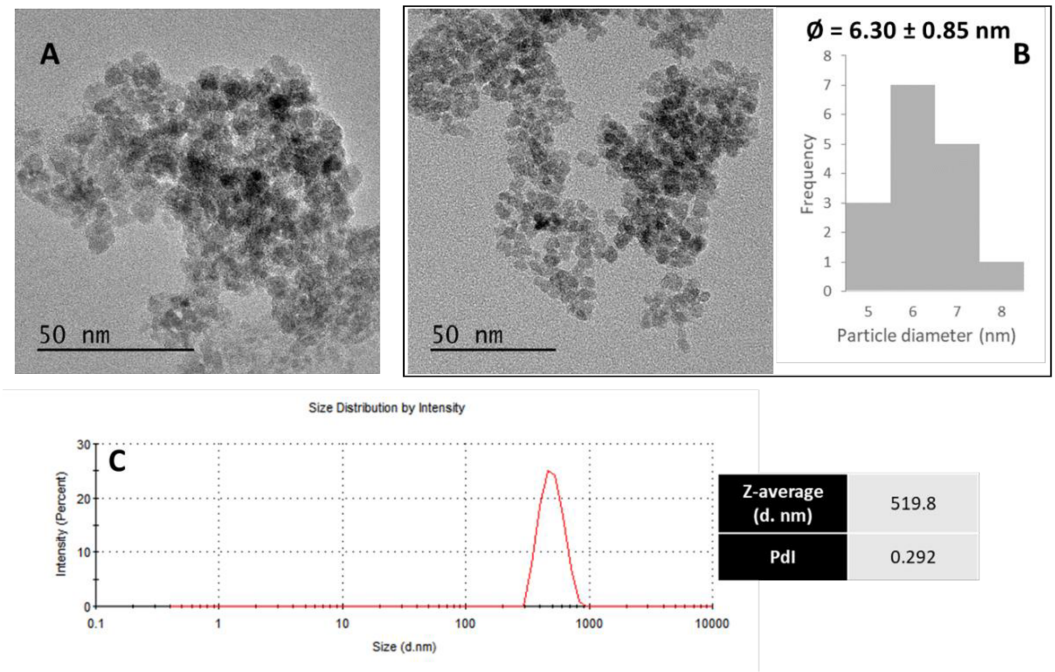


***Figure 26. Characterization of dextran coated FeNPs synthesized under $N_2$ atmosphere. A: HR-TEM image using non-reduced dextran. B: HR-TEM image after using reduced dextran with $NaBH_4$ and associated histogram showing mean core diameter of 6.30 nm. C. DLS of the FeNPs with reduced dextran revealing a hydrodynamic volume over 500 nm.***

Characterization of dextran coated iron oxide NPs using urea as additive was carried out by HR-TEM. Figure 27 shows how NPs look like when dialysis procedure is followed (Figure 27.B) or not (Figure 27.A) for purification. As can be seen, there is a significant improvement when using dialysis in terms of agglomeration, although they remain compacted. In general, NPs seem to be cleaner, so dialysis would be required as a purification step if this methodology was selected.

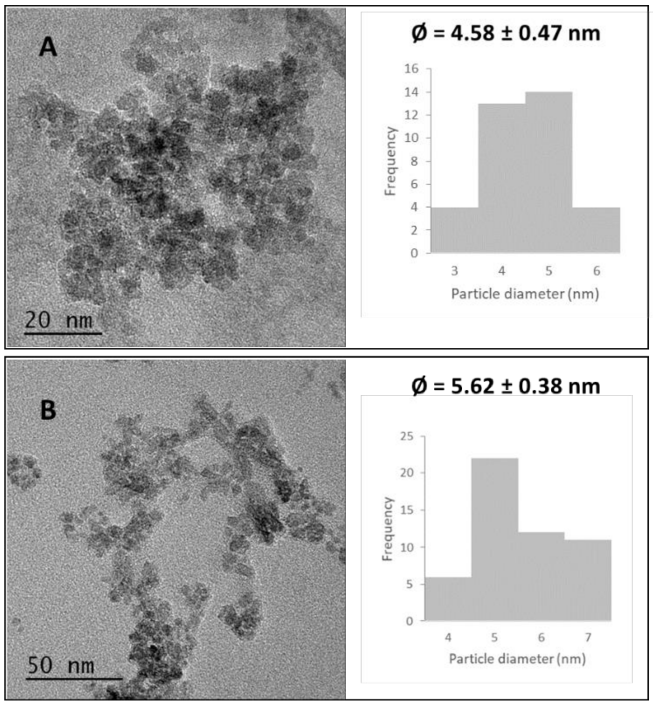


***Figure 27. Characterization of synthesized dextran coated FeNPs under $N_2$ atmosphere using urea as additive in the medium. A: HR-TEM image of FeNPs prepared without dialysis procedure and associated histogram. B: HR-TEM image using dialysis as purification procedure and its corresponding histogram.***

A different approach was tried under oxygen atmosphere. Figure 28. shows HR-TEM images of the dextran coated iron oxide NPs using non-reduced dextran (Figure 28.A) and dextran previously reduced with $NaBH_4$ (Figure 28.B). In both figures, polydispersity is present, and a lack of homogeneity is clear. Spheres and nanorods were found revealing a random nucleation of the nanostructure during the process. Same approach, using non-reduced dextran was essayed with the addition of a high concentrated saline solution, looking for a better control of shape and size of the nanoparticles. In figure 29.A., HR-TEM image of the resulting nanoparticles is presented and also the size histogram. Polydispersity is better controlled, and only spherical shape is found in this case. However, aggregation problems are still present and DLS measurements revealed a significantly higher hydrodynamic volume, below 500 nm (Figure 29.B).

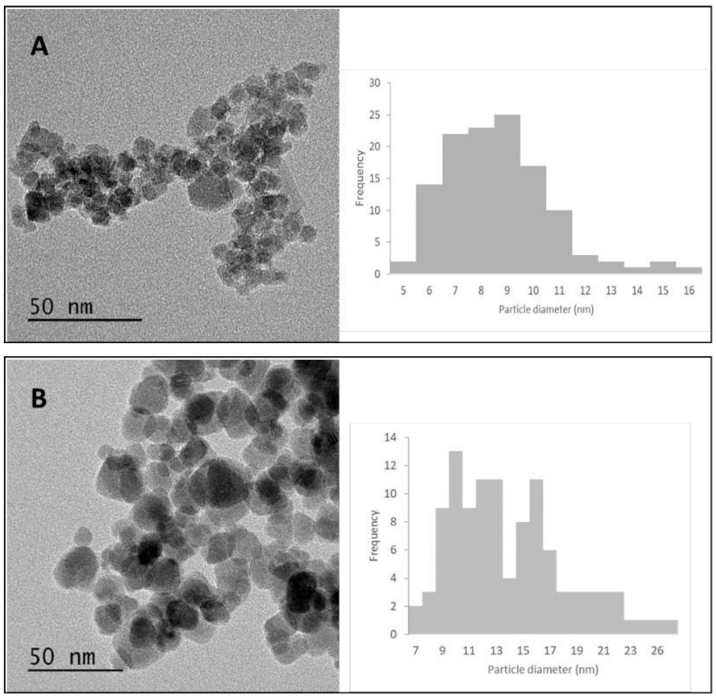


***Figure 28. Characterization of synthesized dextran coated FeNPs under $O_2$ atmosphere. A: HR-TEM image of FeNPs synthesized using non-reduced dextran and associated histogram. B: HR-TEM image of FeNPs using reduced dextran with $NaBH_4$ and its corresponding histogram.***

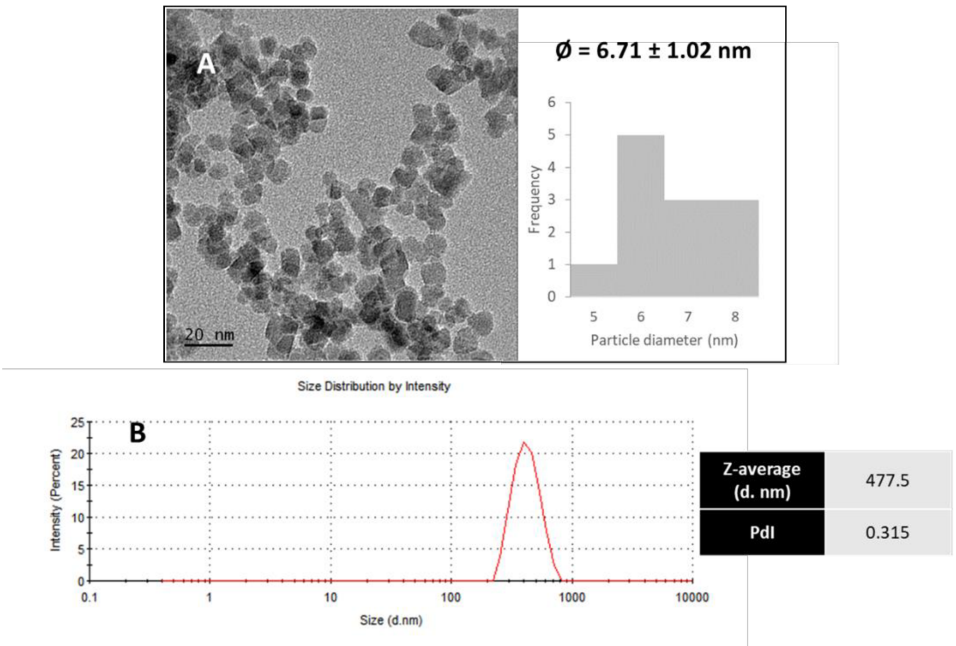


***Figure 29. Characterization of synthesized dextran coated FeNPs under $O_2$ atmosphere, using non-reduced dextran and with a NaCl solution to enrich the medium. A: HR-TEM image and its corresponding histogram. B. DLS measurement revealing a 477.5 nm hydrodynamic volume.***

#### *4.2.2.2. Sucrose coated iron oxide NPs*

In the case of sucrose coated iron oxide NPs, HR-TEM image revealed nanoparticles of approximately 9 nm of core size and particle aggregation is clear in the preparation (Figure 30.A). Although they have similar composition to the nanoparticles containing Venofer® preparation,

differences in size, aggregation and polydispersity are significant. Moreover, hydrodynamic volume measured by DLS displayed a much higher value (176.2 nm) than the core size registered by HR-TEM, suggesting the existence of a big carbohydrate shell and the association of these NPs to form larger units in solution (Figure 30.B).

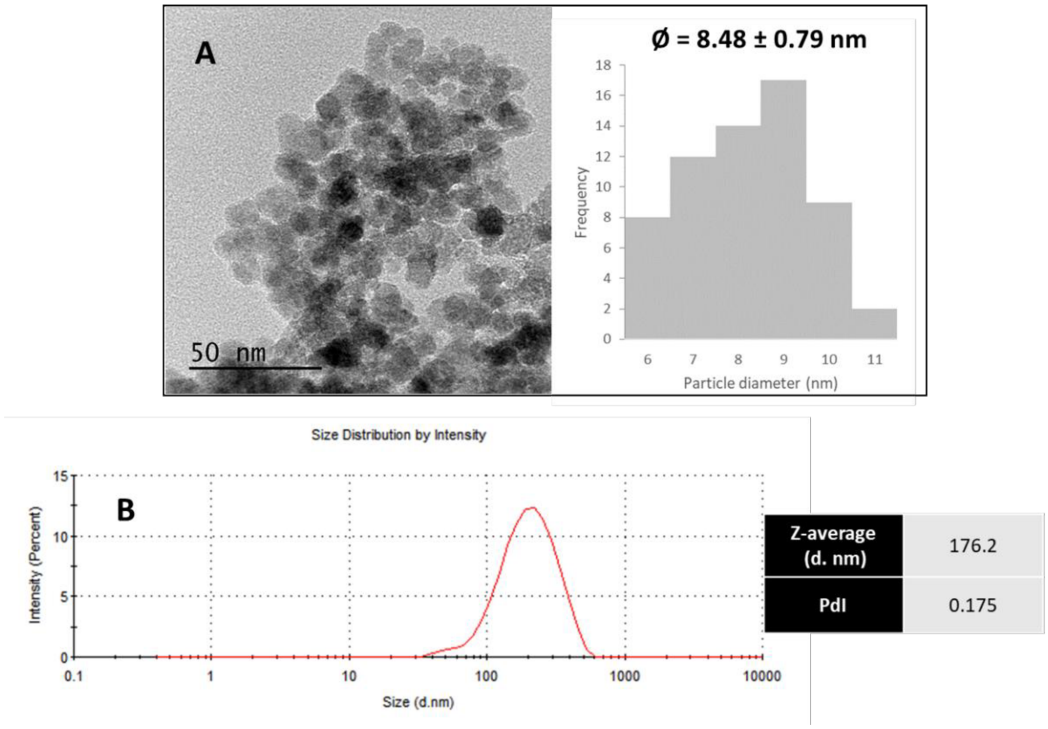


***Figure 30. Characterization of synthesized sucrose coated FeNPs under Ar atmosphere. A: HR-TEM image of FeNPs and its corresponding histogram. B: DLS measurement.***

### *4.2.2.3. Tartrate modified coated Iron Oxide NPs*

Characterization by HR-TEM can be observed in Figure 31.A. Discrete and spherical particles with no visible aggregates are shown. The average of core size is 3.65 ± 0.39 nm and homogenous size distribution is also appreciated. Moreover, dispersion in size and nanoparticle hydrodynamic volume were assessed by DLS and results are plotted in Figure 31.B. A hydrodynamic diameter of 11.77 nm with a polydispersity index of 0.276 means an acceptable monodispersing and homogeneity in this suspension and it can also be concluded that the modified tartrate shell corresponds to about 7-8 nm.

A UV-vis spectrum was obtained to evaluate the energy band gap of the semiconductor Fe-based nanomaterial. The optical absorbance measurement was carried out at room conditions and Figure 32 shows the absorption profile obtained for synthesized FeNPs previously diluted

100 times. It appears as a continuous high intensity band decreasing gradually at longer wavelengths. However, a high intensity band can be seen around 350 nm corroborating the presence of the oxo-metal charge transfer transition, expected in this kind of nanostructure in the range of 250-390 nm [236].

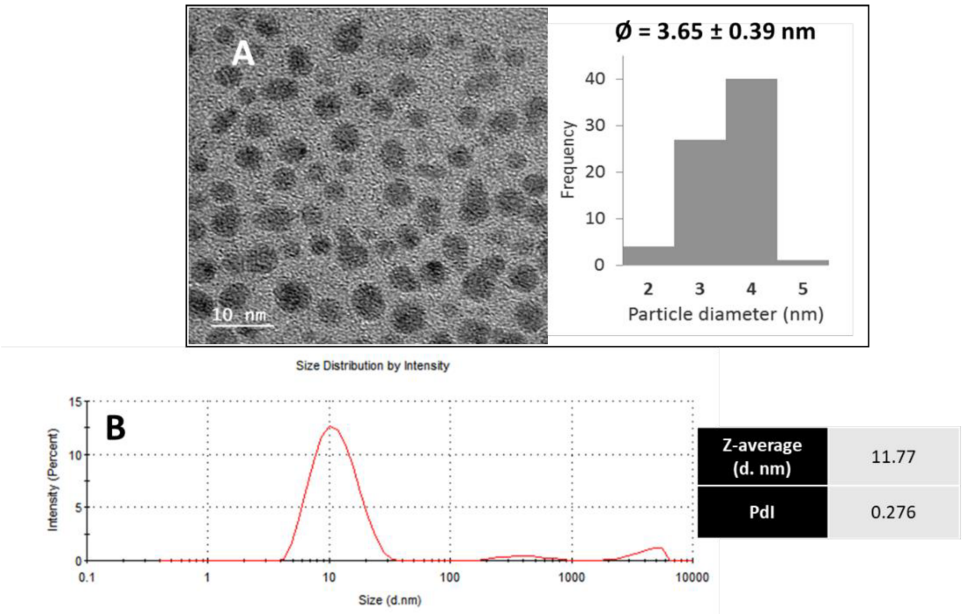


***Figure 31. A. Characterization of synthesized tartrate modified coated iron oxide NPs and size histogram associated showing a mean diameter of less than 4 nm. B. DLS confirming a hydrodynamic volume of 11.77 nm in aqueous solution.***

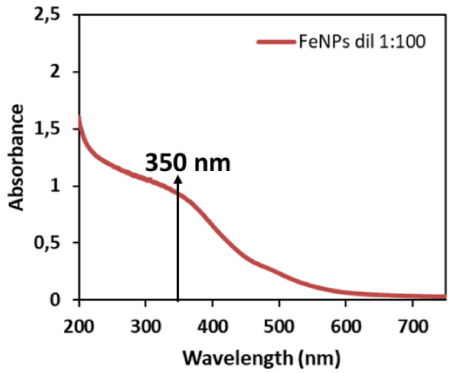


***Figure 32. UV-vis absorption spectrum at 1:100 dilution of the tartrate modified iron NPs.***

#### *4.2.2.3.1. Isotopically enriched $^{57}$FeNPs*

Tartrate-modified iron nanoparticles were synthesized in the laboratory following the procedure cited in Experimental Section, including the preparation of the $^{57}FeCl_3$ precursor. They do not present significant aggregation or agglomeration by looking at the HR-TEM image (Figure 33.A) and the average of core size, although smaller, is in the range of the previous self-

synthesized FeNPs (around 3 nm). EDX spectrum is represented in Figure 33.B. and proofs the chemical composition of the nanoparticle suspension.

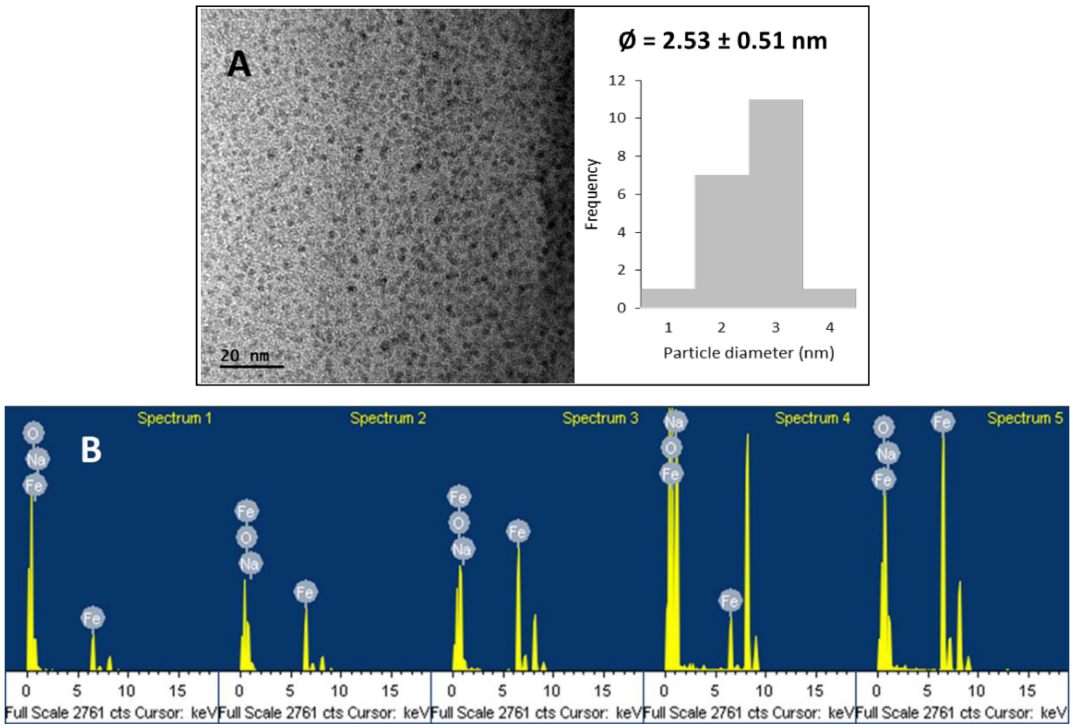


***Figure 33. HR-TEM image of $^{57}$FeNPs and associated histogram. B. EDX spectrum for the analysis of $^{57}$FeNPs, where its elemental composition is confirmed.***

Quantification studies by ICP-MS revealed the percentage of Fe nanoparticulate and soluble present in the suspension. Data from the measurements of the suspension before UHF and after UHF (collecting the fraction accumulated in the filter and the fraction that pass through the filter) are shown in Table 20.

**Table 20. Quantitative analysis of total Fe in synthesized $^{57}$Fe-NPs by ICP-MS.**

| $^{57}$FeNPs | Total Fe (mg) | Fe content (%) |
|---|---|---|
| **Before UHF** | 4.846 | |
| **UHF (Nanoparticulate fraction)** | 2.741 | 56.5 |
| **Soluble Fe** | 2.19 | 45.4 |

#### *4.2.2.3.2. Holmium-doped FeNPs*

Optical absorption spectra were recorded and compared to the tartrate modified coated iron NPs in order to determine if the doping with holmium could modify the structure. In the green trace of Figure 34 can be observed the same continuous intensity band decreasing at longer wavelengths that was detected for the original structure as well as the characteristic band at 350 nm corroborating the presence of the oxo-metal charge transfer transition once more.

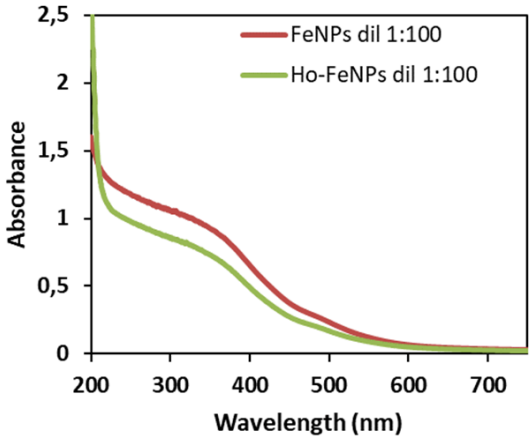


***Figure 34. UV-vis absorption spectra of FeNPs diluted 1:100 (red trace) and Holmium doped FeNPs diluted 1:100 (green trace).***

DLS measurements were also compared and hydrodynamic volume was slightly higher (5 nm more than original structure) and so the polydispersity index, although it remains below 0.5 value, which determines an acceptable quality for the measurement. Table 21 displays the comparison.

**Table 21. Average of hydrodynamic diameter and polydispersity index obtained by DLS for FeNPs and Fe-Ho NPs.**

| DLS | FeNPs | Fe-Ho NPs |
|---|---|---|
| **Z-average (d. nm)** | 11.77 | 16.81 |
| **PdI** | 0.276 | 0.485 |

In order to determine the structure of the nanoparticle in terms of average particle size, shape, distribution and surface-to-volume ratio, SAXS measurements were performed (Figure 35.A.). WAXS technique was also applied to elucidate crystalline structure of the nanosuspension. It only differs from SAXS in the shorter distance from sample to the detector and thus diffraction maxima at larger angles are observed (Figure 35.B.C). However, looking at the results obtained, homogeneity and monodisperse particles detected by HR-TEM were not confirmed by SAXS. Data from SAXS reveal a possible agglomeration and polydispersity. Moreover, spherical shape is not clear as the parameter P is not 4, expected value for spherical particles (except in the case of Venofer® samples, see Table 22).

**Table 22. Results from SAXS measurements expressed in terms of the Radius of gyration ($R_g$) and Porod (P), both related to the shape of the particle.**

| | $R_g$ (Radius of gyration) | P (Porod) |
|---|---|---|
| **Venofer®** | 2.1 nm | 4 |
| **Fe-Ho NPs** | 1.9 nm | 3.2 |
| **FeNPs(1 week)** | 2.9 nm | 3.35 |
| **FeNPs (freshly prepared)** | 1.8 nm | 3.1 |

From the WAXS results, akageneite structure cannot be assigned to Venofer® as it was established in the literature [236]. Moreover, no signal for nanoparticle is detected, only background in both dried and liquid samples. A possible interpretation of these results could be the non-fully crystalline structure of the NPs, although is not discarded the 2-line ferrihydrite structure for tartrate-modified NPs as established in bibliography [71].

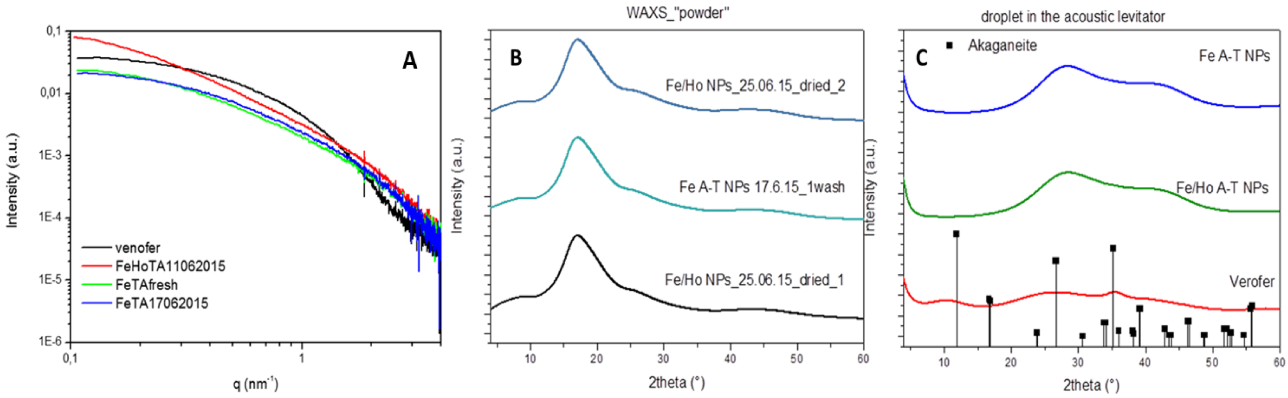


***Figure 35. A: Results obtained from SAXS measurements for Venofer® (black line, tartrate-modified NPs freshly synthesized (green line) and 1 week after the synthesis (blue line) and Holmium doped tartrate-modified NPs (red line) samples. B: WAXS measurements for dried samples: tartrate-modified NPs freshly synthesized (second line in blue) and Holmium doped tartrate-modified NPs (first and third lines in blue and black, respectively). C: measurements of Venofer® (red line), tartrate-modified NPs (blue line) and Holmium doped tartrate-modified NPs (green line) in solution are represented with results for akageneite structure that was expected (black squares).***

### 4.2.3. Uptake studies in different cell lines

#### *4.2.3.1. FeNPs characterization in cell culture medium*

The hydrodynamic mean diameters of tartrate-modified NPs were recorded by DLS using milli-Q water and cell culture medium in order to get an idea of the possible behaviour that NPs will have when interact with cells. Figure 36 shows an only peak centred in 11.40 nm

corresponding to the hydrodynamic volume of the NPs suspended in milli-Q water with a Polydispersity Index (PdI) value of 0.276, which means an acceptable monodispersion and homogeneity. However, when NPs are dispersed in cell culture medium, the only peak of the NPs is splitted in two, one centred in 11.61 nm (that is higher in intensity when the NP concentration increases) and other centred in 52.93 nm that is also found in DLS spectrum of the cell culture medium.

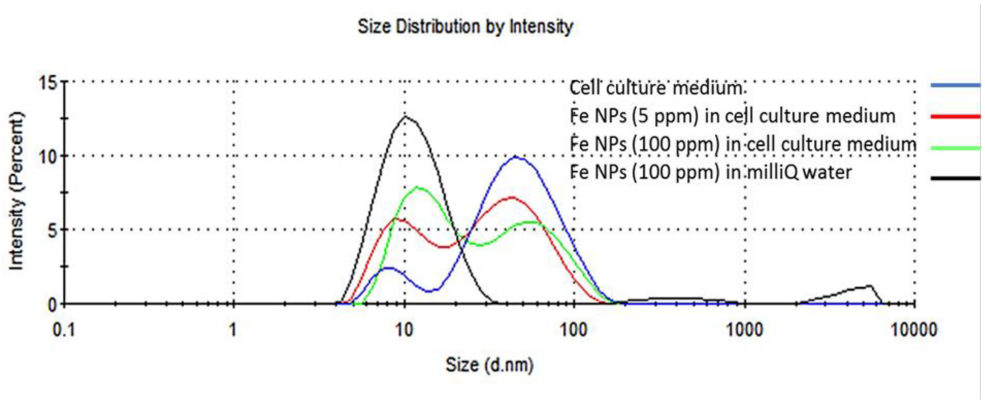


***Figure 36. Particle size analysis by DLS (Dynamic Light Scattering) to detect the dispersion of tartrate-modified NPs in cell culture medium (red and green lines) and in milli Q water (black line). Spectrum of cell culture medium was also recorded as a standard (blue line).***

### *4.2.3.2. Total iron quantification in cell samples by ICP-MS*

The FeNPs and iron salt ($FeSO_4$) were incubated at 37 $^{o}$C for up to 48 h at concentrations up to 2 mM (100 µg Fe $mL^{-1}$ in different cell lines (Caco-2 and HT-29). In Figure 37.A. the iron uptake (pg Fe/cell) is shown. Uptake increases with increasing concentration of FeNPs in both cell lines, HT-29 and Caco-2, but this increment is significantly different in Caco-2, being almost 5-times higher than in HT-29. Although the reasons of this difference concerning iron uptake are not clear, there are some limitations concerning the use of HT-29 as an *in vitro* model of intestinal cells which can contribute to the lower values of cell-associated iron detected. Actually, despite their resemblance with the small intestine enterocytes, they are colonic cells and thus, not so strongly related to iron absorption. Moreover, it has been postulated that they are closer to human foetal colonic cells because of the type of hydrolases present and the intracellular concentration of glycogen accumulated [244, 245]. It must also be remarked that under standard culture conditions, i.e., in the presence of glucose and serum, HT-29 cells are undifferentiated: morphologically they grow as a multilayer of unpolarized undifferentiated

cells; functionally, they do not express particular characteristics of intestinal epithelial cell [246, 247].

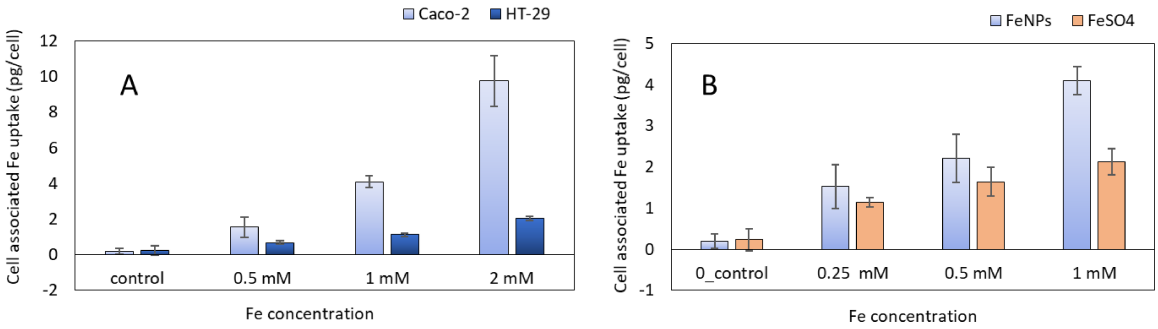


***Figure 37. A: Cell associated iron expressed in pg Fe/cell from uptake studies of FeNPs in Caco-2 (light blue bars) and HT-29 (dark blue bars). B: Cell associated iron expressed in pg Fe/cell from uptake studies of FeNPs (light blue bars) Vs FeSO4 (orange bars) in Caco-2.***

In Figure 37.B, the absorption level of $FeSO_4$ and FeNPs are compared in Caco-2 cells. There is also a clear increment of the iron uptake when the incubated iron concentration increases for both compunds. However, the intracellular iron levels are significantly higher in the case of FeNPs. In spite of using the same concentrations of iron in both cases, $FeSO_4$ is poorly internalized reaching 2.1 ± 0.3 pg Fe $cell^{-1}$ whereas the FeNPs at the same initial concentration (1 mM) reach levels of 4.1 ± 0.3 pg Fe $cell^{-1}$. These differences could be attributed to a possible absorption mechanism similar to haem iron for the FeNPs. Haem iron crosses cellular membrane of the enterocyte by a transporter protein called Haem Carrier Protein-1 (HCP1) and it is internalized by endocytosis. This mechanism has shown a better effectiveness of absorption than non-haem form [248]. The hypothesis for FeNPs uptake is supported by two main reasons: a) several clinical studies have shown that in physiological conditions, macromolecules can penetrate epithelial cells by pinocytosis [249], and b) the presence of FeNPs inside Caco-2 and HT-29 cells has been observed in this study as it is going to be discussed in the following section (Figures 38, 39)

#### *4.2.3.3. Iron uptake mechanism and subcellular distribution*

To check the accumulation and distribution of the FeNPs inside the cells, TEM images were captured after 48 h of FeNP exposure in Caco-2 and HT-29 cell lines. Figures 38 and 39 shows nanoparticles confined in vesicles inside the cells, both in Caco-2 (Figure 38) and HT-29 (Figure

39). Thus, it is proposed that FeNPs are absorbed by these endocytic vesicles following an adsorptive endocytic mechanism.

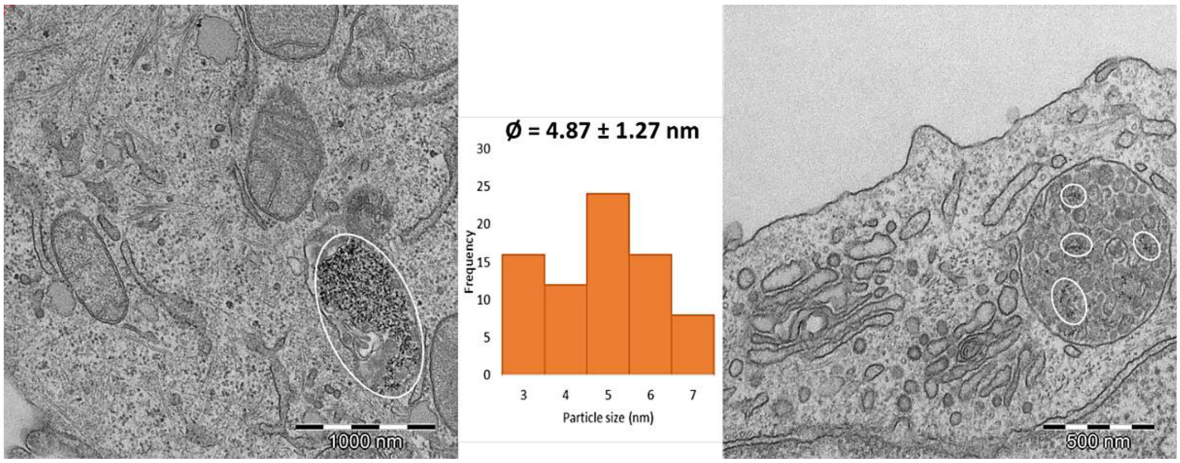


***Figure 38. TEM images after FeNPs exposure during 48 h in Caco-2.***

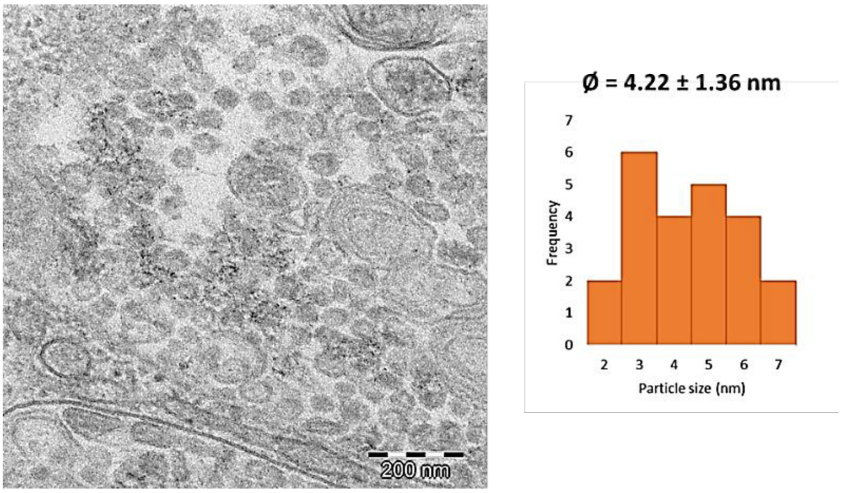


***Figure 39. TEM image after FeNPs exposure during 48 h in HT-29.***

### 4.2.4. LA-ICP-MS experiments

Caco-2 cells were incubated with FeNPs suspensions and grown as a monolayer on sterile coverslips for LA-ICP-MS investigation, fixed with formaldehyde, and dried prior to ablation. To minimize fractionation effects during LA-ICP-MS analysis, laser energy, repetition rate, spot diameter, and scan speed were optimized so that the material was completely ablated during every line scan. Final parameters were detailed in Experimental Section.

In order to obtain a high-resolution image with a spot size in scan direction smaller than the laser focus point diameter, here we applied a laser ablation scan mode that is based on the

overlap of single ablation points. This procedure requires (i) the laser energy to be high enough for complete ablation and for minimum background signal and (ii) the repetition rate high enough relative to scan speed, so that the laser spots on the surface of the sample are overlapping and the signal of the sample is generated by the difference in ablated area.

LA-ICP-MS measurements of the isotopes $^{56}$Fe and $^{57}$Fe were conducted using an ICP sector field mass spectrometer (Element XR, Thermo Fisher Scientific, Bremen, Germany) in medium mass resolution to be able to detect $^{56}$Fe without interferences.

To investigate the particle uptake and distribution we analysed isolated groups of Caco-2 cells incubated with 0.7 mM FeNPs during 48 h and we compared signals obtained with control samples. It was assumed that FeNPs were localized in vesicles inside the cell after being internalized through an endocytic pathway, as it has been shown in TEM images. In Figure 40 plots of $^{56}$Fe and $^{57}$Fe signal intensity as a function of position show the distribution of FeNPs in small group of isolated Caco-2 cells. The presence of FeNPs inside the cells is confirmed by comparing these plots with the corresponding to control samples (Figure 41). The 2D map of

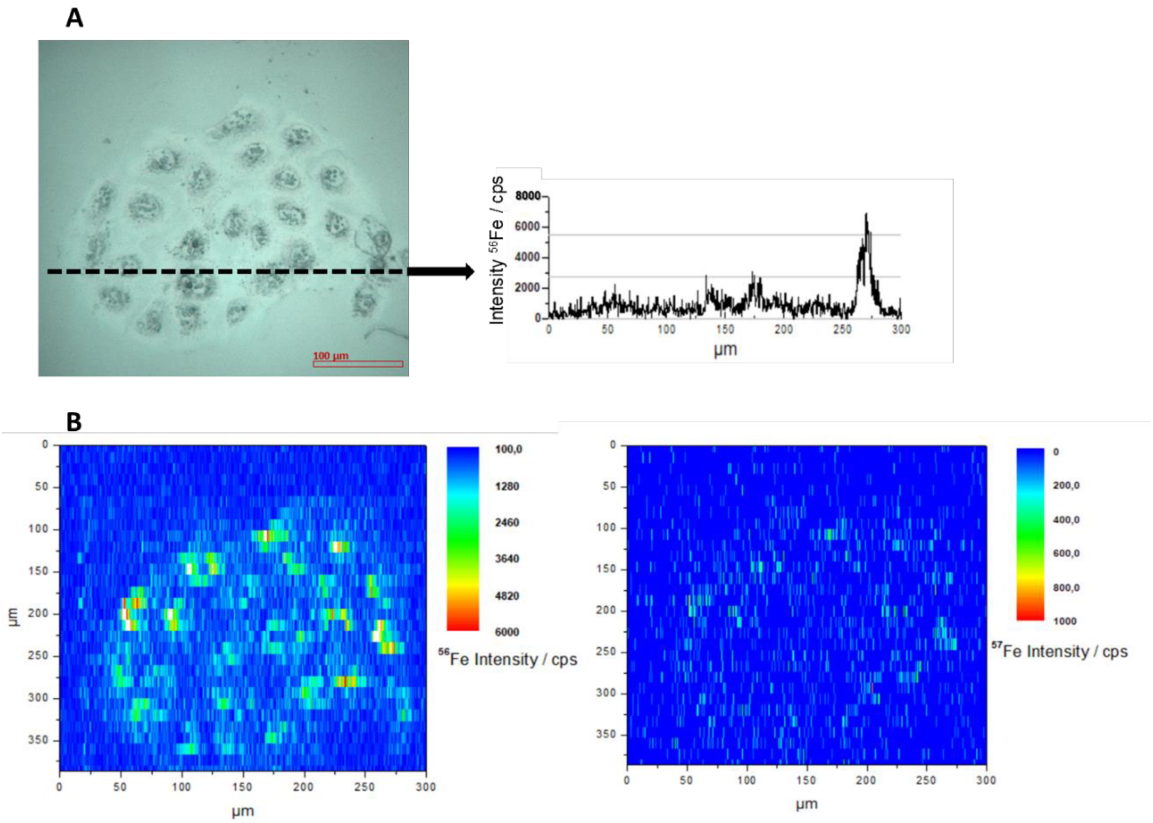


***Figure 40. (A) Bright field image and the corresponding single line scan of the cell regions marked with an arrow in first picture. Every peak in the line scans represents nanoparticles. (B) LA-ICP-MS image of the $^{56}$Fe and $^{57}$Fe intensity distribution (in CPS) inside a group of Caco-2 cells. Caco-2 cells were incubated with FeNPs in a particle concentration of 0.7 mM for 48 h. Parameters: laser spot size, 15 µm; line distance, 12 µm; scan speed, 15 µm/s; repetition rate, 10 Hz; fluence, 0.5 J/cm².***

Figure 41 indicates lower signal of $^{56}Fe$, in the range of the background, so no FeNP signal is detected.

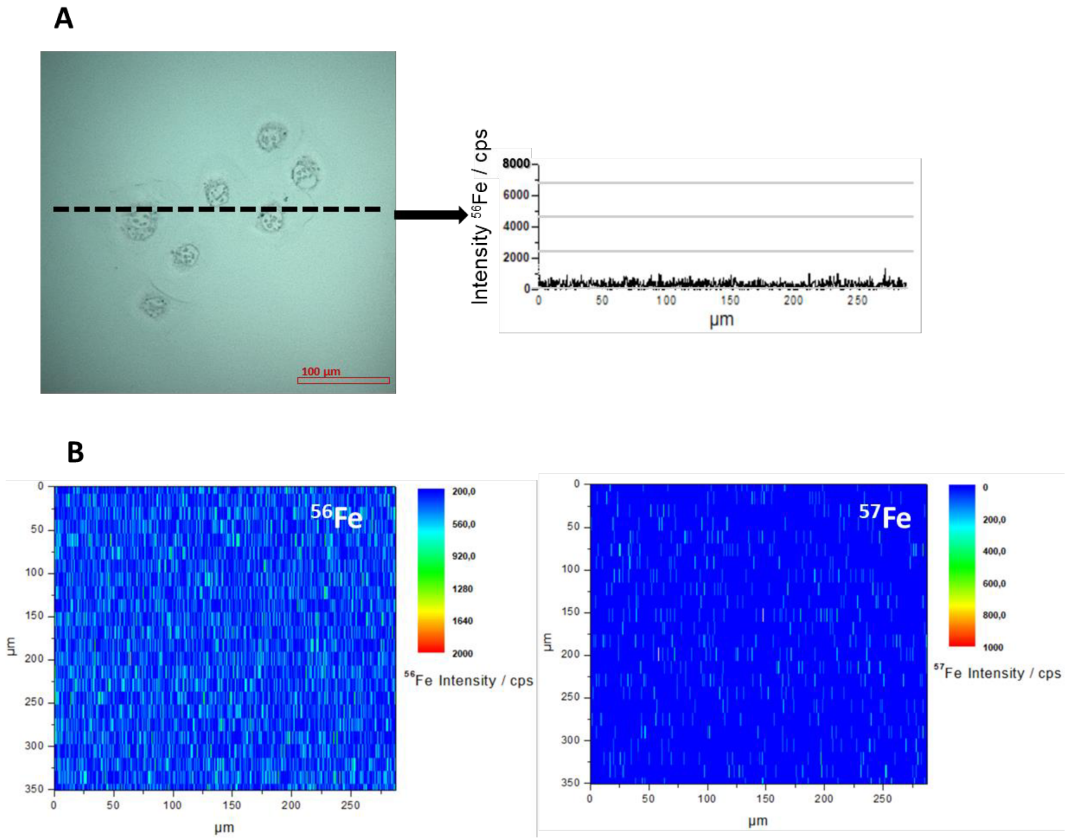


***Figure 41. (A) Bright field image and the corresponding single line scan of the cell regions marked with an arrow in first picture. (B) LA-ICP-MS image of the $^{56}Fe$ and $^{57}Fe$ intensity distribution (in CPS) inside a group of Caco-2 cells. Parameters: laser spot size, 15 µm; line distance, 12 µm; scan speed, 15 µm/s; repetition rate, 10 Hz; fluence, 0.5 J/cm$^2$.***

This example illustrates that the LA-ICP-MS approach enables one to localize FeNPs within the substructures of single Caco-2 cells and therefore can be used to investigate nanoparticle uptake and intracellular distribution. Moreover, it is considered as a complementary technique to other techniques for determination/characterization of nanoparticles, such as TEM, where elemental composition and quantification are not possible *per se*.

### 4.2.5. Toxicity assessment

#### *4.2.5.1. Cell viability assays*

Viability assays were accomplished using high concentration levels of FeNPs (up to 4000 µM) and long incubation times (48 h). Results of the MTT assay are showed in Figure 42. This colorimetric assay is based on the production of formazan via an enzymatic reduction, so the more formazan is produced, the more number of metabolically active cells are in culture. In this range of concentrations, considered in therapeutic levels, no cytotoxicity is detected neither in Caco-2 or HT-29. It should be remarked that no effects were observed on cell viability at low FeNPs concentration. But as FeNPs concentration increases, cell viability percentages also increase, especially in Caco-2 cells, which can be associated to their highest capability to absorb iron and may suggest a positive effect of the nanoparticles on the enzymatic activity. At higher FeNP concentrations, cell viability falls down until reaching control values again. This reduction could be attributed to an increase of ROS production due to the great amount of iron absorbed at these levels. In spite of these cell viability rates around 100 %, cell damage cannot be completely discarded since the cell has repair mechanisms that are impossible to detect with the MTT assay.

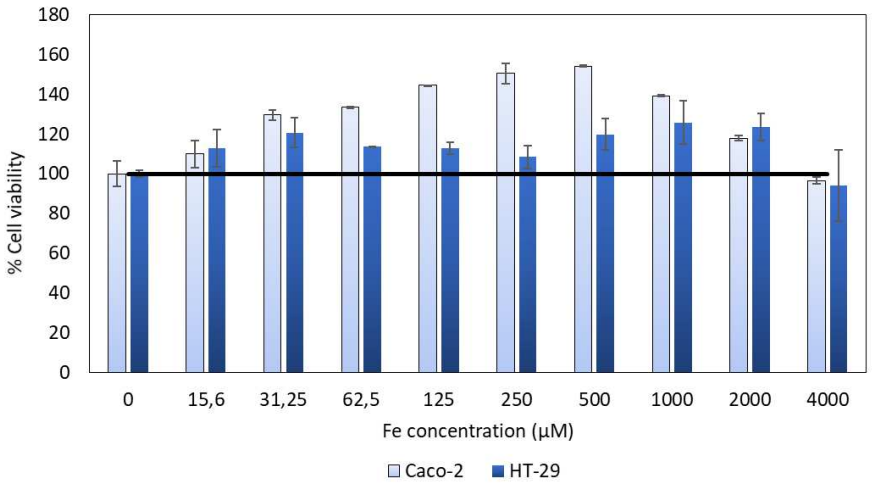


***Figure 42. Cell viability in HT-29 (dark blue bars) and Caco-2 (light blue bars) after 48 h of FeNPs exposure from 0-4000 µM of Fe concentration.***

Moreover, cytotoxicity studies based on WST-1 reagent were carried out in THP-1 monocytes and macrophages. The results, corresponding to three independent experiments, demonstrated that exposure to the synthesized FeNPs during 24 h resulted in a non-significant toxicity, especially up to 1600 µM in both cell lines, THP-1 and its differentiated line, macrophages. An increment in the cytotoxicity when incubation time is increased up to 48 h was

also noticed. Survival rates values between 100-80 % were recorded in both cell types and a more significant effect in macrophages after 48 h with 4000 µM Fe concentration was observed (Figure 43. A, B).

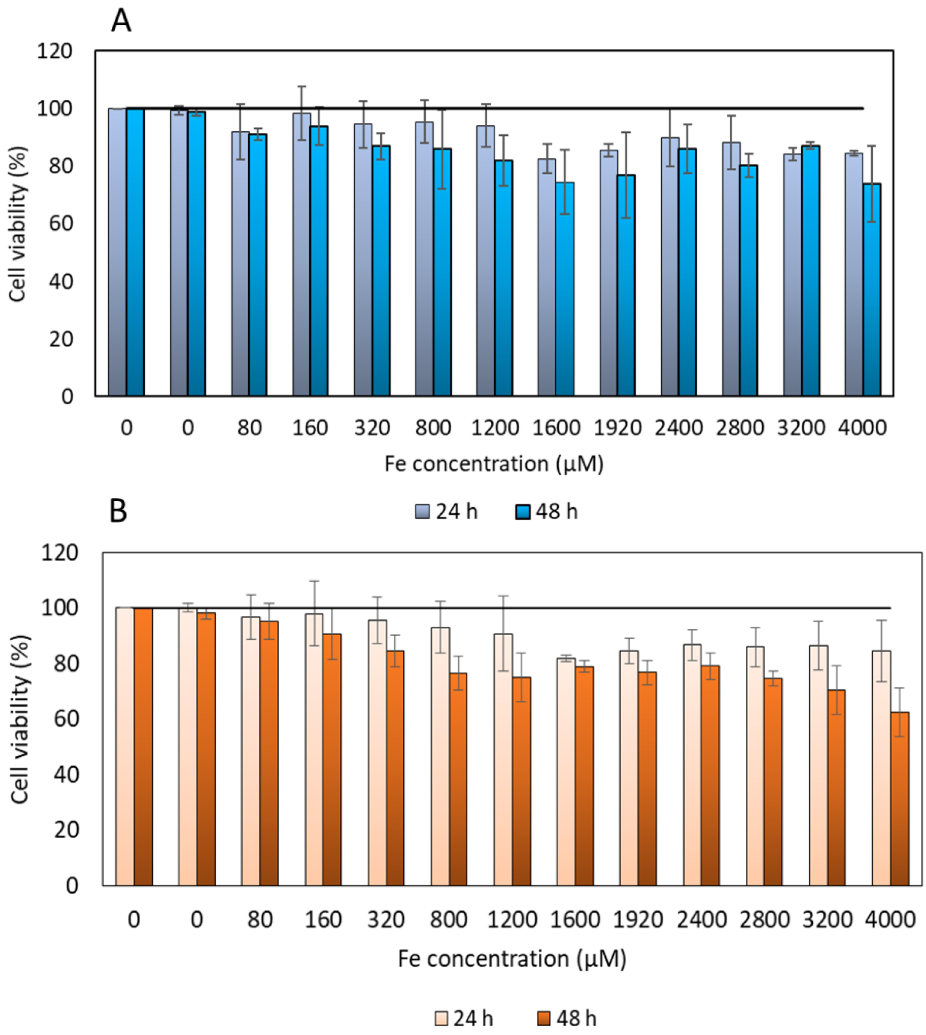


***Figure 43. Effect of FeNPs on the survival rate of THP-1 monocytes cells (A) and macrophages (B) after 24 h (light bars) and 48 h (dark bars) of incubation time.***

### *4.2.5.2. Oxidative stress evaluation: Reactive Oxygen Species assay*

Different mechanisms can cause toxicity in body, but most intracellular and in vivo toxicities from nanoparticles arise from the production of excess reactive oxygen species. High ROS levels are indicative of oxidative stress and can damage cells by peroxidising lipids, altering proteins, disrupting DNA, interfering with signalling functions, and modulating gene transcription and finally ending up in cancer, renal disease, neurodegeneration, cardiovascular or pulmonary disease [121].

As it can be seen in Figure 44, the cellular DCFDA assay revealed the evidence of reactive oxygen species generation with time after incubating with FeNPs and $FeSO_4$, which is in good agreement with the expected for iron compounds [130]. Fluorescence intensity increases with time in both cases and duplicates the background values from the compounds by themselves or cells without any modification. Thus, there is a proof of cell damage although it was not previously shown in terms of cell mortality.

It should be noticed that cellular oxidative stress might have a more pronounced impact when using $FeSO_4$ in comparison with the use of the same concentration of FeNPs, judging by the greater fluorescence intensity reached in the first case. This could be due to a lower bioavailability of the iron present in FeNPs as it is confined in the nanostructure and protected by its shell, minimizing its oxidant capability. These values are the result of applying a correction that considers the lower degree of absorption of the $FeSO_4$ compared to the FeNPs uptake. Concentration level of 0.25 mM was chosen attending to the plasma levels reached in patients after iron administration at pharmacological doses [250]. So, results here presented could validate the use of these nano-preparations for the effective treatment of iron deficiency disease.

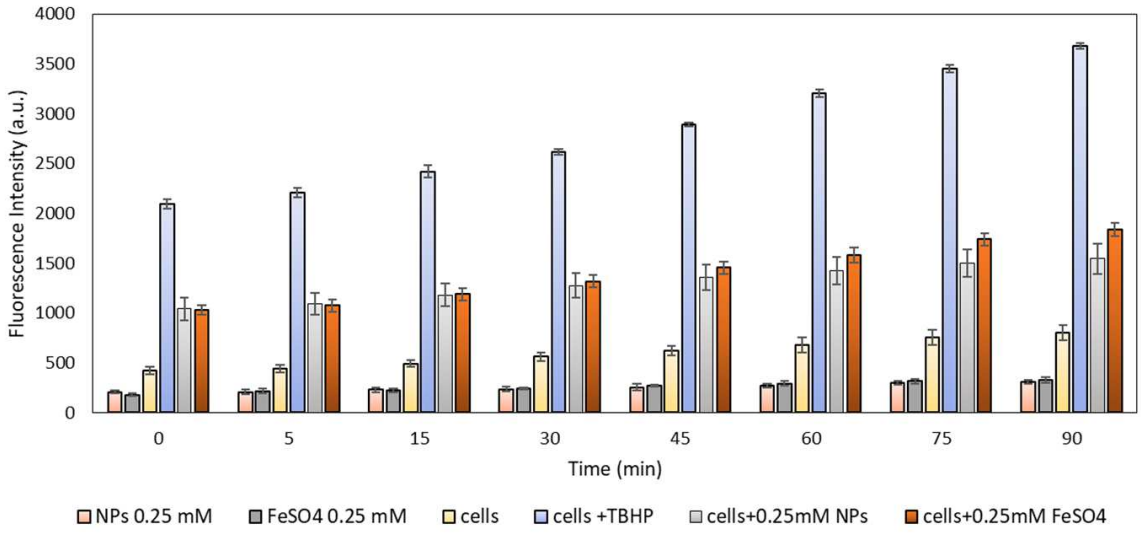


***Figure 44. ROS assay comparing the exposure to FeNPs (grey bars) Vs $FeSO_4$ (orange bars) in Caco-2. Tert-butyl hydroperoxide (TBHP) was used as positive control (blue bars) and controls of FeNPs (red bars), $FeSO_4$ (grey bars) and cells (yellow bars) were used to establish background levels of fluorescence intensity.***

### 4.2.6. Speciation and quantitative analysis of nanoparticles and ionic species of iron by HPLC-ICP-MS in combination with Isotope Dilution Analysis

#### *4.2.6.1. Optimization of HPLC conditions*

For the speciation goal, the methodology already designed for the separation of engineered silver containing nanoparticles and Ag(I) species in a single chromatographic run was modified to be applied for the speciation of iron nanoparticles and their ionic species, Fe(III). For these studies, a reversed-phase column with a pore size of 1000 Å and an ammonium acetate buffer containing SDS as modifier were used. Parameters used in this study are summarized in Table 23.

**Table 23. Instrumental parameters of the HPLC used for the speciation of Fe-NPs.**

| **HPLC** | |
|---|---|
| **Column** | Nucleosil 7 µm particle size, C18, 1000 Å pore size, 250 x 4.6 mm |
| **Flow rate** | 0.5 mL $min^{-1}$ |
| **Injection Volume** | 20 µL |
| **Mobile phase** | 10 mM SDS, 10 mM ammonium acetate, pH = 6.8 |

*Mobile phase studies*

First studies were carried out by diluting the self-synthesized iron nanoparticles in a solution of 10 mmol $L^{-1}$ SDS, 10 mmol $L^{-1}$ ammonium acetate, pH = 6.8 to final concentrations between 1 and 50 µg $L^{-1}$ of iron. Moreover, Venofer® solutions were also prepared in the same mobile phase to final concentrations between 1-30 µg $L^{-1}$. Figure 45 displays the variation of intensities in these chromatograms according to different iron concentrations injected for both complexes, Venofer® (Figure 45.A) and FeNPs (Figure 45.B).

Chromatograms also revealed an only peak at a retention time of 4.4 min in the case of Venofer® (used as a standard of 4.55 ± 0.55 nm), and 4.8 min for the self-synthesized FeNPs, in agreement with what we expected according to their smaller size (3.65 ± 0.39 nm) and the size exclusion mechanism followed in this kind of separation (Figure 46).

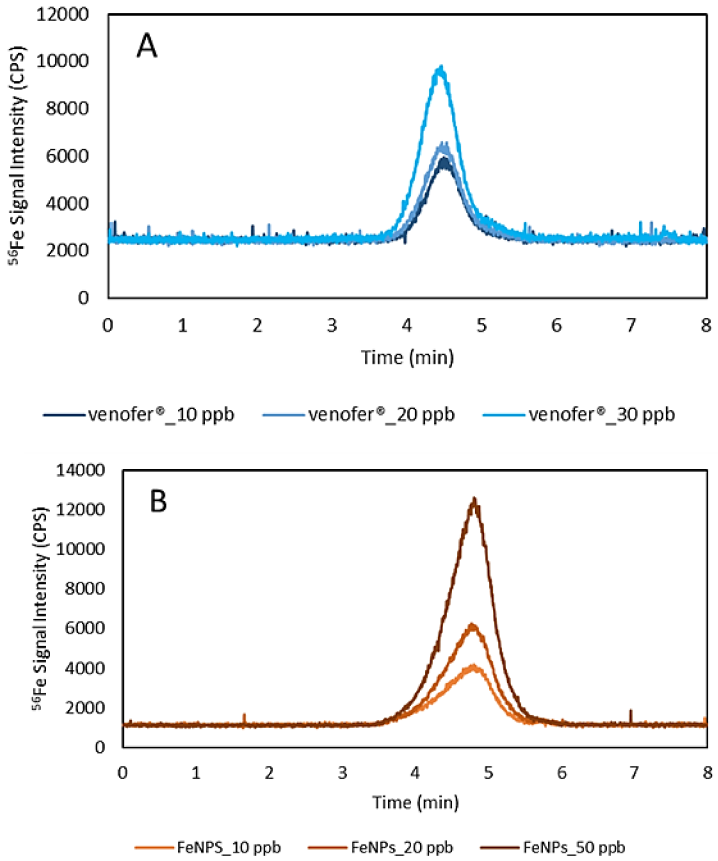


*Figure 45. Chromatograms of different concentration solutions containing Venofer® (A) and FeNPs (B)(solvent: 10 mM Ammonium acetate and 10 mM SDS).*

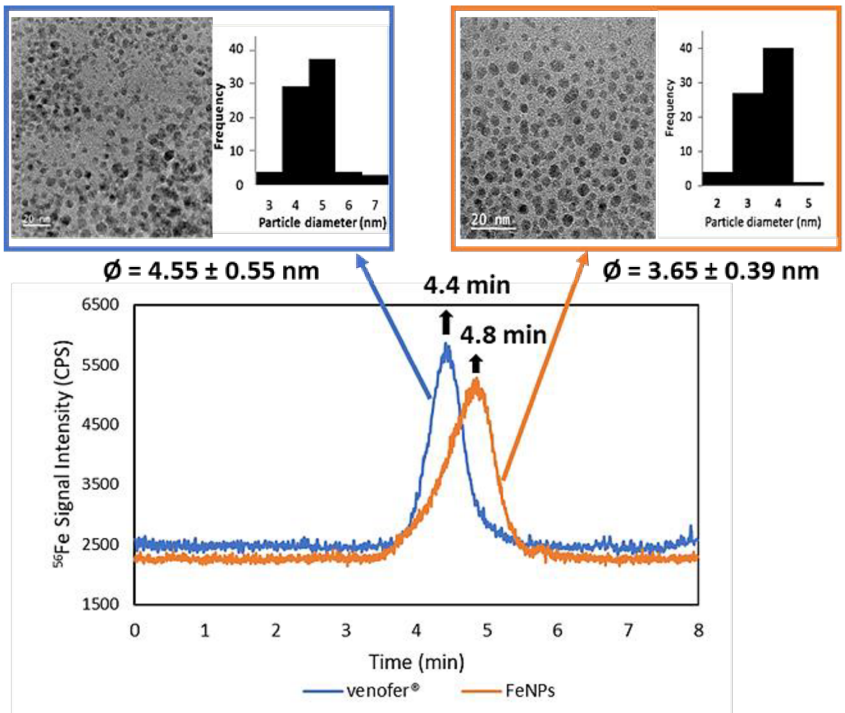


*Figure 46. Chromatograms and HR-TEM images of Venofer® and FeNPs.*

With the aim of eluting the iron ionic species, studies on the HPLC separation conditions were carried out. For this purpose, 1 mM EDTA and 1 mM sodium citrate were included for dilution of the samples. Both reagents are considered as iron high chelating agents (stability constants: Fe(III)-EDTA=25.7; Fe(III)-citric acid=11.85) so the soluble iron present in the samples is supposed to elute from the column chelated with these ligands. However, chromatograms show the appearance of two peaks, especially a high intensity signal at 5.7 min (Figure 47) that reveals the increasing solubilization of these nano-structures in these media with time and the high strength of these ligands in comparison to original binding of nanoparticles, especially in the case of EDTA, as expected regarding the stability constant (Figure 47.A).

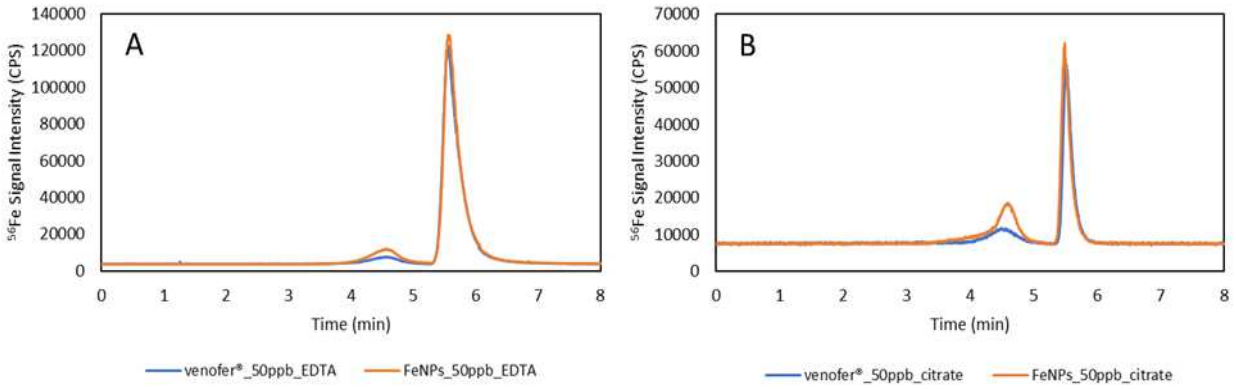


***Figure 47. Chromatograms of Venofer® and FeNPs using 1 mM EDTA (A) and 1 mM sodium citrate (B) as solvent agents.***

#### *4.2.6.2. Quantitative studies*

##### *4.2.6.2.1. Recovery studies for Venofer®, FeNPs and soluble species of iron*

To determine the recovery rates of the Venofer®, FeNPs and soluble iron, total iron quantification was measured as previously described in section 3.4.6.3. On the other hand, on-line quantification using the IDA approach was carried out. The application of post-column IDA, with an isotopically enriched $^{57}$Fe isotope standard, resulted in three peaks at retention times of 4.4 min, 4.8 min and 5.7 min for Venofer®, FeNPs and Fe(III), respectively. Concentration of iron was calculated according to Rottman et al. using the equation for time-resolved IDA [251]. Table 24. shows obtained recoveries for those species.

**Table 24. Total Fe concentration measured for Venofer®, FeNPs and Fe(III) and corresponding recoveries.**

| Sample | Determined Fe concentration by ICP-MS (µg $L^{-1}$) | Determined Fe concentration by IDA (µg $L^{-1}$) | Recoveries (%) |
|---|---|---|---|
| **Venofer®** | 12.2 | 11.4 ± 1.8 | 93.2 |
| **FeNPs** | 19.4 | 17.4 ± 1.0 | 89.9 |
| **Fe(III)** | 15.3 | 5.7 ± 0.1 | 37.5 |

Satisfactory recovery rates of 89.9 % and 93.2 % were obtained for FeNPs and Venofer®, whereas a value below 40 % was determined for soluble species. This can be attributed to a higher retention of these small ions in the column due to their strong interactions with the negatively charged sulphate groups from the SDS contained in the mobile phase and a consequent entrapment in the column. Repeatability in terms of retention time and peak area was assessed and collected in Table 25.

**Table 25. Repeatability in terms of retention times and peak areas for Venofer®, FeNPs and the ionic species of Fe and the LODs for the analyzed samples using the 1000 Å column (N = 3).**

| Sample | Retention time peak (min) | Peak Area (ng $min^{-1}$) | LOD (µg $L^{-1}$) |
|---|---|---|---|
| Venofer® | 4.44 ± 0.01 | 0.25 ± 0.05 | 1.65 |
| FeNPs | 4.80 ± 0.01 | 0.35 ± 0.02 | 0.53 |
| Fe(III) | 5.61 ± 0.01 | 0.11 ± 0.01 | 1.11 |

The suggested chromatographic strategy shows repeatable results by looking at the standard deviations values: 0.01 for retention times (N = 3) and below 0.05 for peak area (N=3). Lowest detection limit was achieved for the self-synthesized FeNPs (0.53 µg $L^{-1}$) whereas the highest was obtained for Venofer® nanoparticles with a value of 1.65 µg $L^{-1}$. There are no comparable results as there is no analogous strategy for the speciation and quantification of iron nanoparticles, especially in the low nm-range as these ones.

#### *4.2.6.2.2. Analysis of iron species in Caco-2 cell samples*

The protocol for the FeNPs extraction from cellular samples was followed as detailed in section 3.4.6.4. Purification steps based on sedimentation through sucrose cushion seem to be more effective in terms of detaching loosely bound proteins and isolating the nanoparticle,

without affecting its intrinsic structure. In parallel, acid digestion and iron total quantification of Caco-2 cell pellets containing the FeNPs were carried out by ICP-MS.

Once the cell extracts are injected in the column, separation in three peaks occurs as it is shown in Figure 48. A peak at 4.8 minutes that is only missing in the control sample and increases the intensity with increasing iron concentrations denotes the elution of NP-bound iron species, and so it was previously determined in aqueous solution studies (Figures 45.B and 46).

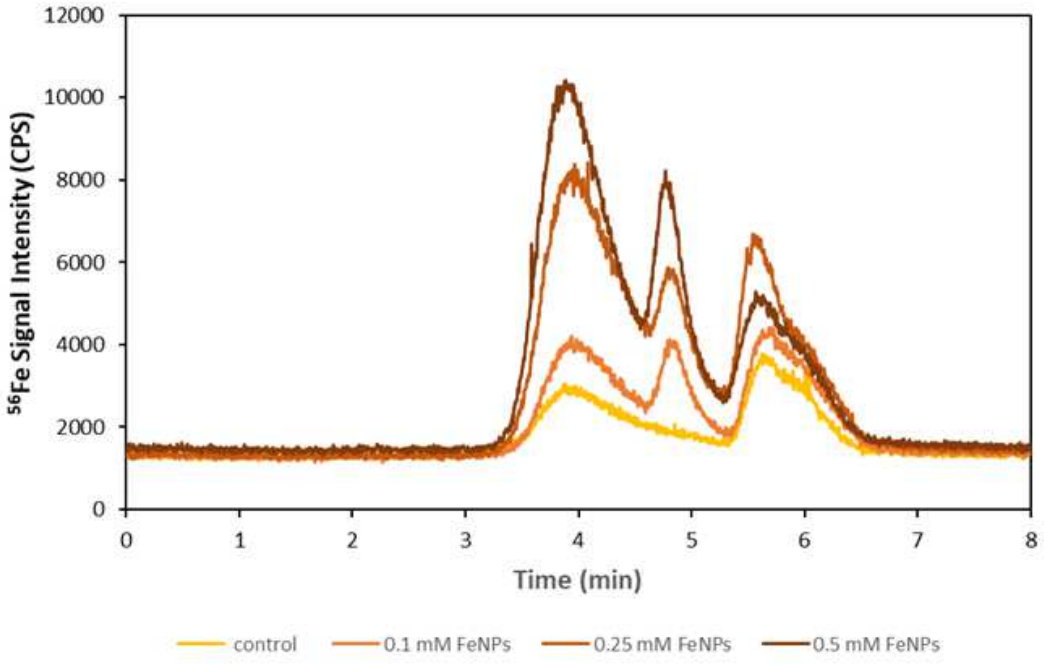


***Figure 48. Chromatograms of solutions extracted from Caco-2 cell samples containing 0, 0.1, 0.25 and 0.5 mM FeNPs.***

Another peak at 5.7 minutes tends to increase when iron content gets also higher in the samples. It can be correlated to ionic iron species based on the retention time obtained for Fe(III) in prior mobile phase studies (see Figure 47). This increment can be justified by the solubilization of the nanoparticles that takes place gradually when entering the cells. By using the nanoparticles whose sizes are well-known by complementary techniques, such as HR-TEM, it is possible to obtain a size calibration considering different retention times. Thus, a mean size of $1.62 \pm 0.03$ nm could be estimated for these soluble iron species.

Chromatograms also show another peak at a retention time of 3.7 min which needed further analysis for its identification. For this purpose, fractions between 3.2 and 4.2 min were collected at the exit of the column and examined by HR-TEM. At such a retention time, estimated particle size was $6.1 \pm 0.8$ nm and, in fact, images corresponding to these fractions verified this value.

Figure 49 reveals the presence of some polydisperse aggregates of nanoparticles with a mean diameter size of 5.84 ± 1.21 nm. This can be due to the small size of these nanoparticles and their tendency to aggregate, especially when surface coating is affected or there are some changes on the buffer solution where they are suspended.

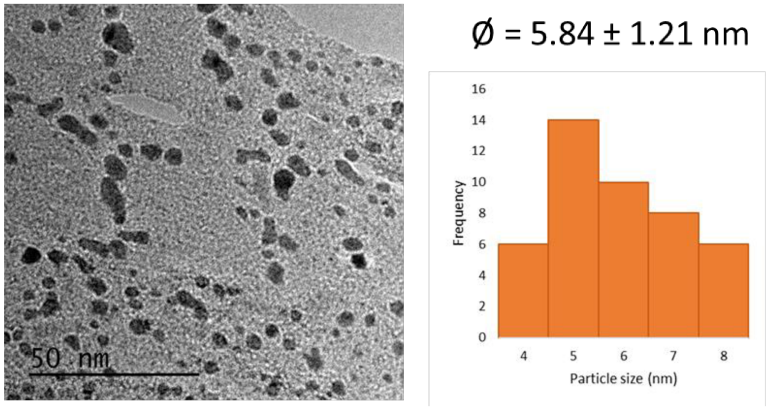


***Figure 49. HR-TEM image showing FeNP aggregates present in the collected fractions.***

However, this would not explain the presence of this peak in the control sample, where no FeNPs were added. In this case, ferritin protein and its ferrihydrite core plays an important role. It is possible that this protein remains in the sample even after applying the extraction protocol. Ferritin stores iron in a nanoparticle form that assemble into a hollow nano-sphere with an outer diameter of 12 nm and an inner diameter of about 8 nm [19]. It can be then correlated to the peak detected in the chromatogram of the control sample.

The quantitative recoveries obtained were satisfactory for all the cell extracts (60-80 %) and are collected in Table 26. However, it is remarkable how the sample containing the highest concentration of FeNPs (0.5 mM) apparently contains a fraction of ionic iron species smaller than the previous sample and thus, makes that total iron quantification does not increase as it would be expected. This can be associated to the also low recovery rate obtained for soluble iron species in comparison to FeNPs and Venofer® values in previous section and the possible and not always proportional entrapment of these species in the column previously mentioned.

**Table 26. Determined FeNP, ionic Fe and total Fe concentration for four injected sample concentrations of the FeNPs in Caco-2 extract samples.**

| Sample | Fe total concentration by ICPMS (µg $L^{-1}$) | Determined FeNP concentration (µg $L^{-1}$) | Determined $Fe^{3+}$ concentration (µg $L^{-1}$) | Fe total concentration (µg $L^{-1}$) | Recoveries (%) |
|---|---|---|---|---|---|
| **Control** | 7.9 | - | 2.7 ± 0.1 | 5.6 ± 0.2 | 70.6 |
| **0.1 mM FeNPs** | 318.1 | 73.7 ± 3.8 | 89.2 ± 5.1 | 250.8 ± 42.8 | 78.8 |
| **0.25 mM FeNPs** | 687.3 | 88.6 ± 3.3 | 149.4 ± 13.1 | 503.2 ± 25.2 | 73.2 |
| **0.5 mM FeNPs** | 995.3 | 161.4 ± 21.4 | 148.3 ± 12.8 | 590.7 ± 28.9 | 59.3 |

## 4.3. *In vivo* studies on iron nanoparticles for the oral treatment of anaemia: distribution and bioaccumulation assessment in rats

Iron absorption takes place at the apical membrane of duodenal enterocytes. Usually, *in vitro* studies are made to address drug absorption. However, true absorption of ingested trace metals is defined as the uptake and transfer of dietary mineral across the mucosal cells [252]. In this sense, small intestine perfusion experiments seem to be particularly adequate to study metallodrugs absorption in animal models [230, 253].

### 4.3.1. Acid lability assays to check the stability of FeNPs in gastric conditions

Usually, one of the most important aspects to determine the bioavailability of an iron supplement is the solubility that it presents when passing through the gastrointestinal barrier. Thus, it is important to check the stability of the self-synthesized iron nanoparticles in this sort of media, which is quite far from the pH values of the original medium. For this purpose, acid lability assays were performed following protocol already detailed in Experimental Section (3.4.5.2.).

With this experiment, FeNPs were checked in a simulated digestion medium with time and results are shown in Figure 50. In brief, three different degrees of solubilization are detected. During the first 5 minutes, the main solubilization occurs (soluble fraction increases from 12 to 33 %), duplicating the soluble fraction from the initial point. During the next 5 minutes, another important solubilization takes place but not as significant as the first one (soluble fraction increases from 33 to 46 %). Finally, a balance between both species (nanoparticulate and soluble fractions) is reached, and the situation remains until the end of the experiment (95 minutes),

confirming the stability of these nanostructures in the gastric tract. This fact is in agreement with the bibliography consulted [55].

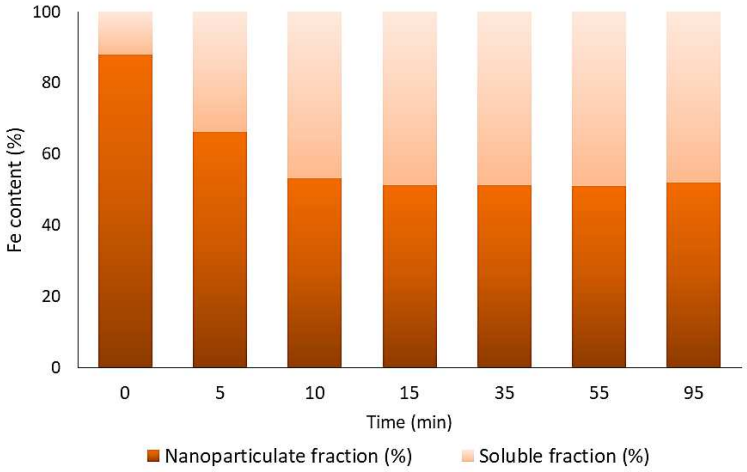


***Figure 50. Acid lability assay of FeNPs at pH 3 showing the evolution of the nano-compound composition with time (nanoparticulate fraction is showed as dark orange bars; soluble fraction is represented as light orange bars.)***

### 4.3.2. Iron absorption and distribution through the small intestine

Iron absorption studies by intestinal perfusion of FeNPs suspensions were accomplished for the first time in anaesthetized animals. For this purpose, the animals were treated as described in the Experimental section (3.4.7.1.) and the total iron was measured by ICP-MS after adequate dilution and using $H_2$ as cell gas in the infused solution before and after perfusion. The obtained results (before and after normalization by the dimensions of the intestine of the different animals) are shown in Table 27.

**Table 27. Results obtained for the perfusion experiments.**

| Compound | Number | Perfused Fe (mg $L^{-1}$) | Absorbed Fe (mg $L^{-1}$) | % Absorption | Absorption by intestinal surface (V at mg $L^{-1}$ $cm^{-2}$) |
|---|---|---|---|---|---|
| **Control** | 4 | 0.004 ± 0.003 | -0.2 ± 0.1 | - | -0.006 ± 0.001 |
| **FeNPs** | 4 | 35.6 ± 0.6 | 28.2 ± 2.1 | 79.3 ± 6.1 | 0.3 ± 0.1 |

As can be observed, the absorption of the FeNPs achieves a value of 79.3 % compared to the control group, that proves the effectiveness of potential absorption that these nanoparticles

would have if they were orally administered. The absorption rate of iron from FeNPs is significantly higher than the one commonly obtained in the literature (from 1-50 % depending on specific conditions [254, 255]). In particular, in previous bioavailability studies using $FeSO_4$, absorption values between 26-57 % were obtained [256, 257].

It is known that iron absorption normally occurs in the duodenum and upper part of the jejunum. However, it is important to remark that the availability of ingested iron for absorption can vary and the amount absorbed depends on the chemical nature and quantity of iron in the diet, the presence of other factors in ingested food, the effects of gastrointestinal secretions and the absorptive capacity of the intestinal mucosa [254, 255]. Moreover, in a similar study for iron absorption assessment by duodenum perfusion using ferric citrate, uptake levels of 30 % were obtained [258], being clearly lower than the values here presented.

This great absorption value can be attributed to the higher capacity of FeNPs absorption due to the several uptake mechanisms that can take place in in vivo models. The ionic fraction released from nanoparticles may be absorbed by DMT-1 protein, whereas the non-digested FeNPs could be uptaken by endocytosis and released to the interstitial space, increasing the yield of the absorptive process. It has also been described that alternatively, macromolecules may cross the "tight junction" barrier between cells and diffuse into the intercellular space, so they can be absorbed by paracellular pathways. In both cases, FeNPs would access to the portal veins via mesenteric lymph [259]. The participation of both mechanisms would allow to increase iron intestinal absorption capacity. Furthermore, this hypothesis would be supported by the presence of FeNPs in blood and spleen of the perfused rats that will be presented in following section (Figure 54 A, B) and this would justify the existence of the absorption mechanisms previously discussed.

By conducting this perfusion experiment, the distribution and accumulation of iron throughout the three regions (duodenum, jejunum and ileum) of the small intestine were also evaluated. Tissues were lyophilized, and microwave-assisted digestion was carried out as it was described in the previous section. Then, corresponding dilutions were made in order to measure total iron concentration by ICP-MS, using $H_2$ as collision gas to remove polyatomic interferences affecting the $^{56}Fe$ monitorization.

Figure 51 shows the total iron concentration in duodenum, jejunum and ileum after perfusing a saline solution in the case of the control group, and FeNP solutions in the target group.

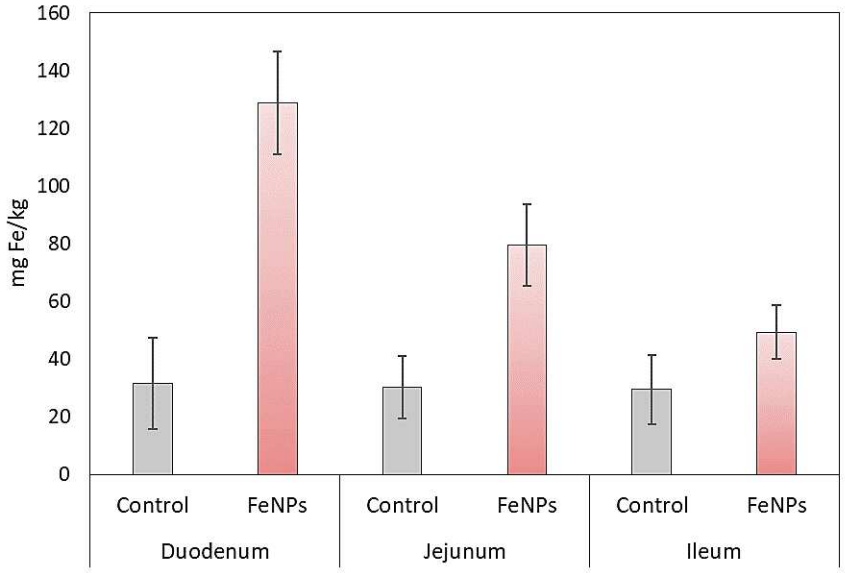


***Figure 51. Total Fe concentration levels in duodenum, jejunum and ileum after FeNPs perfusion (red bars, N = 4) and comparison with control samples (grey bars, N = 4).***

As can be seen in the graph, an equal accumulation of iron in the three regions is obtained for control samples (concentrations are between 32 ± 16 mg $kg^{-1}$ in the duodenum and 29 ± 12 mg $kg^{-1}$ in the ileum), while a clear pattern of decreasing iron concentration is observed throughout the three regions of the small intestine where the FeNPs were perfused. The determining role of duodenum in the absorption of iron is here evident and in agreement with what it was expected according to literature [258]. Moreover, the iron content incorporated to the small intestine by injecting FeNPs solutions is significantly present in the three parts and means an important increment of 300 %, 163 % and 67 % over control duodenum, jejunum and ileum samples, respectively. These results are in good agreement with previous comments (section 3.2) about DMT-1 transporter in different regions through the small intestine and their absorption capability [260].

### 4.3.3. Small intestine perfusion experiment using $^{57}$FeNPs

Parallel experiments were carried out in small intestine of 4 rats using isotopically labelled $^{57}$FeNPs. Table 28 shows the total iron absorption before and after normalization by the dimensions of the intestine of the different animals and the comparison between values obtained in both kind of FeNPs employed as well as the difference with the control samples.

**Table 28. Results obtained after perfusion experiments (including $^{57}$FeNPs).**

| Compound | Number | Perfused Fe (mg $L^{-1}$) | Absorbed Fe (mg $L^{-1}$) | % Absorption | Absorption by intestinal surface (V at mg $L^{-1}$ $cm^{-2}$) |
|---|---|---|---|---|---|
| **Control** | 4 | 0.004 ± 0.003 | -0.2 ± 0.1 | - | -0.006 ± 0.001 |
| **FeNPs** | 4 | 35.6 ± 0.6 | 28.2 ± 2.1 | 79.3 ± 6.1 | 0.3 ± 0.1 |
| **$^{57}$FeNPs** | 3 | 16.9 ± 0.4 | 13.3 ± 1.0 | 78.3 ± 5.4 | 0.2 ± 0.1 |

As it was previously shown in case of FeNPs perfusion, Figure 52 shows the total iron concentration in duodenum, jejunum and ileum after perfusing a saline solution in the case of the control group, and $^{57}$FeNP solutions in the target group.

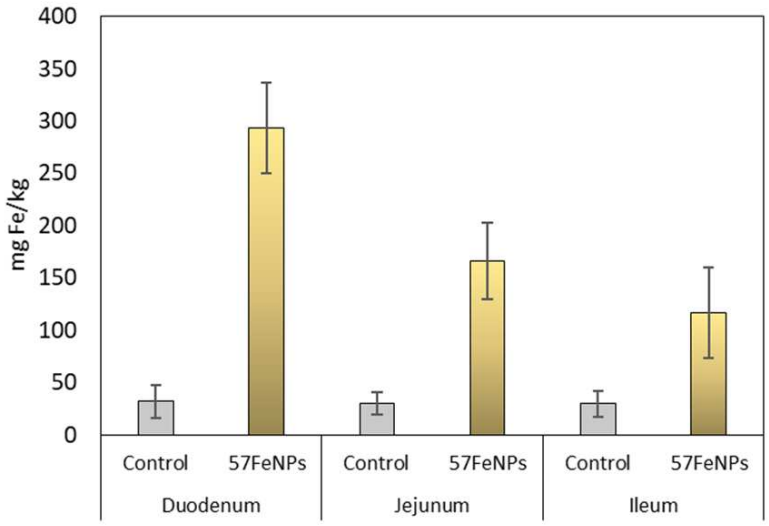


***Figure 52. Total Fe concentration levels in duodenum, jejunum and ileum after $^{57}$FeNPs perfusion (yellow bars, N = 4) and comparison with control samples (grey bars, N = 4).***

Iron absorption pattern is in agreement with the one detected in previous experiment with FeNPs, with a prevailing role of duodenum in comparison to the other small intestine parts. However, main differences are founded in the high levels of total concentration detected in all intestine regions (duodenum, jejunum and ileum) being almost 2 times higher when using $^{57}$FeNPs for the perfusion experiment.

### 4.3.4. Iron distribution in other tissues

As a first step to address the fate of FeNPs once they are absorbed in the small intestine, reaching the bloodstream, samples from other tissues that could be involved in the iron metabolism were collected and treated as the intestine fragments. Figure 53 displays the total iron quantification in kidney, liver and blood samples after intestinal perfusion experiment with and without FeNPs and quantitative results of total iron measurements after perfusion experiments were summarized and collected in Table 29.

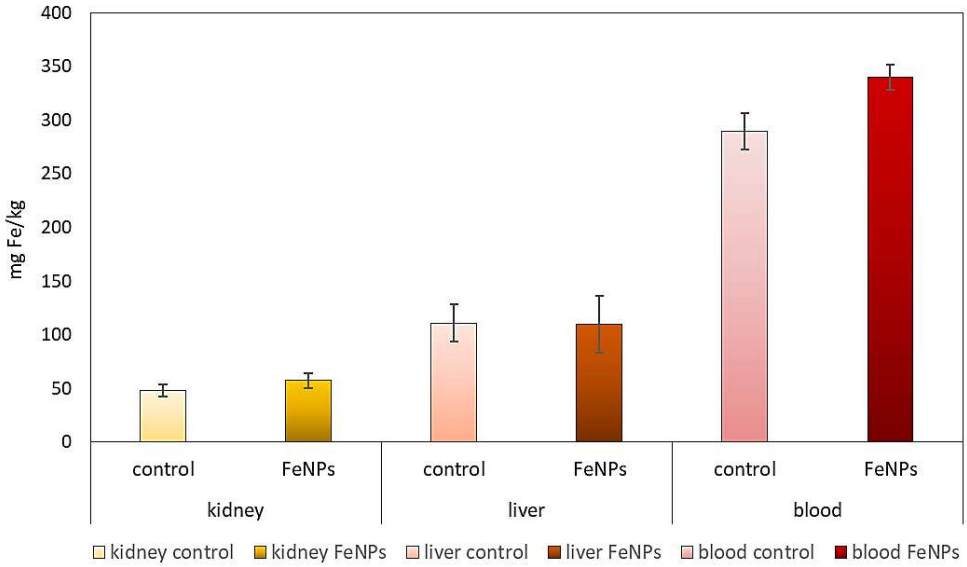


***Figure 53. Fe content in other tissues after intestinal perfusion of FeNPs (dark bars) and saline solutions without iron (light bars).***

**Table 29. Iron content in small intestine and other tissues after FeNPs perfusion and iron increment compared to control samples.**

| | Total iron content in control samples (mg $kg^{-1}$) | Total iron content in FeNPs-perfused samples (mg $kg^{-1}$) | Increment of iron (%) |
|---|---|---|---|
| **Duodenum** | 31.7 ± 15.8 | 128.9 ± 17.7 | 300 |
| **Jejunum** | 30.2 ± 10.9 | 79.7 ± 14.2 | 163 |
| **Ileum** | 29.5 ± 12.0 | 49.4 ± 9.4 | 67 |
| **Kidney** | 47.9 ± 5.4 | 57.3 ± 7.1 | 20 |
| **Liver** | 110.8 ± 17.2 | 109.7 ± 26.6 | -1 |
| **Blood** | 289.3 ± 17.1 | 340.1 ± 11.4 | 18 |

The obtained results in kidney and blood reveals an increment of 20 and 18 %, respectively in comparison to their corresponding control samples. In contrast to this trend, liver samples remain stable and no significant variation is found in terms of iron concentration after FeNPs injection. This is in good agreement with the expected results for these small size nanoparticles which are generally renally cleared from blood [261]. This could justify the barely perceptible effect of the FeNPs in this tissue looking at total iron analysis by ICP-MS. As it has been mentioned, Fe concentration increases in blood and kidney. FeNPs, previously absorbed in the intestine, would be incorporated into bloodstream for further distribution to other tissues. At the renal level, both free iron species and FeNPs, would filter easily into the glomeruli and become part of the renal tubules content.

Some of the tissues, as the spleen and blood, were also fixated as previously mentioned, and TEM images were taken to determine subcellular location and a possible degradation of FeNPs. Figure 54.A shows the presence of a large number of FeNPs in the bloodstream without any significant structure modification. In Figure 54.B a fragment of a spleen macrophage is shown.

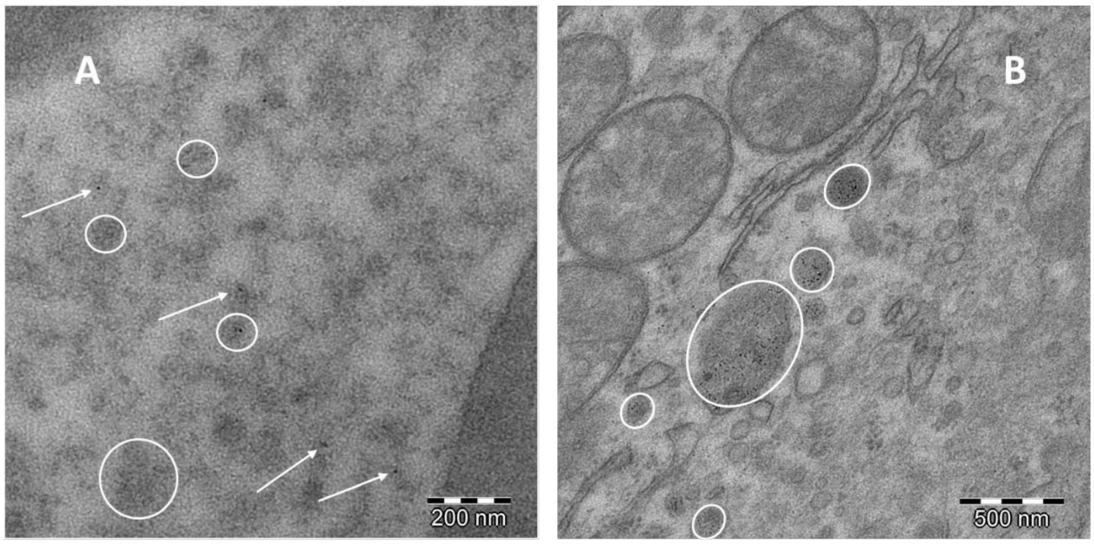


***Figure 54. TEM images after FeNPs perfusion in blood (A) and macrophages from spleen (B).***

The FeNPs are found in digestive vacuoles where they are isolated to be destroyed by fusion with the lysosomes and release of the enzymes containing inside them. The presence of FeNPs in the spleen could be a consequence of the high degree of vascularization of this tissue, which would allow the fast arrival of NPs, and the high presence of macrophages with great capacity to phagocytose and incorporate these nanostructures [262].

Al together these studies and results could confirm a high stability of the nanoparticle structure, a rapid metabolization of the FeNPs in the body and also a fast incorporation into bloodstream, in the light of the results of the total iron measurements as well as TEM images.

# 5 CONCLUSIONS AND OUTLOOK

# 5 CONCLUSIONS AND OUTLOOK

The main conclusions that can be extracted from the present dissertation can be summarized in the following paragraphs.

Concerning the full characterization and bioavailability studies of a commercial preparation for the parenteral treatment of severe anaemia (Venofer®), it can be emphasized that:

- The physicochemical characterization of iron-sucrose nanoparticle formulation, Venofer®, revealed a monodisperse iron-NPs preparation of 4.55 ± 0.55 nm and an average hydrodynamic diameter of 15.11 nm.

- Solubilization studies in serum and blood samples were carried out by Isotope Dilution Analysis (IDA) with the addition of a stable tracer ($^{57}$Fe) and application of the IDA equation. It was revealed that a high concentration of iron is directly dissolved from the preparation in the presence of biological media after 7 hours of incubation, reaching 70 % of the initial iron concentration. Such results confirmed the semi-robust (kinetically) and moderately strong (thermodynamically) character of Venofer® formulation, probably due to the relatively labile nature of iron oxide-sucrose binding.

- The released iron incorporation into transferrin binding sites was addressed by separation of Tf sialoforms using anion exchange chromatography coupled to ICP-MS detection. Complete saturation was accomplished by adding $^{57}$Fe and application of isotope pattern deconvolution showed the contribution of endogenous and exogenous iron to each Tf isoform obtained. It was detected that complete iron saturation is not achieved even after 7 h of incubation, when the incorporation of iron to Tf-binding sites reached almost 95 %.

- Iron association to other serum proteins was evaluated by anion exchange chromatography coupled to UV and ICP-MS detection. Small iron traces were detected in the ICP-MS trace corresponding to albumin retention time. However, no other proteins seem to carry much iron from the disrupted particles. Thus, it can be concluded that part of the nanostructure might be disrupted into smaller size particles and ions that will circulate in the blood stream.

- The method here developed gives new insights for the monitoring of ions released from nanoparticles in body fluids and it can be considered as a competitive tool, especially in terms of accuracy and precision for the quantitative speciation of these iron species. Moreover, it can be considered as a suitable alternative to investigate the iron metabolism in other similar intravenous preparations for the treatment of anaemia.

From the synthesis of FeNPs suitable for the oral treatment of anaemia, it can be extracted that:

- A synthesis of non-aggregated FeNPs potentially used as iron supplements was carried out with satisfactory results in terms of monodispersity, reproducibility, and simplicity.

- Physico-chemical characterization by HR-TEM and DLS revealed a particle diameter of $3.65 \pm 0.39$ nm and a hydrodynamic volume of 11.77 nm, respectively. SAXS and WAXS measurements could show the non-total crystalline structure of the nanoparticles, although the 2-line ferrihydrite structure expected was not discarded by the results obtained. Moreover, nanoparticle structure stability in acidic medium was assessed by adding HCl, simulating gastric conditions and nanostructure remained stable during the whole experiment.

Regarding the *in vitro* studies developed in different cell lines, it should be highlighted that:

- Cellular uptake was evaluated by incubation of HT-29 and Caco-2 cell lines with different concentrations of FeNPs during 48 h and consequently, digestion and quantification by total iron analysis using ICP-MS. It was significantly higher in Caco-2 cells than in HT-29, although in both, the absorption of FeNP was clearly detected.

- Cell samples were fixated and prepared for TEM imaging in order to get information about subcellular location. TEM images suggested an endocytic pathway of FeNPs to enter the cells and a subsequent confinement in vesicles for further release and distribution to other tissues in the body.

- Toxicity was also evaluated. Cell viability assays displayed a non-harmful effect of these nanoparticles in the range of therapeutic levels (up to 4 mM Fe concentration) after 48 h of exposure in different cell lines (THP-1, macrophages, HT-29, and Caco-2). ROS experiments detected an increment of fluorescence intensity in cells incubated with FeNPs, but the oxidative stress effect caused by the FeNPs is lower than the $FeSO_4$ at the

same concentration level. Thus, it is a significant improvement in the oral treatments supplied up to now.

The main conclusions concerning the speciation and quantification of iron nanoparticles and soluble iron species by reversed phase chromatography coupled to ICP-MS can be summarized as follows:

- Chromatography separation of different size nanoparticles and corresponding ions was optimized and satisfactorily applied to different iron compounds: Venofer®, self-synthesized FeNPs, and Fe(III) salts. The methodology here developed improved the range of size in the separation that was assumed for this type of reversed-phase column, allowing the separation of two iron nanostructures (below 5 nm diameter size) differing in only 1 nm between them.

- Caco-2 cells were incubated with three different concentrations of FeNPs and extraction of nanoparticles from the cell matrix was carried out before injecting on the chromatographic column. Separation of three different iron species in the range of 1.6 to 6.1 nm was detected in less than 7 minutes in one single run. Nanoparticle fraction was clearly detected by comparison with the blank samples (without FeNPs incubation).

- Simultaneous quantification of all iron species was achieved by using post-column isotope dilution analysis and recoveries between 90-93 % and between 60-80 % were obtained for nanoparticles aqueous solutions and cell extracts, respectively. Moreover, repeatability values and limits of detection in the low µg $L^{-1}$ range make this methodology suitable for the speciation of iron species in biological samples and mean a significant enhancement considering there are no comparable studies neither for iron nanoparticles nor for such small size nanoparticles.

Regarding *in vivo* studies, following conclusions must be remarked:

- Small intestine perfusion was carried out for the first time with this kind of FeNPs and absorption degree of approximately 80 % was observed after 100 minutes of experiment, proving the effectiveness of the FeNPs and the capability of these perfusion experiments to mimic the real absorption that would take place after oral uptake. Moreover, the important role of duodenum in the iron absorption was shown with significant differences over jejunum and ileum.

- In order to assess the pathway of the FeNPs after being absorbed in the small intestine, other tissues such as liver, kidney, blood and spleen were also digested and analysed by ICP-MS. FeNPs showed a possible clearance via kidney as there was no variation found on liver tissues before and after FeNPs perfusion.

- The release of nanoparticles to bloodstream without any degradation was also proven to be fast as they were already found in blood samples examined by TEM.

Although the different aims of this dissertation have been described and achieved in the light of the conclusions, the nature of scientific research leads to new challenges that can be investigated in the future. Here, some remaining questions are raised:

- As it was mentioned, there are several parenteral preparations in the market for the treatment of anaemia based on iron-carbohydrate nanoparticles suspensions. However, release and behaviour of these iron compounds in the blood stream and their interaction with proteins are still issues to be cleared. Thus, analytical strategies here proposed and successfully applied to Venofer® could be also applied to other similar preparations and comparison in terms of solubilization, bond lability or association to iron binding proteins would be established.

- Speciation of FeNPs and ionic species of iron was here achieved by using reversed phase chromatography coupled to ICP-MS. This methodology was applied to aqueous suspensions and Caco-2 cells samples with satisfactory quantitative recoveries. Therefore, similar strategy might be carried out in more complex biological samples, such as organ tissues or *in vivo* experiments, so the stability and solubilization of the nanoparticle were assessed and toxicological effects or metabolic disorders could be better understood.

- Syntheses of different “labelled” FeNPs were here developed, using lanthanides as Holmium, and isotopic enriched standards as $^{57}Fe$. This leads to multiple possibilities in detection and quantification by mass spectrometric techniques which were not tackled here. For example, LA-ICP-MS approach could be achieved with higher sensitivity and avoiding polyatomic interferences that usually affect $^{56}Fe$ detection.

# 6 GLOSSARY

# 6 GLOSSARY

| | |
|---|---|
| ACD | Anaemia of chronic disease |
| AF4 | Asymmetric flow field flow fractionation |
| AFM | Atomic force microscopy |
| ATP | Adenosine triphosphate |
| BSA | Bovine serum albumin |
| Calcein AM | Calcein acetoxymethyl |
| CE | Capillary electrophoresis |
| CMC | Critical micellar concentration |
| CRC | Collision/Reaction cell |
| CRP | C-reactive protein |
| DAD | Diode array detector |
| DCF | 2'-7'dichlorofluorescein |
| DCFH-DA | 2'-7'dichlorofluorescin diacetate |
| DLS | Dynamic light scattering |
| DMT1 | Divalent Metal Transporter 1 |
| DNA | Deoxyribonucleic acid |
| EDTA | Ethylenediaminetetraacetic acid |
| EDX | Energy dispersive X-ray analysis |
| EM | Electron microscopy |
| ESA | Erythropoiesis-stimulating agents |
| FBS | Fetal bovine serum |
| FFF | Field flow fractionation |
| GE | Gel electrophoresis |
| GSH | Glutathione redox system |
| Hb | Haemoglobin |
| HCP1 | Haem carrier protein 1 |
| HDC | Hydrodynamic chromatography |
| HEPES | 4-(2-hydroxyethyl)-1-piperazineethanesulfonic acid |
| HFE | Human hemochromatosis protein |
| HPLC | High performance liquid chromatography |
| HR-TEM | High resolution transmission electron microscopy |
| IC | Ion exchange chromatography |
| ICP-ORS-MS | ICP-MS with octapole reaction system |
| IDA | Iron deficiency anaemia |
| | Isotope dilution analysis |
| IPD | Isotope pattern deconvolution |
| LA-ICP-MS | Laser ablation coupled to ICP-MS |
| LDH | Lactate dehydrogenase |
| MALLS | Multiangle laser light scattering |
| MALS | Multiangle light scattering |
| MDA | Malondialdehyde |
| MEKC | Micellar electrokinetic chromatography |
| MEM | Minimum essential medium |
| MIC | Minimum inhibitory concentration |
| MTT | 3-(4,5-dimethylthiazol-2-yl)-2,5-diphenyltetrazolium bromide |

| | |
|---|---|
| NADPH | Nicotinamide adenine dinucleotide phosphate |
| PBS | Phosphate buffer saline |
| PLGA | Poly(lactic-co-glycolic acid) |
| PLGA-PEG | Polyethylene glycol–poly lactic acid-co-glycolic acid |
| PMA | Phorbol 12-myristate 13-acetate |
| RES | Reticuloendothelial system |
| ROS | Reactive oxygen species |
| RP-HPLC | Reversed phase high performance liquid chromatography |
| RPMI | Roswell Park Memorial Institute cellular medium |
| SAXS | Small-angle X-ray scattering |
| SDS | Sodium dodecyl sulphate |
| SEC | Size exclusion chromatography |
| SEM | Scanning electron microscopy |
| spICP-MS | Single particle detection |
| sTfR | Serum transferrin receptor |
| TBHP | Tert-butyl hydroperoxide |
| TEM | Transmission electron microscopy |
| Tf | Transferrin |
| TIBC | Total iron-binding capacity |
| TRIS | Tris(hydroxymethyl)aminomethan |
| UIBC | Unsaturated iron-binding capacity |
| WAXS | Wide-angle X-ray scattering |
| WST | 2-(4-Iodophenyl)-3-(4-nitrophenyl)-5-(2,4-disulfophenyl)-2H tetrazolium, monosodium salt |
| XRD | X-ray difraction |

# 7 BIBLIOGRAPHY

# 7 BIBLIOGRAPHY


1. de Laeter JR, Böhlke JK, De Bièvre P, Hidaka H, Peiser HS, Rosman KJR, Taylor PDP (2003) Atomic weights of the elements. Review 2000 (IUPAC Technical Report). Pure Appl Chem 75:683–800.

2. Pérez Surribas D (2005) Proteínas relacionadas con el metabolismo del hierro. Química Clínica 24:5–40.

3. Kaplan J, DM W (2013) The essential nature of iron usage and regulation. Curr Biol 23:R642-6.

4. Gurzau ES, Neagu C, Gurzau AE (2003) Essential metals - Case study on iron. Ecotoxicol Environ Saf 56:190–200.

5. Rout GR, Sahoo S (2015) Role of Iron in Plant Growth and Metabolism. Rev Agric Sci. 3:1-24.

6. Berg JM, Tymoczko JL, Stryer L (2002) Biochemistry, Fifth Edition. W.H. Freeman

7. Harrison PM, Arosio P (1996) The ferritins: Molecular properties, iron storage function and cellular regulation. Biochim Biophys Acta - Bioenerg 1275:161–203.

8. Brock JH (1994) Iron Metabolism in Health and Disease. Saunders

9. Bermejo F, García-López S (2009) A guide to diagnosis of iron deficiency and iron deficiency anemia in digestive diseases. World J Gastroenterol 15:4638–4643.

10. Allowances NRC (US) S on the TE of the RD (1989) Recommended Dietary Allowances. Recomm Diet Allow 10th Ed.

11. Abbaspour N, Hurrell R, Kelishadi R (2014) Review on iron and its importance for human health. J Res Med Sci 19:164–174.

12. Jacobs A, Miles PM (1969) Role of gastric secretion in iron absorption. Gut 10:226–229.

13. Ponka P, Schulman HM, Woodworth RC, Richter GW (1990) Iron Transport and Storage. Taylor & Francis

14. Lynch SR, Cook JD (1980) Interaction of vitamin c and iron. Ann N Y Acad Sci 355:32–44.

15. Aisen P, Wessling-Resnick M, Leibold EA (1999) Iron metabolism. Curr Opin Chem Biol

3:200–206.

16. Uzel C, Conrad ME (1998) Absorption of heme iron. Semin Hematol 35:27–34.

17. Hagar W, Theil EC, Vichinsky EP (2002) Diseases of iron metabolism. Pediatr Clin North Am 49:893—909.

18. Swinkels DW, Janssen MCH, Bergmans J, Marx JJM (2006) Hereditary hemochromatosis: genetic complexity and new diagnostic approaches. Clin Chem 52:950–968.

19. Bode S a, Minten IJ, Nolte RJM, Cornelissen JJLM (2011) Reactions inside nanoscale protein cages. Nanoscale 3:2376–89.

20. Fischbach FA, Gregory DW, Harrison PM, Hoy TG, Williams JM (1971) On the structure of hemosiderin and its relationship to ferritin. J Ultrasructure Res 37:495–503.

21. Muñoz M, García-Erce JA, Remacha AF (2011) Disorders of iron metabolism. Part 1: molecular basis of iron homoeostasis. J Clin Pathol 64:281–6.

22. Wallace DF (2016) The Regulation of Iron Absorption and Homeostasis. Clin Biochem Rev 37:51–62.

23. Ganz T (2005) Cellular iron: Ferroportin is the only way out. Cell Metab 1:155–157.

24. Park CH, Valore E V, Waring AJ, Ganz T (2001) Hepcidin, a urinary antimicrobial peptide synthesized in the liver. J Biol Chem 276:7806–7810.

25. Nemeth E, Tuttle MS, Powelson J, Vaughn MB, Donovan A, Ward DM, Ganz T, Kaplan J (2004) Hepcidin regulates cellular iron efflux by binding to ferroportin and inducing its internalization. Science 306:2090–2093.

26. Piperno A (1998) Classification and diagnosis of iron overload. Haematologica 83:447–455.

27. Muñoz M, García-Erce JA, Remacha ÁF (2011) Disorders of iron metabolism. Part II: iron deficiency and iron overload. J Clin Pathol 64:287–96.

28. Piperno A, Mariani R, Trombini P, Girelli D (2009) Hepcidin modulation in human diseases: From research to clinic. World J Gastroenterol 15:538–551.

29. Castagna A, Campostrini N, Zaninotto F, Girelli D (2010) Hepcidin assay in serum by SELDI-TOF-MS and other approaches. J Proteomics 73:527–536.

30. Yun S, Vincelette ND (2015) Update on iron metabolism and molecular perspective of

common genetic and acquired disorder, hemochromatosis. Crit Rev Oncol Hematol 95:12–25.

31. Camaschella C, Nai A (2016) Ineffective erythropoiesis and regulation of iron status in iron loading anaemias. Br J Haematol 172:512–523.

32. Crichton RR, Ward RJ, Hider RC (2016) Metal Chelation in Medicine. Royal Society of Chemistry

33. WHO (2012) Priorities in the Assessment of Vitamin A and Iron Status in Populations, Panama City, Panama 15-17 September 2010. 1–86.

34. Office of Dietary Supplements (ODS) (2016) Iron Dietary Supplement Fact Sheet. In: Natl. Institutes Heal. https://ods.od.nih.gov/factsheets/Iron-HealthProfessional/#en8. Accessed 24 Jan 2018

35. Kaur S (2016) Iron Deficiency Anemia ( IDA ): A Review. Int J Sci Res 5:1999–2003.

36. Kemna E, Pickkers P, Nemeth E, van der Hoeven H, Swinkels D (2005) Time-course analysis of hepcidin, serum iron, and plasma cytokine levels in humans injected with LPS. Blood 106:1864–1866.

37. Weinberg ED (1999) Iron loading and disease surveillance. Emerg Infect Dis 5:346–352.

38. Lundström U (2001) Iron deficiency anaemia Assesment, Prevention and Control. World Heal Organ 34:864–865.

39. Lynch SR (2011) Why Nutritional Iron Deficiency Persists as a Worldwide Problem. J Nutr 141:763S–768S.

40. (2015) WHO | Micronutrient deficiencies: Iron deficiency anaemia. In: WHO. http://www.who.int/nutrition/topics/ida/en/. Accessed 25 Jan 2018

41. Ramsay LC, Charles C V (2015) Review of Iron Supplementation and Fortification. Top Public Heal 175–195.

42. Kassebaum NJ, Jasrasaria R, Naghavi M, Wulf SK, Johns N, Lozano R, Regan M, Weatherall D, Chou DP, Eisele TP, Flaxman SR, Pullan RL, Brooker SJ, Murray CJL (2014) A systematic analysis of global anemia burden from 1990 to 2010. Blood 123:615–624.

43. Gulmez H, Akin Y, Savas M, Gulum M, Ciftci H, Yalcinkaya S, Yeni E (2014) Impact of iron supplementation on sexual dysfunction of women with iron deficiency anemia in short

term: a preliminary study. J Sex Med 11:1042–1046.

44. McClung JP, Murray-Kolb LE (2013) Iron nutrition and premenopausal women: effects of poor iron status on physical and neuropsychological performance. Annu Rev Nutr 33:271–288.

45. Stoltzfus RJ (2003) Iron deficiency: global prevalence and consequences. Food Nutr Bull 24:S99-103.

46. Haas JD, Brownlie T 4th (2001) Iron deficiency and reduced work capacity: a critical review of the research to determine a causal relationship. J Nutr 131:676S–688S; discussion 688S–690S.

47. Congdon EL, Westerlund A, Algarin CR, Peirano PD, Gregas M, Lozoff B, Nelson CA (2012) Iron deficiency in infancy is associated with altered neural correlates of recognition memory at 10 years. J Pediatr 160:1027–1033.

48. Pasricha S-R, Drakesmith H, Black J, Hipgrave D, Biggs B-A (2013) Control of iron deficiency anemia in low- and middle-income countries. Blood 121:2607–2617.

49. Auerbach M, Adamson JW (2016) How we diagnose and treat iron deficiency anemia. Am J Hematol 91:31–38.

50. Stockman R (1893) The Treatment of Chlorosis by Iron and some Other Drugs. Br Med J 1:881–885.

51. Finch C. (1994) Regulators of iron balance in humans. Blood 84:1697–1706.

52. Brugnara C, Beris P (2009) Iron therapy. ESH Handb Disord Erythropoiesis, Erythrocytes Iron Metab 21:512–529.

53. Tom W (2008) Comparison of Oral Iron Supplements. Pharm Lett 24:1–4.

54. Kruske SG, Ruben AR, Brewster DR (1999) An iron treatment trial in an aboriginal community: improving non-adherence. J Paediatr Child Health 35:153–158.

55. Pereira DIA, Bruggraber SFA, Faria N, Poots LK, Tagmount MA, Aslam MF, Frazer DM, Vulpe CD, Anderson GJ, Powell JJ (2014) Nanoparticulate iron(III) oxo-hydroxide delivers safe iron that is well absorbed and utilised in humans. Nanomedicine Nanotechnology, Biol Med 10:1877–1886.

56. Moretti D, Goede JS, Zeder C, Jiskra M, Chatzinakou V, Tjalsma H, Melse-boonstra A,

Brittenham G, Swinkels DW, Zimmermann MB (2015) Oral iron supplements increase hepcidin and decrease iron absorption from daily or twice daily doses in iron depleted young women. Blood 126:1981–1990.

57. Hedenus M, Birgegard G, Nasman P, Ahlberg L, Karlsson T, Lauri B, Lundin J, Larfars G, Osterborg A (2007) Addition of intravenous iron to epoetin beta increases hemoglobin response and decreases epoetin dose requirement in anemic patients with lymphoproliferative malignancies: a randomized multicenter study. Leukemia 21:627–632.

58. Auerbach M, Ballard H, Glaspy J (2007) Clinical update: intravenous iron for anaemia. Lancet 369:1502–1504.

59. Auerbach M, Ballard H (2010) Clinical use of intravenous iron: administration, efficacy, and safety. Hematol Am Soc Hematol Educ Progr 2010:338–347.

60. Goodnough LT, Skikne B, Brugnara C (2000) Erythropoietin, iron, and erythropoiesis. Blood 96:823–833.

61. Cançado RD, Muñoz M (2011) Intravenous iron therapy. Rev Bras Hematol Hemoter 33:461–469.

62. Weiss G, Goodnough LT (2005) Anemia of chronic disease. N Engl J Med 352:1011–1023.

63. Shovlin CL, Guttmacher AE, Buscarini E, Faughnan ME, Hyland RH, Westermann CJ, Kjeldsen AD, Plauchu H (2000) Diagnostic criteria for hereditary hemorrhagic telangiectasia (Rendu-Osler-Weber syndrome). Am J Med Genet 91:66–67.

64. Beris P, Muñoz M, García-Erce JA, Thomas D, Maniatis A, Van Der Linden P (2008) Perioperative anaemia management: Consensus statement on the role of intravenous iron. Br J Anaesth 100:599–604.

65. Munoz M, Breymann C, Garcia-Erce JA, Gomez-Ramirez S, Comin J, Bisbe E (2008) Efficacy and safety of intravenous iron therapy as an alternative/adjunct to allogeneic blood transfusion. Vox Sang 94:172–183.

66. Weiss G (2002) Iron and immunity: a double-edged sword. Eur J Clin Invest 32 Suppl 1:70–78.

67. Aronoff GR (2004) Safety of intravenous iron in clinical practice: implications for anemia management protocols. J Am Soc Nephrol 15 Suppl 2:S99-106.

68. Nagpal J, Choudhury P (2004) Iron formulations in pediatric practice. Indian Pediatr 41:807–815.

69. Santiago P (2012) Ferrous versus Ferric Oral Iron Formulations for the Treatment of Iron Deficiency: A Clinical Overview. Sci World J 2012:1–5.

70. Tolkien Z, Stecher L, Mander AP, Pereira DIA, Powell JJ (2015) Ferrous sulfate supplementation causes significant gastrointestinal side-effects in adults: A systematic review and meta-analysis. PLoS One 10:1–20.

71. Powell JJ, Bruggraber SFA, Faria N, Poots LK, Hondow N, Pennycook TJ, Latunde-Dada GO, Simpson RJ, Brown AP, Pereira DIA (2014) A nano-disperse ferritin-core mimetic that efficiently corrects anemia without luminal iron redox activity. Nanomedicine Nanotechnology, Biol Med 10:1529–1538.

72. Seril DN, Liao J, Ho K-LK, Warsi A, Yang CS, Yang G-Y (2002) Dietary iron supplementation enhances DSS-induced colitis and associated colorectal carcinoma development in mice. Dig Dis Sci 47:1266–1278.

73. Radulescu S, Brookes MJ, Salgueiro P, Ridgway RA, McGhee E, Anderson K, Ford SJ, Stones DH, Iqbal TH, Tselepis C, Sansom OJ (2012) Luminal iron levels govern intestinal tumorigenesis after Apc loss in vivo. Cell Rep 2:270–282.

74. Senior JH (2008) Nanoparticulate Drug Delivery Systems. Drug Dev Ind Pharm 34:116.

75. Anselmo AC, Mitragotri S (2016) Nanoparticles in the clinic. Bioeng Transl Med 1:10–29.

76. Torchilin VP (2014) Multifunctional, stimuli-sensitive nanoparticulate systems for drug delivery. Nat Rev Drug Discov 13:813–827.

77. Mozafari MR, Johnson C, Hatziantoniou S, Demetzos C (2008) Nanoliposomes and their applications in food nanotechnology. J Liposome Res 18:309–327.

78. Shudo J, Pongpeerapat A, Wanawongthai C, Moribe K, Yamamoto K (2008) In vivo assessment of oral administration of probucol nanoparticles in rats. Biol Pharm Bull 31:321–325.

79. Gao H, Chen H, Chen W, Tao F, Zheng Y, Jiang Y, Ruan H (2008) Effect of nanometer pearl powder on calcium absorption and utilization in rats. Food Chem 109:493–498.

80. Zariwala MG, Elsaid N, Jackson TL, Corral López F, Farnaud S, Somavarapu S, Renshaw D (2013) A novel approach to oral iron delivery using ferrous sulphate loaded solid lipid

nanoparticles. Int J Pharm 456:400–407.

81. Shafie EH, Keshavarz SA, Kefayati ME, Taheri F, Sarbakhsh P, Vafa MR (2016) The effects of nanoparticles containing iron on blood and inflammatory markers in comparison to ferrous sulfate in anemic rats. Int J Prev Med 2016:3–7.

82. Wegmuller R, Zimmermann MB, Moretti D, Arnold M, Langhans W, Hurrell RF (2004) Particle size reduction and encapsulation affect the bioavailability of ferric pyrophosphate in rats. J Nutr 134:3301–3304.

83. Silverstein SB, Rodgers GM (2004) Parenteral Iron Therapy Options. Am J Hematol 76:74–78.

84. Jahn MR, Andreasen HB, Fütterer S, Nawroth T, Schünemann V, Kolb U, Hofmeister W, Muñoz M, Bock K, Meldal M, Langguth P (2011) A comparative study of the physicochemical properties of iron isomaltoside 1000 (Monofer), a new intravenous iron preparation and its clinical implications. Eur J Pharm Biopharm 78:480–91.

85. Kalra PA, Bhandari S (2016) Efficacy and safety of iron isomaltoside (Monofer) in the management of patients with iron deficiency anemia. Int J Nephrol Renovasc Dis 9:53–64.

86. Macdougall LC (2009) Evolution of IV iron compounds over the last century. J Ren Care 35:8–13.

87. Gupta AK, Gupta M (2005) Synthesis and surface engineering of iron oxide nanoparticles for biomedical applications. Biomaterials 26:3995–4021.

88. Fütterer S, Andrusenko I, Kolb U, Hofmeister W, Langguth P (2013) Structural characterization of iron oxide/hydroxide nanoparticles in nine different parenteral drugs for the treatment of iron deficiency anaemia by electron diffraction (ED) and X-ray powder diffraction (XRPD). J Pharm Biomed Anal 86:151–160.

89. Geisser P, Burckhardt S (2011) The pharmacokinetics and pharmacodynamics of iron preparations. Pharmaceutics 3:12–33.

90. Zanganeh S, Hutter G, Spitler R, Lenkov O, Mahmoudi M, Shaw A, Pajarinen JS, Nejadnik H, Goodman S, Moseley M, Coussens LM, Daldrup-link HE (2016) Iron oxide nanoparticles inhibit tumour growth by inducing pro- inflammatory macrophage polarization in tumour tissues. Nat Nanotechnol 11:986–994.

91. Lin C-H, Chen C-H, Lin Z-C, Fang J-Y (2017) Recent advances in oral delivery of drugs and bioactive natural products using solid lipid nanoparticles as the carriers. J Food Drug Anal 25:219–234.

92. Zimmermann MB (2004) The potential of encapsulated iron compounds in food fortification: a review. Int J Vitam Nutr Res 74:453–461.

93. Durán E, Villalobos C, Churio O, Pizarro F, Valenzuela C (2017) Encapsulación de hierro: Otra estrategia para la prevención o tratamiento de la anemia por deficiencia de hierro. Rev Chil Nutr.

94. Chasteen ND, Harrison PM (1999) Mineralization in Ferritin: An Efficient Means of Iron Storage. J Struct Biol 126:182–194.

95. Hoppler M, Schonbachler A, Meile L, Hurrell RF, Walczyk T (2008) Ferritin-iron is released during boiling and in vitro gastric digestion. J Nutr 138:878–884.

96. Kidane TZ, Sauble E, Linder MC (2006) Release of iron from ferritin requires lysosomal activity. Am J Physiol Cell Physiol 291:C445-55.

97. Powell J, Bruggraber S, Faria N PD (2015) Ligand modified poly oxo-hydroxy metal ion materials, their uses and processes for their preparation. 1:1–52.

98. Onoue S, Yamada S, Chan HK (2014) Nanodrugs: Pharmacokinetics and safety. Int J Nanomedicine 9:1025–1037

99. Choi YH, Han H-K (2017) Nanomedicines: current status and future perspectives in aspect of drug delivery and pharmacokinetics. J Pharm Investig 0:1–18.

100. Andrade F, Rafael D, Videira M, Ferreira D, Sosnik A, Sarmento B (2013) Nanotechnology and pulmonary delivery to overcome resistance in infectious diseases. Adv Drug Deliv Rev 65:1816–1827.

101. Zazo H, Colino CI, Lanao JM (2016) Current applications of nanoparticles in infectious diseases. J Control Release 224:86–102.

102. Hirn S, Semmler-Behnke M, Schleh C, Wenk A, Lipka J, Schaffler M, Takenaka S, Moller W, Schmid G, Simon U, Kreyling WG (2011) Particle size-dependent and surface charge-dependent biodistribution of gold nanoparticles after intravenous administration. Eur J Pharm Biopharm 77:407–416.

103. Zhao G, Huang Y, Li G, Li S, Zhou Y, Lei Y, Chen X, Yang K, Chen Y, Yang K (2013) Subcellular

distribution and genotoxicity of silica nanoparticles in human bronchial epithelial cells. Chinese J lung cancer 16:117–124.

104. Abdulkarim M, Agullo N, Cattoz B, Griffiths P, Bernkop-Schnurch A, Borros SG, Gumbleton M (2015) Nanoparticle diffusion within intestinal mucus: Three-dimensional response analysis dissecting the impact of particle surface charge, size and heterogeneity across polyelectrolyte, pegylated and viral particles. Eur J Pharm Biopharm 97:230–238.

105. Lorenz S, Hauser CP, Autenrieth B, Weiss CK, Landfester K, Mailander V (2010) The softer and more hydrophobic the better: influence of the side chain of polymethacrylate nanoparticles for cellular uptake. Macromol Biosci 10:1034–1042.

106. Bawa P, Pillay V, Choonara Y, du Toit L (2009) Synthesis, characterization and targeting potential of zidovudine loaded sialic acid conjugated-mannosylated poly(propyleneimine) dendrimers. Biomed Mater 4:668–679.

107. Park JS, Han TH, Lee KY, Han SS, Hwang JJ, Moon DH, Kim SY, Cho YW (2006) N-acetyl histidine-conjugated glycol chitosan self-assembled nanoparticles for intracytoplasmic delivery of drugs: Endocytosis, exocytosis and drug release. J Control Release 115:37–45.

108. Bawa P, Pillay V, Choonara YE, du Toit LC (2009) Stimuli-responsive polymers and their applications in drug delivery. Biomed Mater 4:22001.

109. Hua X, Tan S, Bandara HMHN, Fu Y, Liu S, Smyth HDC (2014) Externally Controlled Triggered-Release of Drug from PLGA Micro and Nanoparticles. PLoS One 9:e114271.

110. Goodman CM, McCusker CD, Yilmaz T, Rotello VM (2004) Toxicity of gold nanoparticles functionalized with cationic and anionic side chains. Bioconjug Chem 15:897–900.

111. Oh N, Park J-H (2014) Surface Chemistry of Gold Nanoparticles Mediates Their Exocytosis in Macrophages. ACS Nano 8:6232–6241.

112. Bertrand N, Leroux J-C (2012) The journey of a drug-carrier in the body: an anatomo-physiological perspective. J Control Release 161:152–163.

113. Su Y, Wang L, Liang K, Liu M, Liu X, Song Y, Deng Y (2018) The accelerated blood clearance phenomenon of PEGylated nanoemulsion upon cross administration with nanoemulsions modified with polyglycerin. Asian J Pharm Sci 13:44–53.

114. Xia T, Kovochich M, Brant J, Hotze M, Sempf J, Oberley T, Sioutas C, Yeh JI, Wiesner MR, Nel AE (2006) Comparison of the abilities of ambient and manufactured nanoparticles to

induce cellular toxicity according to an oxidative stress paradigm. Nano Lett 6:1794–1807.

115. Prasad M, Lambe UP, Brar B, Shah I, J M, Ranjan K, Rao R, Kumar S, Mahant S, Khurana SK, Iqbal HMN, Dhama K, Misri J, Prasad G (2018) Nanotherapeutics: An insight into healthcare and multi-dimensional applications in medical sector of the modern world. Biomed Pharmacother 97:1521–1537.

116. Wang Y, Qin N, Chen S, Zhao J, Yang X (2013) Oxidative-damage effect of Fe3O4 nanoparticles on mouse hepatic and brain cells in vivo. Front Biol (Beijing) 8:549–555.

117. Shang L, Nienhaus K, Nienhaus G (2014) Engineered nanoparticles interacting with cells: size matters. J Nanobiotechnology 12:5-16.

118. Champion JA, Mitragotri S (2006) Role of target geometry in phagocytosis. Proc Natl Acad Sci U S A 103:4930–4.

119. Harper B, Thomas D, Chikkagoudar S, Baker N, Tang K, Heredia-Langner A, Lins R, Harper S (2015) Comparative hazard analysis and toxicological modeling of diverse nanomaterials using the embryonic zebrafish (EZ) metric of toxicity. J Nanoparticle Res.

120. Kirchner C, Liedl T, Kudera S, Pellegrino T, Munoz Javier A, Gaub HE, Stolzle S, Fertig N, Parak WJ (2005) Cytotoxicity of colloidal CdSe and CdSe/ZnS nanoparticles. Nano Lett 5:331–338.

121. Sharifi S, Behzadi S, Laurent S, Forrest ML, Stroeve P, Mahmoudi M (2012) Toxicity of nanomaterials. Chem Soc Rev 41:2323–2343.

122. Pereira DIA, Lederer B, Powell JJ (2015) A balanced salt solution that prevents agglomeration of nano iron oxo - hydroxides in serum - free cellular assays. Mater Res Express 2:15403.

123. Seabra AB, Pasquo T, Ferrarini ACF, Santos C, Haddad PS, Lima R De (2014) Preparation , Characterization , Cytotoxicity , and Genotoxicity Evaluations of Thiolated-and S - Nitrosated Superparamagnetic Iron Oxide Nanoparticles : Implications for Cancer Treatment. Chem. Res. Toxicol. 27:1207-1218.

124. Li L, Mak KY, Shi J, Koon HK, Leung CH, Wong CM, Leung CW, Mak CSK, Chan NMM, Zhong W, Lin KW, Wu EX, Pong PWT (2012) Comparative <I>In Vitro</I> Cytotoxicity Study on Uncoated Magnetic Nanoparticles: Effects on Cell Viability, Cell Morphology, and Cellular Uptake. J Nanosci Nanotechnol 12:9010–9017.

125. Magdolenova Z, Drlickova M, Henjum K, Rundén-Pran E, Tulinska J, Bilanicova D, Pojana G, Kazimirova A, Barancokova M, Kuricova M, Liskova A, Staruchova M, Ciampor F, Vavra I, Lorenzo Y, Collins A, Rinna A, Fjellsbø L, Volkovova K, Marcomini A, Amiry-Moghaddam M, Dusinska M (2015) Coating-dependent induction of cytotoxicity and genotoxicity of iron oxide nanoparticles. Nanotoxicology 9:44–56.

126. Ayala V, Herrera AP, Latorre-Esteves M, Torres-Lugo M, Rinaldi C (2013) Effect of surface charge on the colloidal stability and in vitro uptake of carboxymethyl dextran-coated iron oxide nanoparticles. J Nanoparticle Res. 15:1874.

127. Yen H-J, Hsu S-H, Tsai C-L (2009) Cytotoxicity and immunological response of gold and silver nanoparticles of different sizes. Small 5:1553–1561.

128. Soenen SJ, Rivera-Gil P, Montenegro J-M, Parak WJ, De Smedt SC, Braeckmans K (2011) Cellular toxicity of inorganic nanoparticles: Common aspects and guidelines for improved nanotoxicity evaluation. Nano Today 6:446–465.

129. Valdiglesias V, Kiliç G, Costa C, Fernández-Bertólez N, Pásaro E, Teixeira J, Laffon B (2015) Effects of Iron Oxide Nanoparticles: Cytotoxicity, Genotoxicity, Developmental Toxicity, and Neurotoxicity. Environ Mol Mutagen. 56:125-148

130. Wu H, Yin JJ, Wamer WG, Zeng M, Lo YM (2014) Reactive oxygen species-related activities of nano-iron metal and nano-iron oxides. J Food Drug Anal 22:86–94.

131. Valko M, Morris H, Cronin M (2005) Metals, Toxicity and Oxidative Stress. Curr Med Chem 12:1161–1208.

132. Thomas R (2001) A Beginner's Guide to ICP-MS. Spectroscopy:

133. Nelms S (2005) Inductively Coupled Plasma Mass Spectrometry Handbook. Blackwell

134. Jarvis KE, Gray AL, Houk RS (2003) Handbook of Inductively Coupled Plasma Mass Spectrometry. Viridian Publishing

135. Wilbur S, Yamanaka M, Sannac S (2017) Characterization of nanoparticles in aqueous samples by ICP-MS. Agil Technol 10.

136. Thomas R (2002) A Beginner's Guide to ICP-MS: Part XII — A Review of Interferences. Spectroscopy 17:24–31.

137. Thomas R (2013) Practical Guide to ICP-MS: A Tutorial for Beginners, Third Edition. Taylor & Francis

138. Jakubowski N, Moens L, Vanhaecke F (1998) Sector field mass spectrometers in ICP-MS. Spectrochim. Acta - Part B At. Spectrosc. 53:1739-1763.

139. Rodríguez-Castrillón JÁ, Moldovan M, García Alonso JI, Lucena JJ, García-Tomé ML, Hernández-Apaolaza L (2008) Isotope pattern deconvolution as a tool to study iron metabolism in plants. Anal Bioanal Chem 390:579–590.

140. Arizaga Rodríguez S, Blanco González E, Alvarez Llamas G, Montes-Bayón M, Sanz-Medel A (2005) Detection of transferrin isoforms in human serum: Comparison of UV and ICP-MS detection after CZE and HPLC separations. Anal Bioanal Chem 383:390–397.

141. Vanhaecke F, Balcaen L, De Wannemacker G, Moens L (2002) Capabilities of inductively coupled plasma mass spectrometry for the measurement of Fe isotope ratios. J Anal At Spectrom 17:933–943.

142. Boulyga SF, Becker JS (2001) ICP-MS with hexapole collision cell for isotope ratio measurements of Ca, Fe, and Se. Fresenius J Anal Chem 370:618–623.

143. Vogl J, Klingbeil P, Pritzkow W, Riebe G (2003) High accuracy measurements of Fe isotopes using hexapole collision cell MC-ICP-MS and isotope dilution for certification of reference materials. J Anal At Spectrom 18:1125–1132.

144. Degueldre C, Favarger PY, Wold S (2006) Gold colloid analysis by inductively coupled plasma-mass spectrometry in a single particle mode. Anal Chim Acta 555:263–268.

145. Witzler M, Küllmer F, Günther K (2018) Validating a Single-Particle ICP-MS Method to Measure Nanoparticles in Human Whole Blood for Nanotoxicology. Anal Lett 51:587–599.

146. Lee S, Bi X, Reed RB, Ranville JF, Herckes P, Westerhoff P (2014) Nanoparticle size detection limits by single particle ICP-MS for 40 elements. Environ Sci Technol 48:10291–10300.

147. Pozebon D, Scheffler GL, Dressler VL (2017) Recent applications of laser ablation inductively coupled plasma mass spectrometry (LA-ICP-MS) for biological sample analysis: a follow-up review. J Anal At Spectrom 32:890–919.

148. Becker JS, Matusch A, Wu B (2014) Bioimaging mass spectrometry of trace elements – recent advance and applications of LA-ICP-MS: A review. Anal Chim Acta 835:1–18.

149. Günther D, Hattendorf B (2005) Solid sample analysis using laser ablation inductively

coupled plasma mass spectrometry. TrAC Trends Anal Chem 24:255–265.

150. Ivask A, Mitchell AJ, Malysheva A, Voelcker NH, Lombi E (2017) Methodologies and approaches for the analysis of cell-nanoparticle interactions. Wiley Interdiscip Rev Nanomedicine Nanobiotechnology e1486:1-22.

151. Drescher D, Giesen C, Traub H, Panne U, Kneipp J, Jakubowski N (2012) Quantitative imaging of gold and silver nanoparticles in single eukaryotic cells by laser ablation ICP-MS. Anal Chem 84:9684–8.

152. Böhme S, Stärk H-J, Kühnel D, Reemtsma T (2015) Exploring LA-ICP-MS as a quantitative imaging technique to study nanoparticle uptake in Daphnia magna and zebrafish (Danio rerio) embryos. Anal Bioanal Chem 407:5477–5485.

153. Managh AJ, Hutchinson RW, Riquelme P, Broichhausen C, Wege AK, Ritter U, Ahrens N, Koehl GE, Walter L, Florian C, Schlitt HJ, Reid HJ, Geissler EK, Sharp BL, Hutchinson JA (2014) Laser ablation-inductively coupled plasma mass spectrometry: an emerging technology for detecting rare cells in tissue sections. J Immunol 193:2600–2608.

154. Mingos DMP (2014) Gold Clusters, Colloids and Nanoparticles I. Springer International Publishing

155. Williams DB, Carter CB (2009) Transmission Electron Microscopy: A Textbook for Materials Science. Springer

156. Wang ZL (2000) Characterization of nanophase materials. Wiley-VCH

157. Calzolai L, Gilliland D, Rossi F (2012) Measuring nanoparticles size distribution in food and consumer products: a review. Food Addit Contam Part A Chem Anal Control Expo Risk Assess 29:1183–1193.

158. Australian Microscopy & Microanalysis Research Facility Introduction - aims and learning outcomes | MyScope. http://www.ammrf.org.au/myscope/tem/introduction/. Accessed 8 Feb 2018

159. Spence JCH, Kolar HR, Hembree G, Humphreys CJ, Barnard J, Datta R, Koch C, Ross FM, Justo JF (2006) Imaging dislocation cores – the way forward. Philos Mag 86:4781–4796.

160. Fernández-Iglesias N, Bettmer J (2015) Complementary mass spectrometric techniques for the quantification of the protein corona: a case study on gold nanoparticles and human serum proteins. Nanoscale 7:14324–31.

161. Piqueras JR, Megías LM (1998) Manual de Técnicas de Microscopía Electrónica (M.E.T.): Aplicaciones Biológicas: Fundamentos y Procedimientos. Universidad de Granada

162. Swapp S Scanning Electron Microscopy (SEM). https://serc.carleton.edu/research_education/geochemsheets/techniques/SEM.html. Accessed 8 Feb 2018

163. Australian Microscopy & Microanalysis Research Facility Background information - What is scanning electron microscopy? | MyScope. http://www.ammrf.org.au/myscope/sem/background/. Accessed 8 Feb 2018

164. Eaton P, Quaresma P, Soares C, Neves C, Almeida MP De, Pereira E, West P (2017) A direct comparison of experimental methods to measure dimensions of synthetic nanoparticles. Ultramicroscopy 182:179–190.

165. Ledin A, Karlsson S, Düker A, Allard B (1994) Measurements in situ of concentration and size distribution of colloidal matter in deep groundwaters by photon correlation spectroscopy. Water Res 28:1539–1545.

166. Stetefeld J, McKenna SA, Patel TR (2016) Dynamic light scattering: a practical guide and applications in biomedical sciences. Biophys Rev 8:409–427.

167. Yu L, Andriola A (2010) Quantitative gold nanoparticle analysis methods: A review. Talanta 82:869–875.

168. Panacek A, Kvitek L, Prucek R, Kolar M, Vecerova R, Pizurova N, Sharma VK, Nevecna T, Zboril R (2006) Silver colloid nanoparticles: synthesis, characterization, and their antibacterial activity. J Phys Chem B 110:16248–16253.

169. Lapresta-Fernandez A, Doussineau T, Moro AJ, Dutz S, Steiniger F, Mohr GJ (2011) Magnetic core-shell fluorescent pH ratiometric nanosensor using a Stober coating method. Anal Chim Acta 707:164–170.

170. Schwamberger A, De Roo B, Jacob D, Dillemans L, Bruegemann L, Seo JW, Locquet JP (2015) Combining SAXS and DLS for simultaneous measurements and time-resolved monitoring of nanoparticle synthesis. Nucl Instruments Methods Phys Res Sect B Beam Interact with Mater Atoms 343:116–122.

171. Cho TJ, Hackley VA (2010) Fractionation and characterization of gold nanoparticles in aqueous solution: asymmetric-flow field flow fractionation with MALS, DLS, and UV-Vis detection. Anal Bioanal Chem 398:2003–2018.

172. Proulx K, Wilkinson KJ (2014) Separation, detection and characterisation of engineered nanoparticles in natural waters using hydrodynamic chromatography and multi-method detection (light scattering, analytical ultracentrifugation and single particle ICP-MS). Environ Chem 11:392–401.

173. Adelantado C, Rodríguez-Fariñas N, Rodríguez Martín-Doimeadios RC, Zougagh M, Ríos Á (2016) Analysis of silica nanoparticles by capillary electrophoresis coupled to an evaporative light scattering detector. Anal Chim Acta 923:82–88.

174. Dhawan A, Sharma V (2010) Toxicity assessment of nanomaterials: methods and challenges. Anal Bioanal Chem 398:589–605.

175. Lespes G, Gigault J (2011) Hyphenated analytical techniques for multidimensional characterisation of submicron particles: A review. Anal Chim Acta 692:26–41.

176. Gigault J, Le Hécho I, Dubascoux S, Potin-Gautier M, Lespes G (2010) Single walled carbon nanotube length determination by asymmetrical-flow field-flow fractionation hyphenated to multi-angle laser-light scattering. J Chromatogr A 1217:7891–7897.

177. Brewer AK, Striegel AM (2011) Characterizing the size, shape, and compactness of a polydisperse prolate ellipsoidal particle via quadruple-detector hydrodynamic chromatography. Analyst 136:515–519.

178. Kammer F v. d., Baborowski M, Friese K (2005) Field-flow fractionation coupled to multi-angle laser light scattering detectors: Applicability and analytical benefits for the analysis of environmental colloids. Anal Chim Acta 552:166–174.

179. Giannini C, Ladisa M, Altamura D, Siliqi D, Sibillano T, De Caro L (2016) X-ray Diffraction: A Powerful Technique for the Multiple-Length-Scale Structural Analysis of Nanomaterials. Crystals 6:87.

180. Cantor CR, Schimmel PR (1980) Biophysical Chemistry: Part II: Techniques for the Study of Biological Structure and Function. W. H. Freeman

181. Lapresta-Fernandez A, Doussineau T, Dutz S, Steiniger F, Moro AJ, Mohr GJ (2011) Magnetic and fluorescent core-shell nanoparticles for ratiometric pH sensing. Nanotechnology 22:415501.

182. Thomas S, Nair SK, Jamal EMA, Al-Harthi SH, Varma MR, Anantharaman MR (2008) Size-dependent surface plasmon resonance in silver silica nanocomposites. Nanotechnology 19:75710.

183. Lipfert J, Doniach S (2007) Small-angle X-ray scattering from RNA, proteins, and protein complexes. Annu Rev Biophys Biomol Struct 36:307–327.

184. Rao CNR, Biswas K (2009) Characterization of nanomaterials by physical methods. Annu Rev Anal Chem (Palo Alto Calif) 2:435–462.

185. Smetana AB, Klabunde KJ, Marchin GR, Sorensen CM (2008) Biocidal Activity of Nanocrystalline Silver Powders and Particles. Langmuir 24:7457–7464.

186. Roy P, Berger S, Schmuki P (2011) TiO2 Nanotubes: Synthesis and Applications. Angew Chemie Int Ed 50:2904–2939.

187. Wang DZ, Wille U, Juaristi E (2017) Encyclopedia of Physical Organic Chemistry: Wiley

188. Goldstein J (2003) Scanning Electron Microscopy and X-ray Microanalysis: Third Edition. Springer US

189. Patel KN, Patel JK, Patel MP, Rajput GC, Patel HA (2010) Introduction to hyphenated techniques and their applications in pharmacy. Pharm Methods 1:2–13.

190. Wilson ID, Brinkman UAT (2003) Hyphenation and hypernation the practice and prospects of multiple hyphenation. J Chromatogr A 1000:325–356.

191. Siebrands T, Giersig M, Mulvaney P, Fischer CH (1993) Steric exclusion chromatography of nanometer-sized gold particles. Langmuir 9:2297–2300.

192. Helfrich A, Brüchert W, Bettmer J (2006) Size characterisation of Au nanoparticles by ICP-MS coupling techniques. J Anal At Spectrom 21:431–434.

193. Helfrich A, Bettmer J (2011) Analysis of gold nanoparticles using ICP-MS-based hyphenated and complementary ESI-MS techniques. Int J Mass Spectrom 307:92–98.

194. Wei G-T, Liu F-K, Wang CRC (1999) Shape Separation of Nanometer Gold Particles by Size-Exclusion Chromatography. Anal Chem 71:2085–2091.

195. Liu F-K (2007) SEC Characterization of Au Nanoparticles Prepared through Seed-Assisted Synthesis. Chromatographia 66:791–796.

196. Liu F-K (2008) Monitoring the Synthesis of Au Nanoparticles Using SEC. Chromatographia 68:81–87.

197. Wei G-T, Liu F-K (1999) Separation of nanometer gold particles by size exclusion chromatography. J Chromatogr A 836:253–260.

198. Liu F-K, Wei G-T (2004) Effect of Mobile-Phase Additives on Separation of Gold Nanoparticles by Size-Exclusion Chromatography. Chromatographia 59:115–119.

199. Jimenez-Lamana J, Laborda F, Bolea E, Abad-Alvaro I, Castillo JR, Bianga J, He M, Bierla K, Mounicou S, Ouerdane L, Gaillet S, Rouanet J-M, Szpunar J (2014) An insight into silver nanoparticles bioavailability in rats. Metallomics 6:2242–2249.

200. Striegel AM, Brewer AK (2012) Hydrodynamic Chromatography. Annu Rev Anal Chem 5:15–34.

201. Tiede K, Boxall ABA, Tiede D, Tear SP, David H, Lewis J (2009) A robust size-characterisation methodology for studying nanoparticle behaviour in "real" environmental samples, using hydrodynamic chromatography coupled to ICP-MS. J Anal At Spectrom 24:964–972.

202. Pergantis SA, Jones-Lepp TL, Heithmar EM (2012) Hydrodynamic Chromatography Online with Single Particle-Inductively Coupled Plasma Mass Spectrometry for Ultratrace Detection of Metal-Containing Nanoparticles. Anal Chem 84:6454–6462.

203. Rakcheev D, Philippe A, Schaumann GE (2013) Hydrodynamic chromatography coupled with single particle-inductively coupled plasma mass spectrometry for investigating nanoparticles agglomerates. Anal Chem 85:10643–10647.

204. Malejko J, Natalia Ś, Bajguz A, Ż BG- (2018) Method development for speciation analysis of nanoparticle and ionic forms of gold in biological samples by high performance liquid chromatography hyphenated to inductively coupled plasma mass spectrometry ☆. Spectrochim Acta Part B 142:1–7.

205. Hanley TA, Saadawi R, Zhang P, Caruso JA, Landero-Figueroa J (2014) Separation of silver ions and starch modified silver nanoparticles using high performance liquid chromatography with ultraviolet and inductively coupled mass spectrometric detection. Spectrochim Acta Part B At Spectrosc 100:173–179.

206. Zhou X-X, Liu R, Liu J-F (2014) Rapid Chromatographic Separation of Dissoluble Ag(I) and Silver-Containing Nanoparticles of 1–100 Nanometer in Antibacterial Products and Environmental Waters. Environ Sci Technol 48:14516–14524.

207. Surugau N, Urban PL (2009) Electrophoretic methods for separation of nanoparticles. J Sep Sci 32:1889–1906.

208. Hancu G, Simon B, Rusu A, Mircia E, Gyéresi Á (2013) Principles of Micellar Electrokinetic

Capillary Chromatography Applied in Pharmaceutical Analysis. Adv Pharm Bull 3:1–8.

209. Franze B, Engelhard C (2014) Fast Separation, Characterization, and Speciation of Gold and Silver Nanoparticles and Their Ionic Counterparts with Micellar Electrokinetic Chromatography Coupled to ICP-MS. Anal Chem 86:5713–5720.

210. Giddings JC (1966) A New Separation Concept Based on a Coupling of Concentration and Flow Nonuniformities. Sep Sci 1:123–125.

211. Meermann B (2015) Field-flow fractionation coupled to ICP–MS: separation at the nanoscale, previous and recent application trends. Anal Bioanal Chem 407:2665–2674.

212. Wagner M, Holzschuh S, Traeger A, Fahr A, Schubert US (2014) Asymmetric flow field-flow fractionation in the field of nanomedicine. Anal Chem 86:5201–5210.

213. Malik MI, Pasch H (2016) Field-flow fractionation: New and exciting perspectives in polymer analysis. Prog Polym Sci 63:42–85.

214. Caldwell KD, Cheng Z-Q, Hradecky P, Giddings JC (1984) Separation of human and animal cells by steric field-flow fractionation. Cell Biophys 6:233–251.

215. Thielking H, Roessner D, Kulicke W-M (1995) Online Coupling of Flow Field-Flow Fractionation and Multiangle Laser Light Scattering for the Characterization of Polystyrene Particles. Anal Chem 67:3229–3233.

216. Krystek P, Ulrich A, Garcia CC, Manohar S, Ritsema R (2011) Application of plasma spectrometry for the analysis of engineered nanoparticles in suspensions and products. J Anal At Spectrom 26:1701–1721.

217. Sötebier CA, Bierkandt FS, Rades S, Jakubowski N, Panne U, Weidner SM (2015) Sample loss in asymmetric flow field-flow fractionation coupled to inductively coupled plasma-mass spectrometry of silver nanoparticles. J Anal At Spectrom 30:2214–2222.

218. Hagendorfer H, Kaegi R, Traber J, Mertens SF, Scherrers R, Ludwig C, Ulrich A (2011) Application of an asymmetric flow field flow fractionation (AF4) multi-detector approach for metallic ENP characterization - prospects and limitations demonstrated on Au nanoparticles. Anal Chim Acta 706:367–378.

219. Alonso J, Gonzalez P (2013) Isotope Dilution Mass Spectrometry. The Royal Society of Chemistry

220. American Reagent I Venofer® (iron sucrose injection, USP) - Indications and Dosage.

http://www.venofer.com/Indications_Dosage. Accessed 15 Nov 2017

221. Danielson BG, Salmonson T, Derendorf H, Geisser P (1996) Pharmacokinetics of iron(III)-hydroxide sucrose complex after a single intravenous dose in healthy volunteers. Arzneimittelforschung 46:615–621.

222. De La Calle Guntiñas MB, Bordin G, Rodriguez AR (2004) Study of the feasibility of using a pellicular anion-exchange column for separation of transferrin isoforms in human serum by HPLC with UV detection. Anal Bioanal Chem 378:383–387.

223. Del Castillo Busto ME, Montes-Bayón M, Sanz-Medel A (2006) Accurate determination of human serum transferrin isoforms: Exploring metal-specific isotope dilution analysis as a quantitative proteomic tool. Anal Chem 78:8218–8226.

224. Nuevo Ordóñez Y, Montes-Bayón M, Blanco-González E, Paz-Jiménez J, Tejerina-Lobo JM, Peña-López JM, Sanz-Medel A (2009) Metal release in patients with total hip arthroplasty by DF-ICP-MS and their association to serum proteins. J Anal At Spectrom 24:1037–1043.

225. Jarrett BR, Frendo M, Vogan J, Louie AY (2007) Size-controlled synthesis of dextran sulfate coated iron oxide nanoparticles for magnetic resonance imaging. Nanotechnology 18:35603–35610.

226. Ahmadi R, Hosseini HRM, Masoudi A, Omid H, Namivandi-Zangeneh R, Ahmadi M, Ahmadi Z, Gu N (2013) Effect of concentration on hydrodynamic size of magnetite-based ferrofluid as a potential MRI contrast agent. Colloids Surfaces A Physicochem Eng Asp 424:113–117.

227. Saraswathy A, Nazeer SS, Nimi N, Arumugam S, Shenoy SJ, Jayasree RS (2014) Synthesis and characterization of dextran stabilized superparamagnetic iron oxide nanoparticles for in vivo MR imaging of liver fibrosis. Carbohydr Polym 101:760–8.

228. Easo SL, Mohanan P V (2013) Dextran stabilized iron oxide nanoparticles: synthesis, characterization and in vitro studies. Carbohydr Polym 92:726–32.

229. Gamboa JM, Leong KW (2013) In vitro and in vivo models for the study of oral delivery of nanoparticles. Adv Drug Deliv Rev 65:800–810.

230. Iglesias-González T, Sánchez-González C, Montes-Bayón M, Llopis-González J, Sanz-Medel A (2012) Absorption, transport and insulin-mimetic properties of bis(maltolato)oxovanadium (IV) in streptozotocin-induced hyperglycemic rats by integrated mass spectrometric techniques. Anal Bioanal Chem 402:277–285.

231. Nóbrega JA, Pirola C, Fialho LL, Rota G, De Campos Jordão CEKMA, Pollo F (2012) Microwave-assisted digestion of organic samples: How simple can it become? Talanta 98:272–276.

232. Faria N, Winship PD, Weiss DJ, Coles BJ, Schoenberg R, Hutchinson C, Pereira DIA, Powell JJ (2011) Development of DRC-ICP-MS methodology for the rapid determination of 58Fe erythrocyte incorporation in human iron absorption studies. J Anal At Spectrom 26:1648–1652.

233. Fiorito V, Crich SG, Silengo L, Altruda F, Aime S, Tolosano E (2012) Assessment of iron absorption in mice by ICP-MS measurements of 57Fe levels. Eur J Nutr 51:783–789.

234. del Castillo Busto ME, Montes-Bayón M, Bettmer J, Sanz-Medel A (2008) Stable isotope labelling and FPLC–ICP-SFMS for the accurate determination of clinical iron status parameters in human serum. Analyst 133:379–384.

235. Bautista MC, Bomati-Miguel O, Zhao X, Morales MP, González-Carreño T, Alejo RP de, Ruiz-Cabello J, Veintemillas-Verdaguer S (2004) Comparative study of ferrofluids based on dextran-coated iron oxide and metal nanoparticles for contrast agents in magnetic resonance imaging. Nanotechnology 15:S154–S159.

236. Kudasheva DS, Lai J, Ulman A, Cowman MK (2004) Structure of carbohydrate-bound polynuclear iron oxyhydroxide nanoparticles in parenteral formulations. J Inorg Biochem 98:1757–69.

237. RD H, MH B, AL S (1980) Intravenous iron dextran in clinical medicine. JAMA 243:1726–1731.

238. Muñiz CS, Fernández-Martin JL, Marchante-Gayón JM, García Alonso JI, Cannata-Andía JB, Sanz-Medel a (2001) Reference values for trace and ultratrace elements in human serum determined by double-focusing ICP-MS. Biol Trace Elem Res 82:259–272.

239. del Castillo Busto E, Montes-Bayón M, García Alonso JI, Caruso J a, Sanz-Medel a (2010) Novel HPLC-ICP-MS strategy for the determination of beta2-transferrin, the biomarker of cerebrospinal fluid (CSF) leakage. Analyst 135:1538–1540.

240. Nuevo-Ordonez Y, Montes-Bayon M, Blanco Gonzalez E, Sanz-Medel A, Nuevo-Ordoñez Y, Montes-Bayón M, Blanco González E, Sanz-Medel A (2011) Titanium preferential binding sites in human serum transferrin at physiological concentrations. Met Integr biometal Sci 3:1297–303.

241. Anraku M, Kitamura K, Shinohara A, Adachi M, Suenaga A, Maruyama T, Miyanaka K, Miyoshi T, Shiraishi N, Nonoguchi H, Otagiri M, Tomita K (2004) Intravenous iron administration induces oxidation of serum albumin in hemodialysis patients. Kidney Int 66:841–848.

242. Maity D, Agrawal DC (2007) Synthesis of iron oxide nanoparticles under oxidizing environment and their stabilization in aqueous and non-aqueous media. J Magn Magn Mater 308:46–55.

243. Laurent S, Forge D, Port M, Roch a, Robic C, Elst L V, Muller RN (2008) Magnetic Iron Oxide Nanoparticles: Synthesis, Stabilization, Vectorization, Physicochemical Characterizations, and Biological Applications (vol 108, pg 2064, 2008). Chem Rev 108:2064–2110.

244. Verhoeckx, K., Cotter, P., López-Expósito, I., Kleiveland, C., Lea, T., Mackie, A., Requena, T., Swiatecka, D., Wichers H (2015) The Impact of Food Bioactives on Health: In Vitro and Ex Vivo Models. Impact Food Bioact Heal Vitr Ex Vivo Model. Springer International Publishing AG Switzerland.

245. Polak-Charcon MHYB-SS (1990) A morphological study of a human adenocarcinoma cell line (HT29) differentiating in culture. Similarities to intestinal embryonic development. Cell Differ Dev 31:207–218.

246. Zweibaum A, Pinto M, Chevalier G, Dussaulx E, Triadou N, Lacroix B, Haffen K, Brun J-L, Rousset M (1985) Enterocytic differentiation of a subpopulation of the human colon tumor cell line HT-29 selected for growth in sugar-free medium and its inhibition by glucose. J Cell Physiol 122:21–29.

247. Pinto M, Appay M, Simon-Assmann P, Chevalier G, Dracopoli N, Fogh J, Zweibaum A (1983) Enterocyte-like differentiation and polarization of the human colon cancer cells by replacement of glucose by galactose in the medium. Biol Cell 44:193–196.

248. Stipanuk MH, Caudill MA (2013) Biochemical, Physiological, and Molecular Aspects of Human Nutrition. Elsevier Health Sciences

249. Sanderson IR, Walker WA (1993) Uptake and transport of macromolecules by the intestine: Possible role in clinical disorders (an update). Gastroenterology 104:622–639.

250. Alleyne M, McDonald H, Miller JL (2009) Individualized treatment for iron deficiency anemia in adults. Am J Med 121:943–948.

251. Rottmann L, Heumann KG (1994) Development of an Online Isotope-Dilution Technique with Hplc Icp-Ms for the Accurate Determination of Elemental Species. Fresenius J Anal Chem 350:221–227.

252. Gamboa JM, Leong KW (2013) In vitro and in vivo models for the study of oral delivery of nanoparticles. Adv Drug Deliv Rev 65:800–810.

253. Sinnecker H, Krause T, Koelling S, Lautenschläger I, Frey A (2014) The gut wall provides an effective barrier against nanoparticle uptake. Beilstein J Nanotechnol 5:2092–2101.

254. Morgan EH, Oates PS (2002) Mechanisms and regulation of intestinal iron absorption. Blood Cells Mol Dis 29:384–399.

255. Mackenzie B, Garrick MD (2005) Iron Imports. II. Iron uptake at the apical membrane in the intestine. Am J Physiol Gastrointest Liver Physiol 289:G981–G986.

256. Sánchez-González C, López-Chaves C, Trenzado CE, Aranda P, López-Jurado M, Gómez-Aracena J, Montes-Bayón M, Sanz-Medel A, Llopis J (2014) Changes in iron metabolism and oxidative status in STZ-induced diabetic rats treated with bis(maltolato) oxovanadium (IV) as an antidiabetic agent. Sci World J. 2014:1-6.

257. Sanchez-Morito N, Planells E, Aranda P, Llopis J (2000) Influence of magnesium deficiency on the bioavailability and tissue distribution of iron in the rat. J Nutr Biochem 11:103–108.

258. Gomez-Ayala AE, Campos MS, Lopez-Aliaga I, Pallares I, Hartiti S, Barrionuevo M, Alferez MJ, Rodriguez-Matas MC, Lisbona F (1997) Effect of source of iron on duodenal absorption of iron, calcium, phosphorous, magnesium, copper and zinc in rats with ferropoenic anaemia. Int J Vitam Nutr Res 67:106–114.

259. Udall JN, Pang K, Fritze L, Kleinman R, Walker WA (1981) Development of gastrointestinal mucosal barrier. I. The effect of age on intestinal permeability to macromolecules. Pediatr Res 15:241–244.

260. Gunshin H, Mackenzie B, Berger U V, Gunshin Y, Romero MF, Boron WF, Nussberger S, Gollan JL, Hediger MA (1997) Cloning and characterization of a mammalian proton-coupled metal-ion transporter. Nature 388:482–488.

261. Bobo D, Robinson KJ, Islam J, Thurecht KJ, Corrie SR (2016) Nanoparticle-Based Medicines: A Review of FDA-Approved Materials and Clinical Trials to Date. Pharm Res 33:2373–2387.

262. Lopez-Chaves C, Soto-Alvaredo J, Montes-Bayon M, Bettmer J, Llopis J, Sanchez-Gonzalez C (2018) Gold nanoparticles: Distribution, bioaccumulation and toxicity. In vitro and in vivo studies. Nanomedicine Nanotechnology, Biol Med 14:1–12.

# Selbständigkeitserklärung

Hiermit erkläre ich, die Dissertation selbständig und unter Verwendung der angegebenen Hilfen und Hilfsmittel angefertigt zu haben.

I declare that I have completed the thesis independently using only the aids and tools specified.

**Berlin, 17 May 2018** **Jenifer García Fernández**

# List of publications

## Publications

J. García-Fernández, J. Bettmer, N. Jakubowski, U. Panne, E. Añón, M. Montes-Bayón, A. Sanz-Medel, *The fate of iron nanoparticles used for treatment of iron deficiency in blood using mass-spectrometry based strategies*, Microchim. Acta. (2017) 1–8. doi:10.1007/s00604-017-2388-8.

J. García Fernandez, C. Sánchez, J. Bettmer, J. Llopis, N. Jakubowski, U. Panne, M. Montes-Bayón, *Quantitative assessment of the metabolic products of iron oxide nanoparticles to be used as iron supplements in cell cultures* (submitted).

## Conferences

European Winter Conference on Plasma Spectrochemistry, 2015 in Münster (Germany), ***Studies on the Bioavailability of Fe from Iron Oxide Nanoparticles Used for the Treatment of Iron Deficiency*** (Poster Presentation).

Winter Conference on Plasma Spectrochemistry, 2016 in Tucson (Arizona, U.S.A), ***Synthesis, Characterization and Toxicological Evaluation of Iron Oxide Nanoparticles Used for the Treatment of Iron Deficiency*** (Poster Presentation).

International Symposium on Metallomics, 2017 in Vienna (Austria), ***Studies on Characterization and Bioavailability of Iron Oxide Nanoparticles for the Treatment of Iron Deficiency Anaemia*** (Oral Presentation).

European Symposium on Atomic Spectrometry-Colloquium Analytische Atomspektroskopie-Anwendertreffen Plasmaspektrometrie ESAS & CANAS, 2018 in Berlin (Germany), ***Studies on the separation and quantification of nanoparticles and ionic species of iron in Caco-2 cells by HPLC-ICP-MS*** (Oral Presentation).

**Berlin, 8 April 2018** **Jenifer García Fernández**